

18 AFWL TR-77-6

LEVEL II

2
AFWL-TR
77-6

AD A O 6 0 7 3 2

DDC FILE COPY



6 DYNAMIC AIRBLAST SIMULATOR (DABS) INSTRUMENTATION DEVELOPMENT, PHASE I

Eric H. Wang Research Facility
University of New Mexico
Albuquerque, NM 87131

- 11 Aug 1978
- 12 198 p.
- 15 F29601-76-C-φφ15
- 9 Final Report,
- 10 Neal / Baum
- 14 CERT-FI-5

Approved for public release; distribution unlimited.

This research was sponsored by the Defense Nuclear Agency under Subtask L11CAXSX 352, Work Unit 56, DABS Instrumentation Development DNA Coordination.

Prepared for
Director
DEFENSE NUCLEAR AGENCY
Washington, DC 20305

16 WIDNS,
L11CAXS

17 φ3,
X352

62104A
AIR FORCE WEAPONS LABORATORY
Air Force Systems Command
Kirtland Air Force Base, NM 87117

DDC
RECEIVED
NOV 2 1978
REGULATED
D

78 10 31 065 400 976 mit

This final report was prepared by the Eric H. Wang Civil Engineering Research Facility, Albuquerque, New Mexico, under Contract F29601-76-C-0015, Job Order WDNS 0302 with the Air Force Weapons Laboratory, Kirtland Air Force Base, New Mexico. Joe Renick and Joe V. Quintana (DED) were the Laboratory Project Officers-in-Charge.

When US Government drawings, specifications, or other data are used for any purpose other than a definitely related Government procurement operation, the Government thereby incurs no responsibility nor any obligation whatsoever, and the fact that the Government may have formulated, furnished, or in any way supplied the said drawings, specifications, or other data is not to be regarded by implication or otherwise as in any manner licensing the holder or any other person or corporation or conveying any rights or permission to manufacture, use, or sell any patented invention that may in any way be related thereto.

This report has been authored by a contractor of the United States Government. Accordingly, the United States Government retains a nonexclusive, royalty-free license to publish or reproduce the material contained herein, or allow others to do so, for the United States Government purposes.

This report has been reviewed by the Office of Information (OI) and is releasable to the National Technical Information Service (NTIS). At NTIS, it will be available to the general public, including foreign nations.

This technical report has been reviewed and is approved for publication.



JOE RENICK
Project Officer

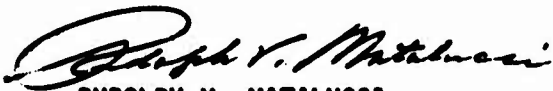


JOE V. QUINTANA
Project Officer

FOR THE COMMANDER



STEWART W. JOHNSON
Lt Colonel, USAF
Chief, Civil Engineering Research
Division



RUDOLPH V. MATALUCCI
Lt Colonel, USAF
Chief, Simulation Branch

DO NOT RETURN THIS COPY. RETAIN OR DESTROY.



UNCLASSIFIED

SECURITY CLASSIFICATION OF THIS PAGE (When Data Entered)

REPORT DOCUMENTATION PAGE		READ INSTRUCTIONS BEFORE COMPLETING FORM
1. REPORT NUMBER AFWL-TR-77-6✓	2. GOVT ACCESSION NO.	3. RECIPIENT'S CATALOG NUMBER
4. TITLE (and Subtitle) DYNAMIC AIRBLAST SIMULATOR (DABS) INSTRUMENTATION DEVELOPMENT - PHASE I	5. TYPE OF REPORT & PERIOD COVERED Final Report	
	6. PERFORMING ORG. REPORT NUMBER CERF FI-5✓	
7. AUTHOR(s) Neal Baum	8. CONTRACT OR GRANT NUMBER(s) F29601-76-C-0015✓	
9. PERFORMING ORGANIZATION NAME AND ADDRESS Eric H Wang Civil Engineering Research Facility University of New Mexico Albuquerque, NM 87131	10. PROGRAM ELEMENT, PROJECT, TASK AREA & WORK UNIT NUMBERS 62704H WDNS 0320	
11. CONTROLLING OFFICE NAME AND ADDRESS Director Defense Nuclear Agency Washington, DC 20305	12. REPORT DATE August 1978	
	13. NUMBER OF PAGES 206	
14. MONITORING AGENCY NAME & ADDRESS (if different from Controlling Office) Air Force Weapons Laboratory (DED) Kirtland Air Force Base, NM 87117	15. SECURITY CLASS. (of this report) UNCLASSIFIED	
	15a. DECLASSIFICATION/DOWNGRADING SCHEDULE	
16. DISTRIBUTION STATEMENT (of this Report) Approved for public release; distribution unlimited		
17. DISTRIBUTION STATEMENT (of the abstract entered in Block 20, if different from Report)		
18. SUPPLEMENTARY NOTES This research was sponsored by the Defense Nuclear Agency under Subtask L11CAXSX 352, Work Unit 56, DABS Instrumentation Development DNA Coordination was through DNA Subtask Manager Tom E. Kennedy via letter o/a 6 January 1978.		
19. KEY WORDS (Continue on reverse side if necessary and identify by block number) Instrumentation Acoustic Velocity Airblast Thermometry Debris Collection		
20. ABSTRACT (Continue on reverse side if necessary and identify by block number) In conjunction with the MX Program the Air Force Weapons Laboratory has been developing a Dynamic Airblast Simulator (DABS), the purpose of which is to simulate the airblast produced by a nuclear device. Since the detonation products of the explosives used to drive the DABS contribute a significant loading pulse, the environment is loaded with debris and ill-defined. Thus development of new instrumentation to parameterize this flow was undertaken. Microwave systems, an infrared detector, an optical photodiode, a debris collector, shock-on-shock instrumentation, and pressure and velocity gages were investigated.		

PREFACE

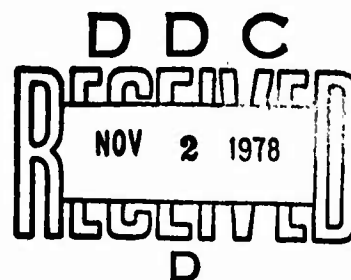
The author wishes to extend special acknowledgment to the authors of the materials included in the appendixes of this report: Appendix B, which was accomplished under subcontract by Mr. Carroll Griffin and Dr. Otto Friedrich of Applied Research Laboratories, University of Texas at Austin, Austin, Texas; Appendix C, a report prepared under subcontract by Dr. Bradford Sturtevant of Graduate Aeronautical Laboratories, California Institute of Technology, Pasadena, California; Appendix D, an investigative study conducted under subcontract by Artec Associates, Incorporated, Hayward, California, where Dr. Dennis Baum was project director for Artec; Appendix E, a report prepared by Dr. R. L. Taylor through subcontract to Physical Sciences, Incorporated, of Wakefield, Massachusetts; and Appendix F, a memorandum submitted by Dr. Robert A. Golobic of RAD, Incorporated, Colorado Springs, Colorado.

In addition to the authors of the above appendixes, the author would like to acknowledge the help and assistance of Mr. Joseph Renick of AFWL/DE, Dr. Bruce Hartenbaum of H-Tech, Dr. Reynold Shunk of Electromechanical Systems, Incorporated, Dr. Ron Hansen of Stanford, Lt. Col. Lannon Stafford, USAF, and Mr. Darwin Boor of CERF.

This technical document was prepared to report activity funded in part by the Defense Nuclear Agency, Subtask Code L11CAXS352, Work Unit Code 56.

L2710H

DISTRIBUTION TO		
DDP	White Section	<input checked="" type="checkbox"/>
DDO	Gen Section	<input type="checkbox"/>
UNCLASSIFIED		<input type="checkbox"/>
JUSTIFICATION		
BY		
DISTRIBUTION/AVAILABILITY CODES		
GEN.	AVAIL.	SPECIAL
A		



78 10 31 055

CONTENTS

<u>Section</u>		<u>Page</u>
1	INTRODUCTION	7
2	MICROWAVE SYSTEMS	11
	Doppler Radar	11
	Particle Velocimeter	20
3	INFRARED DETECTOR	27
4	OPTICAL PHOTODIODE	37
5	DEBRIS COLLECTOR	43
6	SHOCK-ON-SHOCK INSTRUMENTATION	53
7	PRESSURE AND VELOCITY GAGES	59
	Stagnation Pressure Gage	59
	Driver-Chamber Pressure Gages	59
	Magnetohydrodynamic Velocity Gage	64
8	CONCLUSIONS AND RECOMMENDATIONS	71
	APPENDIX A: DOPPLER RADAR SYSTEM FOR DYNAMIC AIRBLAST SIMULATOR	73
	APPENDIX B: RADAR TECHNIQUES FOR VELOCITY FIELD MEASUREMENTS BEHIND A TUNNEL CONFINED SHOCK WAVE	87
	APPENDIX C: IMPLEMENTATION OF A BLAST-WAVE VELOCITY GAUGE FOR THE DYNAMIC AIRBLAST SIMULATOR	127
	APPENDIX D: FEASIBILITY OF MAGNETIC VELOCITY GAGE FOR DABS TESTS	139
	APPENDIX E: RECOMMENDATIONS FOR INSTRUMENTATION FOR DYNAMIC AIR BLAST SIMULATOR	177
	APPENDIX F: CERF INSTRUMENTATION RECOMMENDATIONS	195
	ABBREVIATIONS, ACRONYMS, AND SYMBOLS	201

ILLUSTRATIONS

<u>Figure</u>		<u>Page</u>
1	Radar Buffer Amplifier	14
2	Doppler Radar Signal from 7-mm Magnum Bullet	15
3	Radar Unit	16
4	Raw Data from DABS IC	18
5	Radar Velocity Data from DABS IC	19
6	Raw Data from DABS ID	21
7	Raw Data from DABS IE	22
8	Radar Velocity Data from DABS ID	23
9	Radar Velocity Data from DABS IE	24
10	Microwave Particle Velocimeter System	25
11	Spectral Distribution of Black-Body Radiation at Various Temperatures	28
12	Infrared Detector Response	29
13	Infrared Detector Circuitry on DABS ID	29
14	Mount for Infrared Detector	30
15	Response from Infrared Detector	33
16	Comparison of Infrared and Radar Data	35
17	Infrared Detector Circuit for DABS IE	36
18	Spectral Response of Photodiode	38
19	Photodiode Circuit	38
20	Current Monitor Output	40
21	Photodiode Output from DABS ID	41
22	Second Peak in DABS ID	45
23	Debris Collector	48
24	Time of Closure of Mechanism for Debris Collector	49
25	Stagnation Pulse from DABS IE	51
26	Supersonic Pitot Tube	54
27	Layout for Shock-on-Shock Experiment	54
28	Shock-on-Shock Experimental Data (Gage 1 Output)	57
29	Debris-Shielded Kulite Gage Sensing Scheme	61
30	Sensing Installation	62
31	Mount for DABS IE Driver-Pressure Bar Gage	63
32	Bar Gage Driver Pressure from DABS IE	65
33	Bar Gage Mount After Test	66

ILLUSTRATIONS (Cont'd)

<u>Figure</u>		<u>Page</u>
34	Kulite Gage Driver Pressure from DABS IE	67
35	Kulite Gage After Test	68
36	Principle of Magnetohydrodynamic Velocity Gage	68
A1	Doppler Signal from Rifle Bullet	76
A2	Density Effects	78
A3	Layout for Particle-Velocity Experiment	81
A4	Location of Radar Unit for Test	82
A5	Doppler Radar Signal	83
A6	Particle Velocity Versus Overpressure	84
B1	Conceptual Microwave Velocimeter	90
B2	Laser Beam Crossover Region	91
B3	Cross Section of Ellipsoidal Interference Region	95
B4	Doppler Difference Measurement Geometry	96
B5	Scattering Volume Assumptions	116
B6	Microwave Velocimeter, Tunnel Floor Installation Layout, Typical for 120° Beam Intersection at 10.525 GHz	119
B7	Ku-Band System Design	122
C1	Geometry of Blast Gage	129
C2	Propagation of Secondary Shock	131
C3	Propagation Direction of Secondary Shock	134
D1	Schematic for Faraday Velocity Gage	144
D2	TIGER Calculations of Expanded Explosive Gases	148
D3	Equilibrium Conductivity Calculations	150
D4	Experimental Setup of Shot 122-2	153
D5	Preshot Photographs of Shot 122-2	154
D6	Test Section and Electrode Detail	156
D7	Gas Conductivity Measurement	158
D8	Shot 122-4 Raw Data	161
D9	Shot 122-4 Reduced Data	162
D10	Shot 122-5 Diagnostic Setup	164
D11	Shot 122-5 Raw Data from Scope Traces	165
D12	Shot 122-5 Raw Data from Tape Deck	166
D13	Shot 122-5 Reduced Data	167
D14	AFWL Noise Test Raw Data	172

ILLUSTRATIONS (Concl'd)

<u>Figure</u>		<u>Page</u>
E1	Equilibrium Composition of Air	181
E2	Volume Absorption Coefficient Versus Wavelength for Soot and Fused Silica (T = 300°K)	183
E3	Data from Incident Shock Calibration on the CO First Overtone Emission	185
E4	CO ₂ 4.3- μ Band Emissivity Versus Wave Number for Pure Doppler Line Shape and Weak Line Approximation for T = 1500 K	186
E5	Spectral Radiance of a Blackbody, N_{λ} , at Temperature °K	188
E6	Example of Expected Emission from High Temperature Molecular Radiators in DAB Environment	191
F1	Blunt Cylinder Drag as a Function of Mach Number	198

TABLES

<u>Table</u>		<u>Page</u>
1	DABS ID Debris Distribution	43
2	DABS IE Debris Distribution	50
B1	Debris Total Weight 36.78 (g)	110

SECTION 1 INTRODUCTION

BACKGROUND

The United States Air Force has launched a program directed toward the development of a fourth-generation Intercontinental Ballistic Missile (ICBM) designated *Missile-X (MX)*. This development program is aimed at producing the technology and launch concepts for a large throw weight, survivable, highly accurate MIRVed* ICBM (ref. 1). This improvement in missile technology, specifically that related to accuracy, has led to the consideration of different missile-basing concepts. Present basing concepts for Minuteman rely upon hardened silos. The perceived possible improvements in missile accuracy will radically increase the hardness requirement for these silos or the alternative fixed-point basing concepts. This increase can be both impractical and extremely costly. Thus the Air Force is considering what is popularly called the *shell game* concepts. This simply involves an areal dispersion of potential targets not all of which contain a missile; e.g., two of the more popular concepts are the shelter and the trench. The shelter concept involves providing a number of semihardened, relatively inexpensive shelters for each missile. These shelters are dispersed over a given area and the missile is occasionally moved among them. Thus the probability of a direct or near direct hit is simply the inverse of the number of structures. In the trench concept, a long, shallow, underground tunnel is provided for the launch vehicle and the missile is randomly moved to different locations within the tunnel. In this case the probability of a near miss is inversely proportional to the length of the tunnel.

The concept of areal dispersion of potential targets, as opposed to superhard fixed targets, changes the mechanism governing the vulnerability. With superhardened, fixed-point structures the prime concern is directed toward cratering

* Multiple Independent Reentry Vehicle.

1. Slay, Alton D., Lt. Gen., USAF, "MX, A New Dimension," *Air Force Magazine*, September 1976.

and high-stress, ground-shock propagation. However, with areal dispersion the emphasis shifts to the airblast since the missile is most likely to be some distance from the crater region. It is for this reason that the Air Force has been developing a Dynamic Airblast Simulator (DABS). This simulator is being used to test the effects of airblast loading on some of the structures to be used in different basing concepts for MX.

DABS is sometimes referred to as a *disposable shock tube*. It simply consists of a roofed tunnel covered with an overburden which is driven by high explosives at one end. It is made as short as possible for cost reasons. Model launch structures are located on the floor of the facility and their response to the blast environment is measured.

Since the basic purpose of DABS is to generate a nonnuclear airblast, simulating the blast from a nuclear device at a given range, the blast wave produced must adequately represent that wave in both magnitude and waveform. This is somewhat difficult with DABS because of the short tunnel. It is necessary that the expanding detonation products, driving a clean air shock, be used to provide a significant portion of the blast loading on the structure being tested. Herein lies the basic difficulty for both the theoretician and the experimentalist. The thermodynamic equations for shocked air are quite well known. This is not the case for the detonation products; no really adequate equation-of-state exists. With no adequate model, the burden of parameterizing this portion of the flow falls upon the experimentalist. However, the difficulty of making measurements in the detonation products is quite great, since the atmosphere is composed of unknown constituents at unknown temperatures and is loaded with debris. As far as the theoretician is concerned, the prime variables that need to be measured in reference to the shock wave are the side-on or incident pressure, the shock velocity, and the dynamic pressure in the shock wave. The first two are quite easily and routinely measured; the third is not so easily obtained. If one defines ρ as the density in the flow, V as the flow velocity, and Q as the dynamic pressure, $Q = \rho V^2/2$.

OBJECTIVE

The prospects for measuring the dynamic pressure directly are quite slim. The flow velocity can be measured but there is no reasonable prospect for measuring the density of this dirty flow. Thus, this instrumentation development was directed toward the creation of measuring techniques that could parameterize the flow in such a manner as to obtain the variables from which the dynamic pressure could be inferred. These variables include the flow velocity, the velocity of the interface between the air and the detonation products, stagnation pressure, temperature, mach number, and driver-chamber pressure. Methods to accomplish this objective were thus investigated.

This investigation was carried out on a series of test events, termed the *DABS-I Series*. The purpose of this series was twofold--to develop the techniques necessary to generate an appropriate blast waveform and to create an environment in which the developmental instrumentation could be tested.

SECTION 2 MICROWAVE SYSTEMS

DOPPLER RADAR

Introduction

The use of relatively inexpensive traffic-control doppler radar systems to make velocity measurements in shock waves is clearly one of the more novel and significant advances in the instrumentation development program for DABS. A mass-produced, commercially available item, with minor modification, has been adapted to high velocity experimental work. Thus, a relatively sophisticated microwave system can be obtained at a cost less than that of a normal blast-pressure gage.

Radar experiments were fielded on DABS IA, IC, ID, and IE. The first of these experiments on DABS IA was previously reported at the Defense Nuclear Agency Blast and Shock Instrumentation Conference at the Waterways Experiment Station in October 1975. Briefly, this paper (appendix A) describes how a radar unit was used to track an aluminum-foil target after it was impacted by the shock wave. The resultant velocity was 4489 ft/sec. This velocity corresponds with the expected particle velocity in air shocked to 327 psi, a value which agreed with the pressure readings and with the measured shock velocity. This Lagrangian particle velocity measurement, although quite useful in checking out the system, only proved that the ratio of the isobaric to isovolumetric specific heats was 1.4. This was already known for clean air and thus the experiment simply confirmed this but served more as a check on the measurement system.

One of the prime problems associated with DABS is that the explosive products are used as a significant portion of the loading. The equation-of-state for these gaseous products combined with debris is unknown. Thus, making measurements that parameterize the explosive products is extremely important. It is to this end that the additional radar experiments were directed.

Possibly, the interface between the explosive products and the driven clean air shock can be tracked by a single radar unit looking down the DABS tunnel. The

primary question to be resolved was whether this interface would be reflective or transparent. As shown in appendix A, the prime variable affecting the reflectivity is the free-electron concentration in the hot gases. When the incident microwave radiation is 10.525 GHz, the interface will be reflected when the free-electron concentration is high enough to cause a plasma frequency of 10.525 GHz. In the clean air portion of the shock wave the electron concentration at which the peak pressures are nominally 600 psi, the free-electron concentration does not achieve this value. However, at the interface between the explosive products and the clean air shock the situation is quite different. The explosive used as the driver (PETN) is oxygen deficient, and as a result, a state of combustion exists at and near the interface. This combustion is continually supported (during the time frame of interest) primarily by the oxygen in the air mixing with the detonation products as a result of turbulence. The characteristics of this interface are controlled by the rate of reaction of the unknown nonequilibrium detonation products with the air. Thus, the plasma characteristics of the interface are determined by the rate of mixing along the interface and what the nonequilibrium products are. The present data preclude the possibility of determining these quantities. The only facts known are that the nonequilibrium products burn (photographically observed) and that this burning probably occurs in a manner consistent with the formation of a large number of free electrons. These electron concentrations could easily approach or even exceed the 3.5×10^{10} electrons/cm³ needed to totally reflect the radar beam. Obviously, this hypothesis needed experimental investigation. Thus a radar experiment was fielded on DABS IC to test this hypothesis. The results of this experiment were used in the subsequent experiments to direct modifications.

Radar Unit

The radar unit used in all the experiments was a Model JF100 Speed Gun manufactured by CMI, Inc., Minturn, Colorado. In its normal configuration it is a hand-held, traffic-control, doppler radar unit which digitally displays velocity in miles per hour. The pertinent specifications as given by the manufacturer are as follows:

- (1) Frequency -- 10,525 ± 25 MHz
- (2) Polarization -- Circular

- (3) Beam Width -- 8° or Less (Side lobes suppressed greater than 24 dB down)
- (4) Antenna -- 4-Inch Aperture; Circular Horn Type
- (5) Microwave Oscillator -- Solid-State Gunn Diode
- (6) RF Power -- 20 mW Minimum; 100 mW Maximum
- (7) Receiver Diode -- Schottky Barrier Type Rated for 100-mW Burnout

The unit was ordered without the digital display or its associated electronics since they were not pertinent to the experiments. Thus, the total unit consisted of an antenna, a preamplifier, an amplifier/regulator, a 9-V regulator, and the housing. The system was powered by a 12-V wet cell.

Experimental Procedures

In DABS IA the signal was taken from the output of the preamplifier and ac-coupled (high pass 30 Hz, 3-dB point) because of a dc-offset. The only other modification made was the removal of all low-pass filtering from the preamplifier. The output impedance of the system was 1000 Ω .

The relatively high output impedance in DABS IA prompted a change to the radar system for DABS IC. To improve the frequency response, a buffer amplifier powered by a 45-V battery (fig. 1) was used as a line driver. This amplifier was an inverting unity-gain device with a 1000- Ω input impedance and a 75- Ω output impedance. This modification negated the need for ac-coupling on the output. After this modification was made, the system was checked out with a rifle bullet as a high-velocity target. (The procedure described in appendix A was used.) The results (fig. 2) agreed quite well with the previous rifle data and the expected bullet velocity. Also the previous offset problem described in appendix A was eliminated by the buffer and a terminated line.

The output of the radar antenna was ac-coupled (high pass) to the input of the preamplifier for all experiments after those on DABS IC. This was accomplished by a simple one-pole RC filter which was formed by connecting a 0.005 μ F capacitor in series between the antenna and the preamplifier. Since the preamplifier was 1000 Ω , this formed a high-pass filter with a 3-dB point of 32 kHz. The recorded signal was the amplified doppler signal, and its relationship to the velocity of the target was $f_d = 2v_r/C$, where f_d is the doppler frequency,

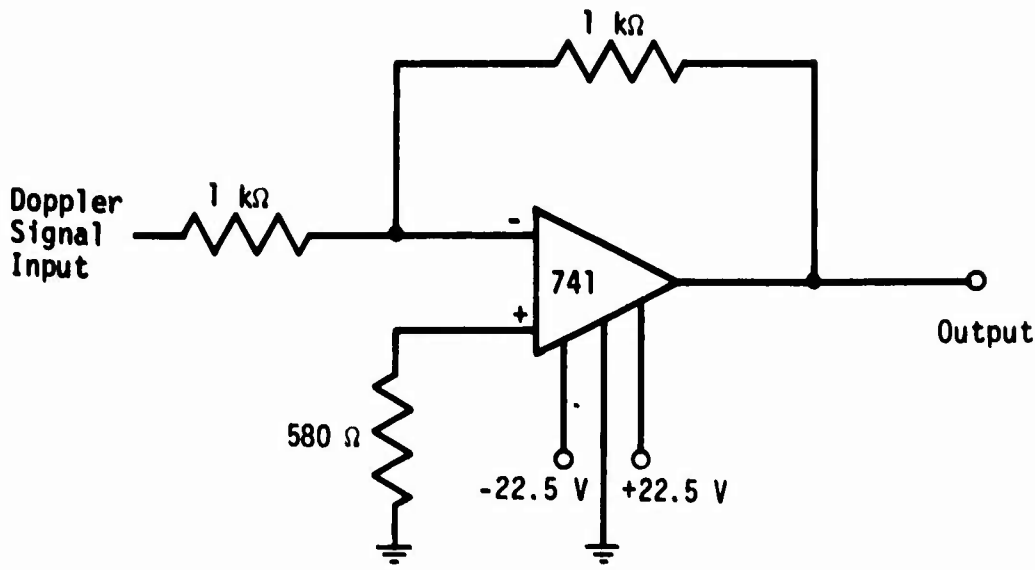
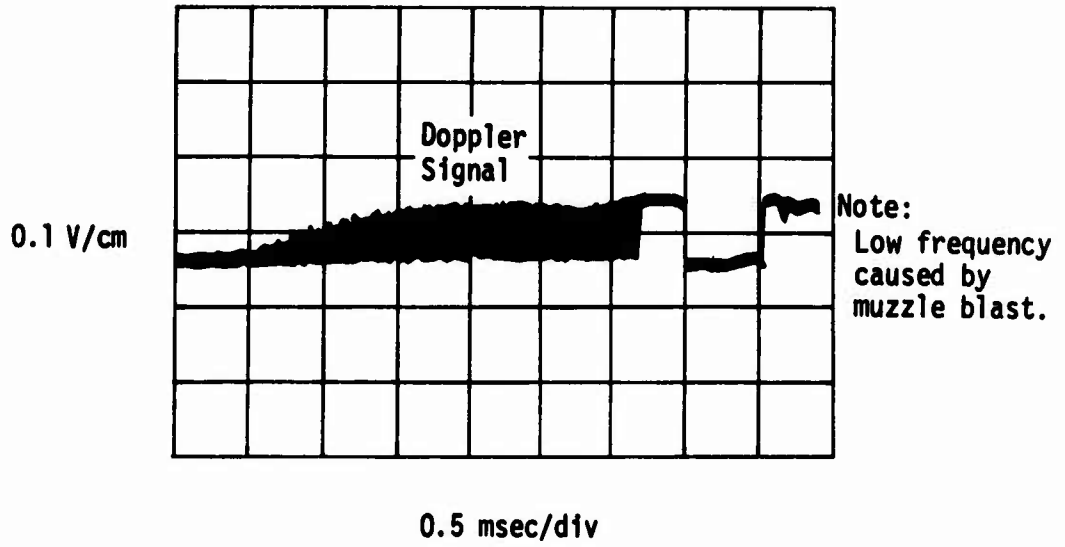


Figure 1. Radar Buffer Amplifier

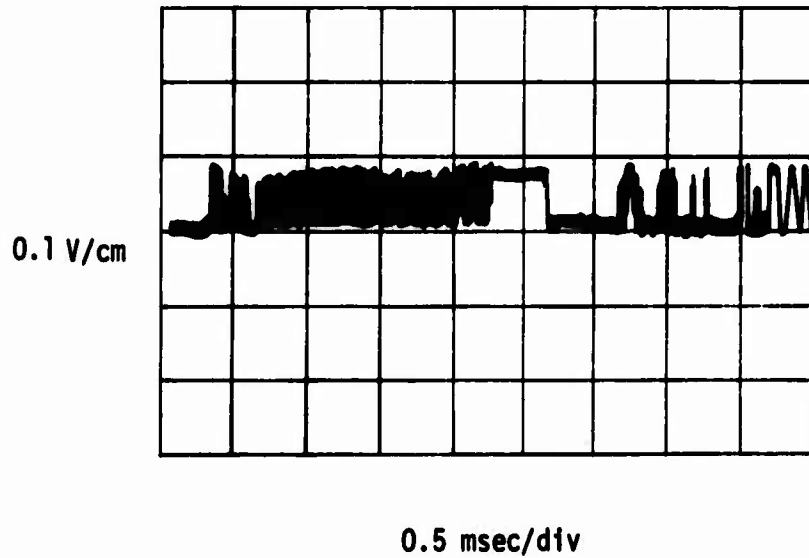
V is the velocity of the target, f_r is the radar carrier frequency, and C is the speed of light. If the unit of velocity is feet per second and the frequency is in Hertz, this equation reduces to $f_d = 21.40V$.

For each of the experiments the data were recorded on a Bell & Howell 3700 B Tape Recorder. With the exception of the DABS IA data, all data were recorded with Wideband II FM (500-kHz frequency response). On DABS IA the signal was transmitted by RG213 cable which was not terminated. This was necessary because of the high output impedance of the preamplifier; however, this was not necessary on the subsequent experiments, since the buffer amplifier was used. A terminated RG58 line was used for these tests. In all the experiments the line was approximately 1000 ft long.

In all cases, the radar unit was aimed down the center of the tunnel and placed so that debris created after impact by the shock wave would not interfere with other experiments in the DABS facility. No attempt was made to harden the



(a) Bullet Fired Toward Radar Unit



(b) Bullet Fired Past and Away From Radar Unit

Figure 2. Doppler Radar Signal from 7-mm Magnum Bullet

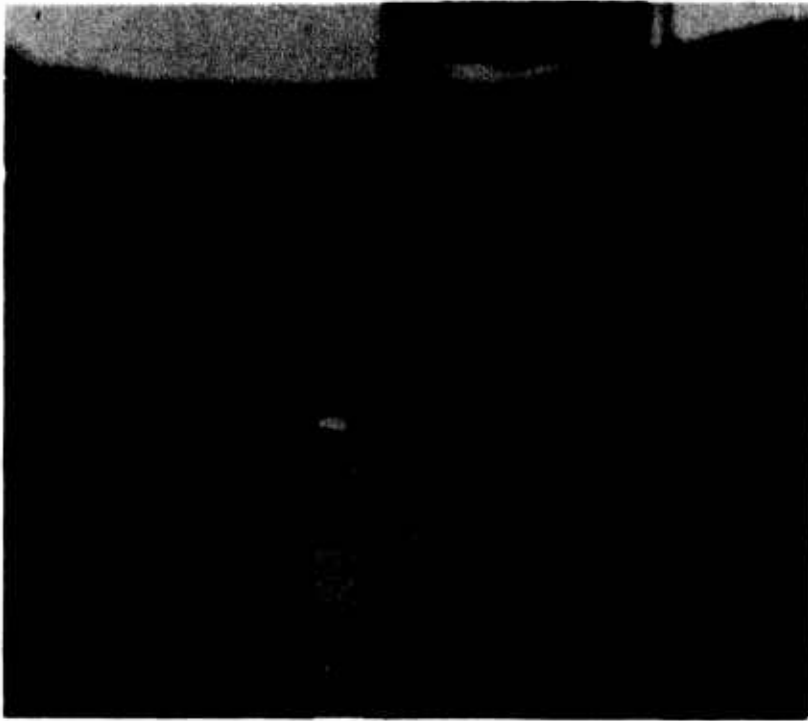


Figure 3. Radar Unit

radar unit to the effects of the shock wave. This would have involved building a bunker with a thick quartz or Teflon window for the radar unit to look through; the cost would far exceed the cost of the radar unit. Thus, the radar was presumed to be disposable and was simply mounted on a wooden stake (fig. 3), usually inside the DABS tunnel.

With the exception of DABS IA, there was no metal target placed in the tunnel, since the objective was to track the interface between the detonation products and the clean air shock. Thus, the DABS IC radar test was performed to determine whether or not the interface between the detonation products and the clean air shock would reflect the microwave radiation. The possibility of another type of microwave system (discussed later) prompted interest in the propagation of a microwave beam of 10.525 GHz frequency through the detonation products. This additional information made the experiment quite unique from the experimentalist's point of view. The fact that the wave could propagate through the shock front had been established in DABS IA. Thus, there were only three possibilities: (1) the beam would be reflected by the interface between the detonation

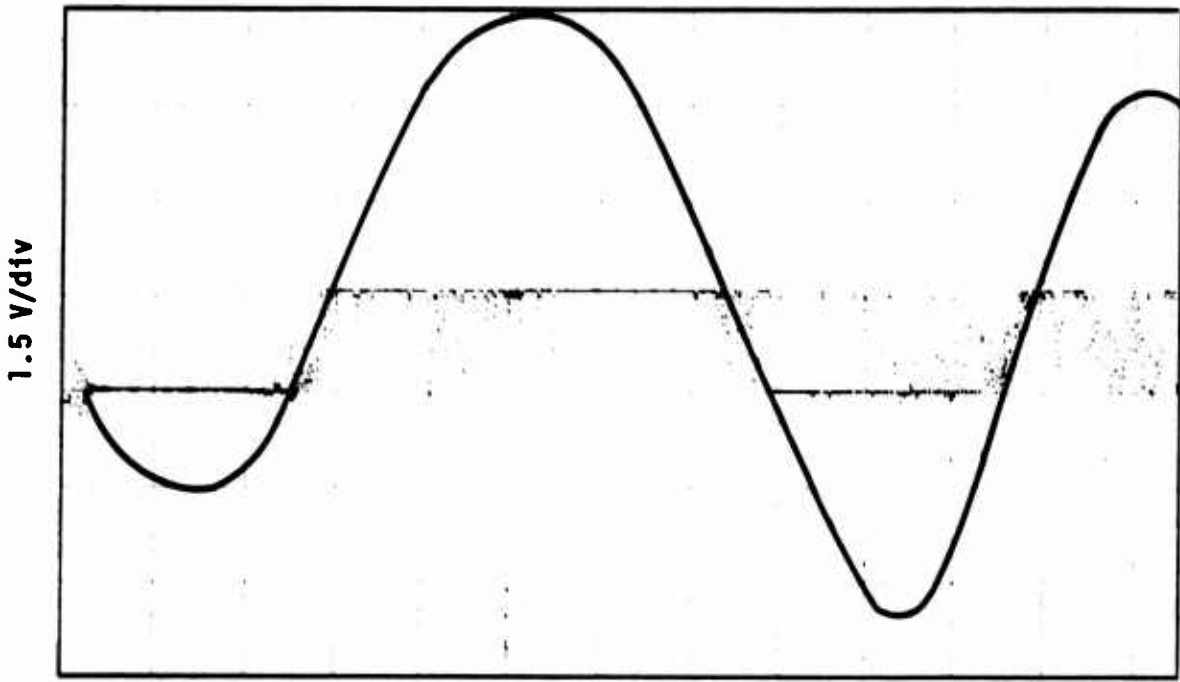
products and the clean air shock; (2) the beam would be reflected only by the back walls and thus be transmitted through the detonation products; or (3) the beam would be totally absorbed by the detonation products and thus there would be no return signal. Obviously, the first two possibilities are the most desirable, but all three cases represent meaningful data. Thus, excluding the possibility of a severed cable, even no return signal would be meaningful.

Results

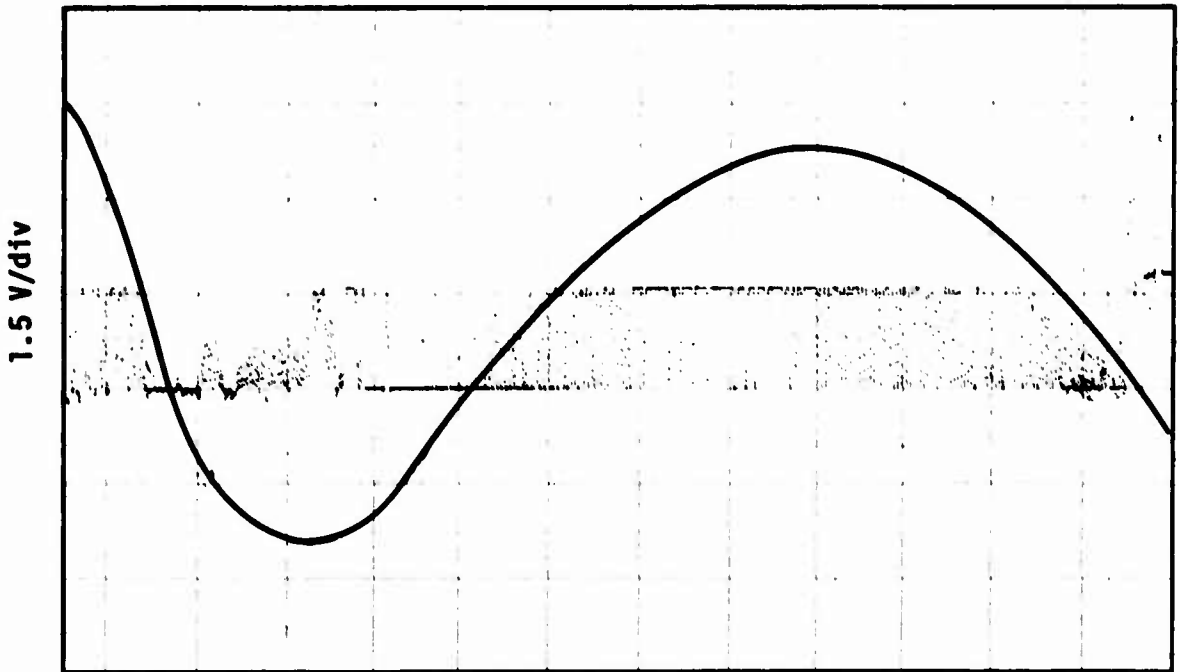
The results of the DABS IC radar test were quite interesting in that they showed that the radar unit did track the interface between the detonation products and the clean air shock and also that the beam was transmitted through the interface and reflected off the rear wall. The raw data are shown in figure 4. These data show that there were high-frequency data superimposed on low-frequency data. The reason for this can be seen by means of the overlaid drawing on the raw data. The low frequencies represent velocities that varied from 12 to 39 ft/sec. These values qualitatively agreed with the photopole data. Thus, they represent the velocity of the wall behind the driver section in DABS. The obvious clipping of the data was caused by the radar unit itself--specifically the maximum output voltage of the integral preamplifier. Thus, all data above or below approximately ± 1.5 V were lost because of clipping in the preamplifier. This led to a reduction in the number of high-frequency data points, which are presumed to represent the velocity of the interface.

The reduced doppler frequency is shown in figure 5 along with the difference between it and the shock velocity. This latter curve can be integrated to determine the distance between the clean air shock front and the interface between the detonation products and clean air shock. These data were obtained by measuring the period of the oscillations and converting that to frequency. This was accomplished with 50- μ sec/in plots.

The knowledge that the 10.5-GHz beam could propagate through the detonation products was useful as a design criterion for the second microwave system investigated. However, the low-frequency data superimposed on the high-frequency data severely limited the amount and continuity of the high-frequency data, which are of prime interest.



0.4 msec/div



0.4 msec/div

Figure 4. Raw Data from DABS IC

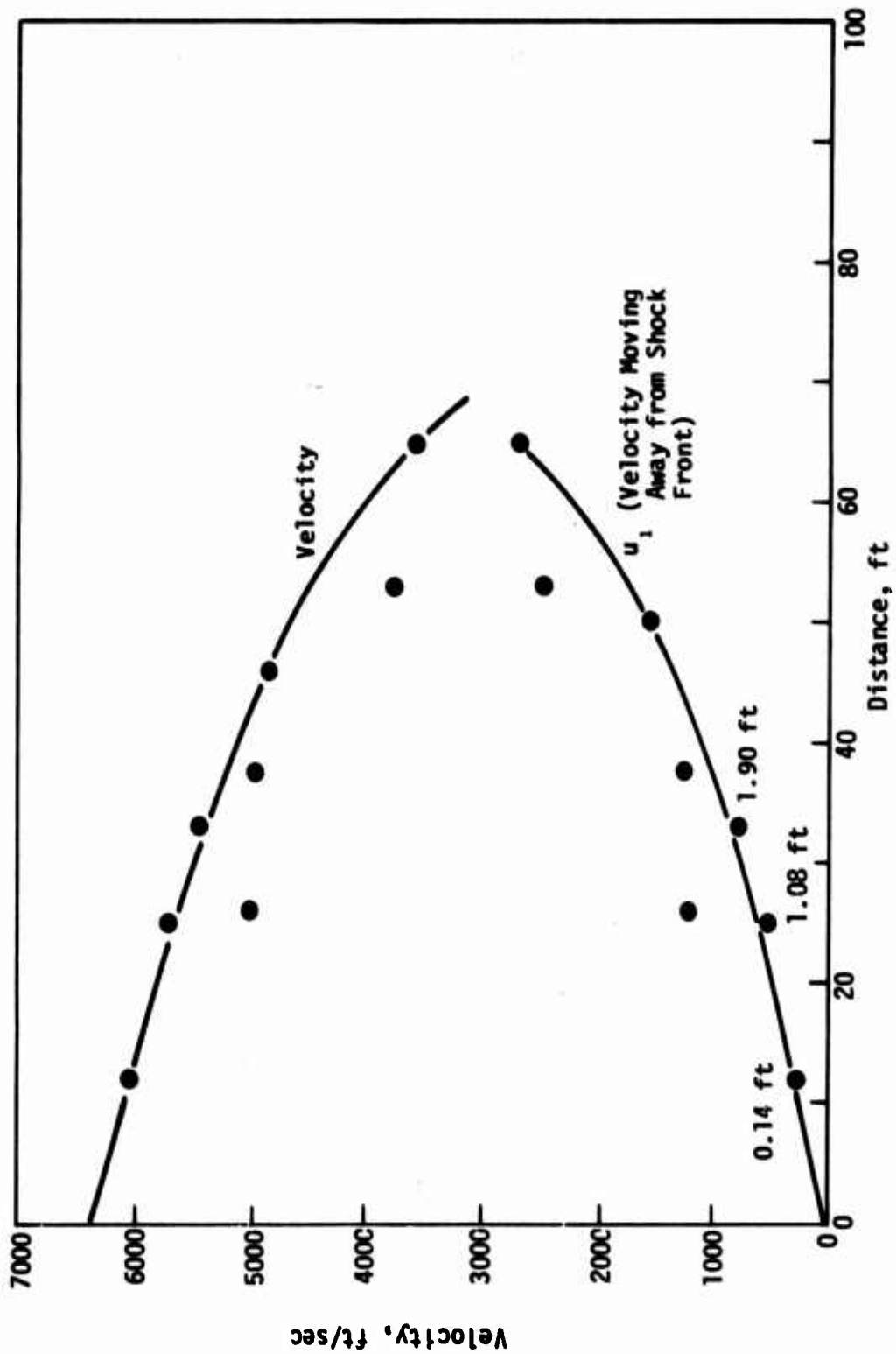


Figure 5. Radar Velocity Data from DABS IC

On DABS ID and IE the input to the preamplifier was, as previously described, high passed. As can be seen in figures 6 and 7 the quantity of high-frequency data was radically increased. There was some low-frequency data retained because of the extremely high gain of the preamplifier ($\approx 10^6$). Figures 8 and 9 show the reduced data from these two tests.

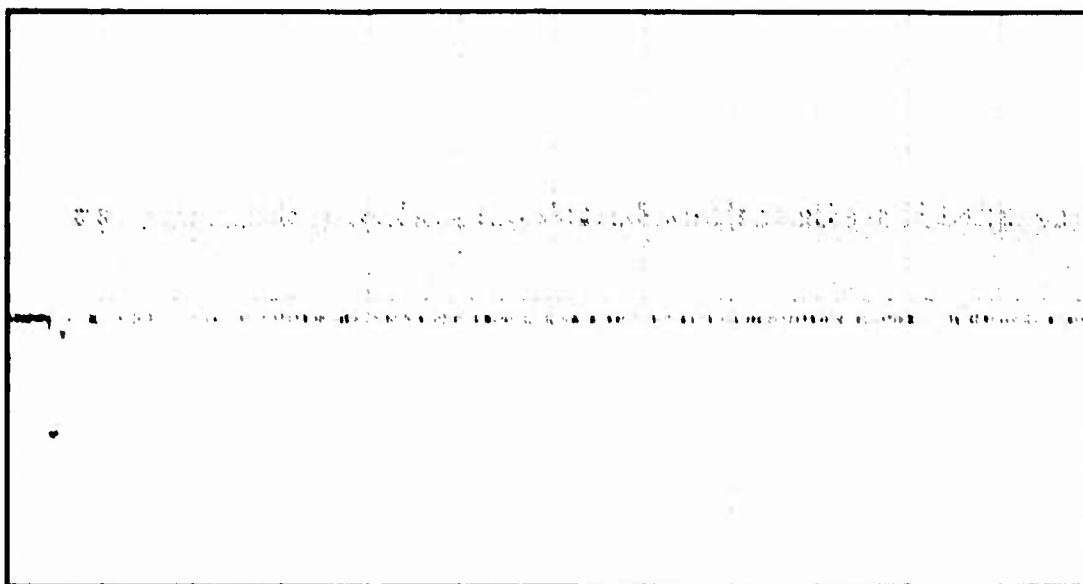
The velocity data from DABS IE (fig. 9) were extremely interesting in that there were some obvious oscillations on top of the data. These oscillations, which varied in period from approximately 3 to 5 msec, were probably due to the excitation of a transverse mode in the DABS IE tunnel (the tunnel was 13 ft wide). This would tend to indicate that the acoustic velocities back in the flow varied from 2600 to 4300 ft/sec. Although these results were interesting and believable in magnitude, the precision of the measurement was certainly limited by the scatter in the data. That this appears only on the DABS IE data is due to geometrical reasons. The DABS IE tunnel was the largest tunnel, and since it was the only one with a sloped roof design, there was only one direction (parallel to the floor) that a transverse mode could be excited. The oblate DABS IA was certainly not conducive to this effect, nor were the DABS IC and ID, since they were constructed with flat roofs. However, in these latter cases, there existed the possibility of exciting two different transverse modes of different frequency and phase.

Based on the velocities inferred from the radar data, the radar beam tracked the interface between the detonation products and the clean air shock or the debris right behind it. Another possibility that should be recognized is that the use of oxygen-compensated explosives such as ANFO or slurry may not be advantageous to the radar system. The absence of a burning interface between the detonation products and clean air shock may allow nearly complete transmission of the beam. This will have to be tested.

PARTICLE VELOCIMETER

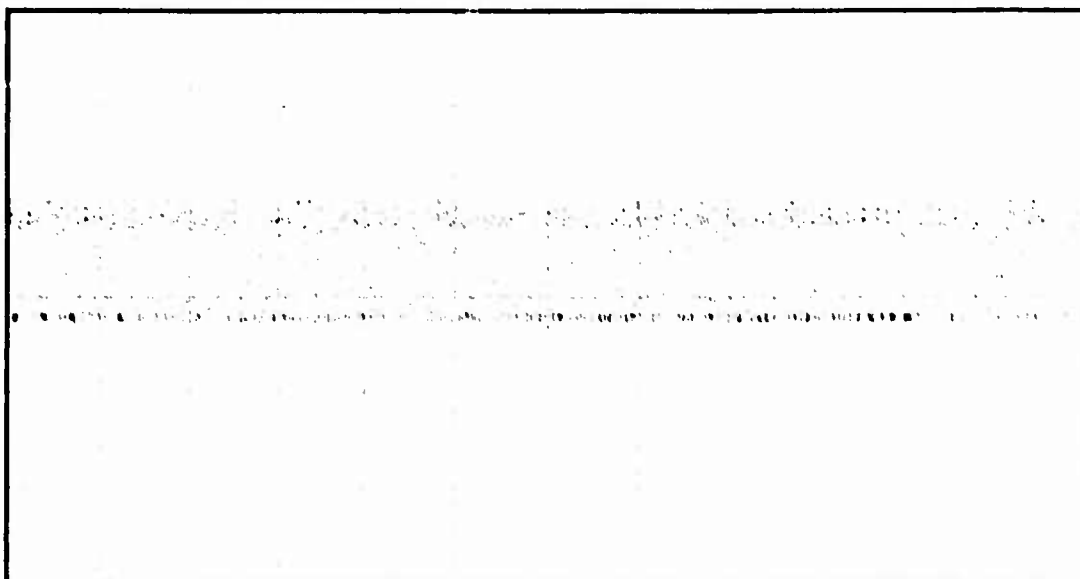
The secondary result of the DABS IC experiment, viz., that the beam could see through the detonation products, was of prime importance in the possible development of an Eulerian particle velocimeter for DABS. Figure 10 shows the layout of the proposed system. It is the exact analog to a LASER velocimeter.

1.5 V/div



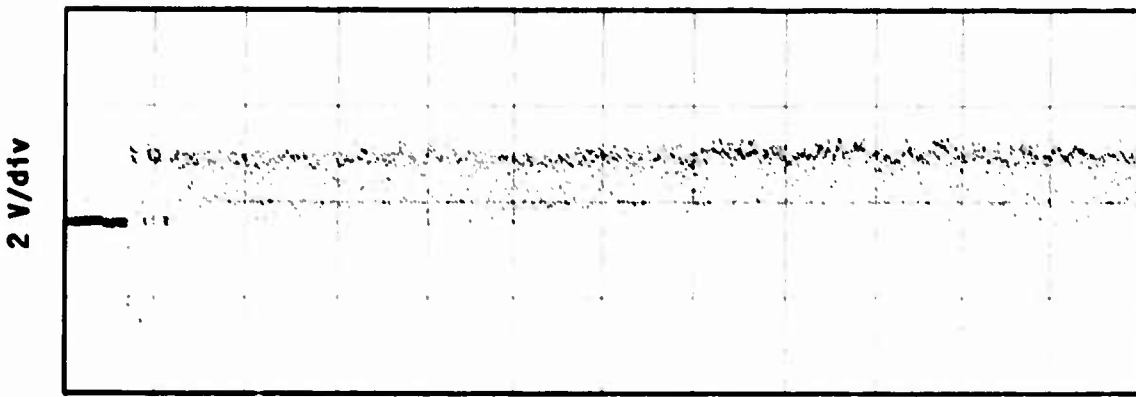
0.4 msec/div

1.5 V/div

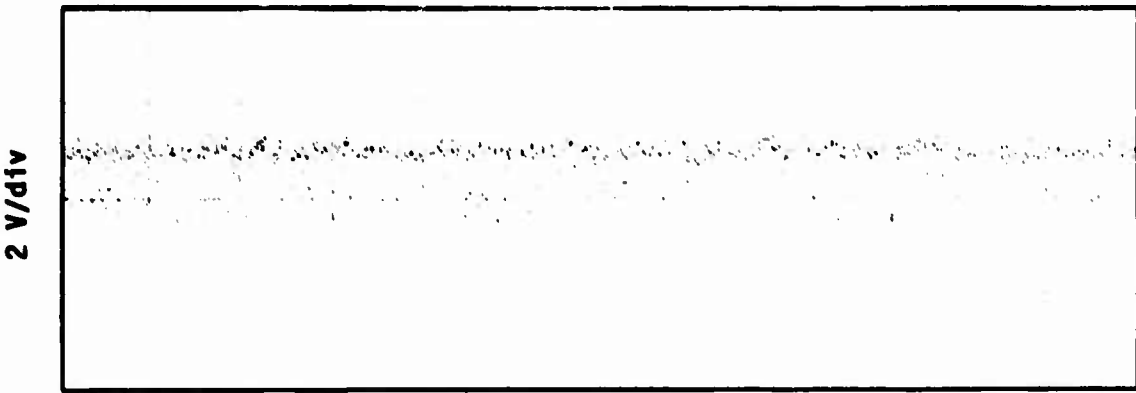


0.4 msec/div

Figure 6. Raw Data from DABS ID



0.4 msec/div



0.4 msec/div

Figure 7. Raw Data from DABS IE

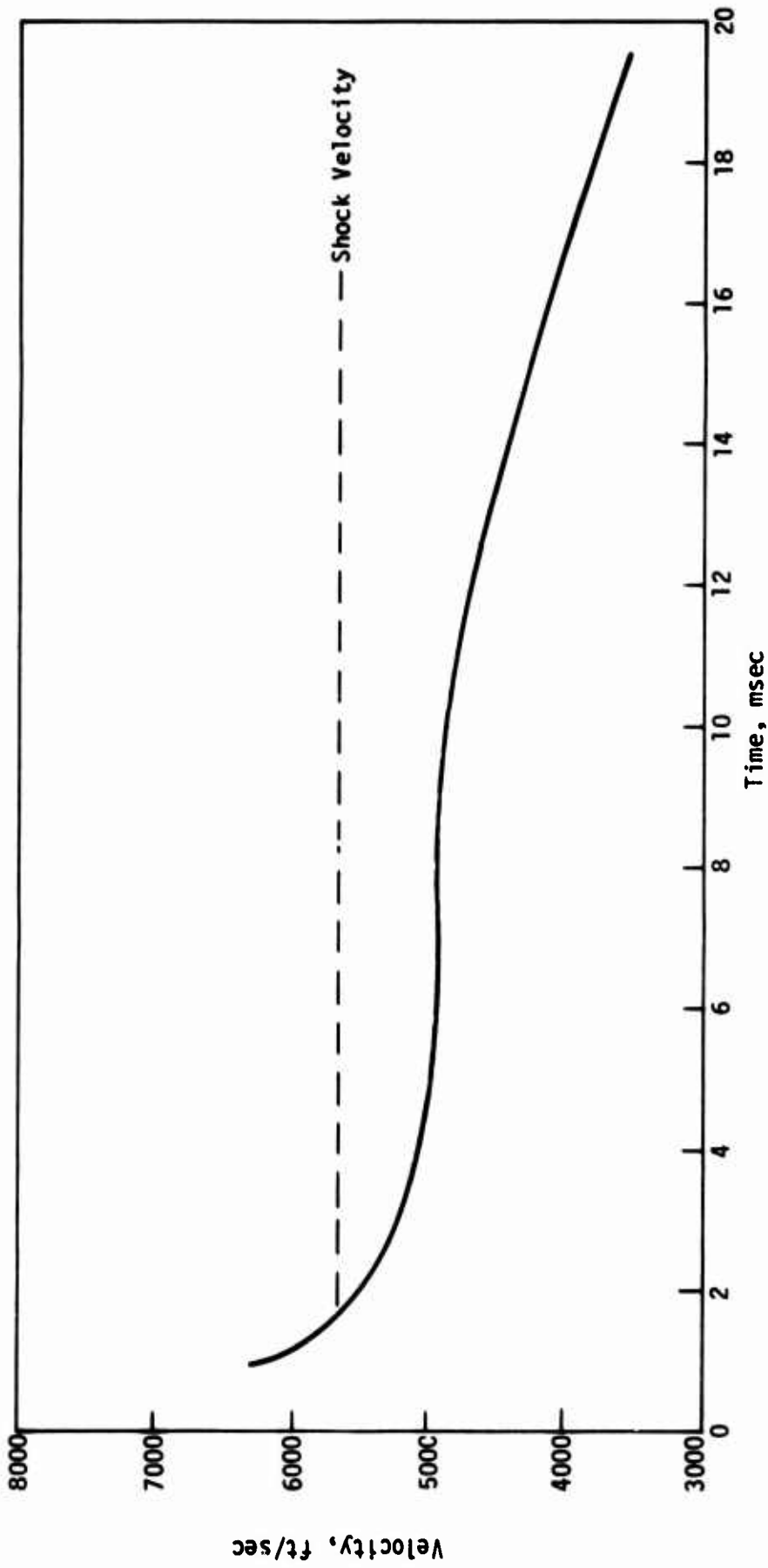


Figure 8. Radar Velocity Data from DABS 10

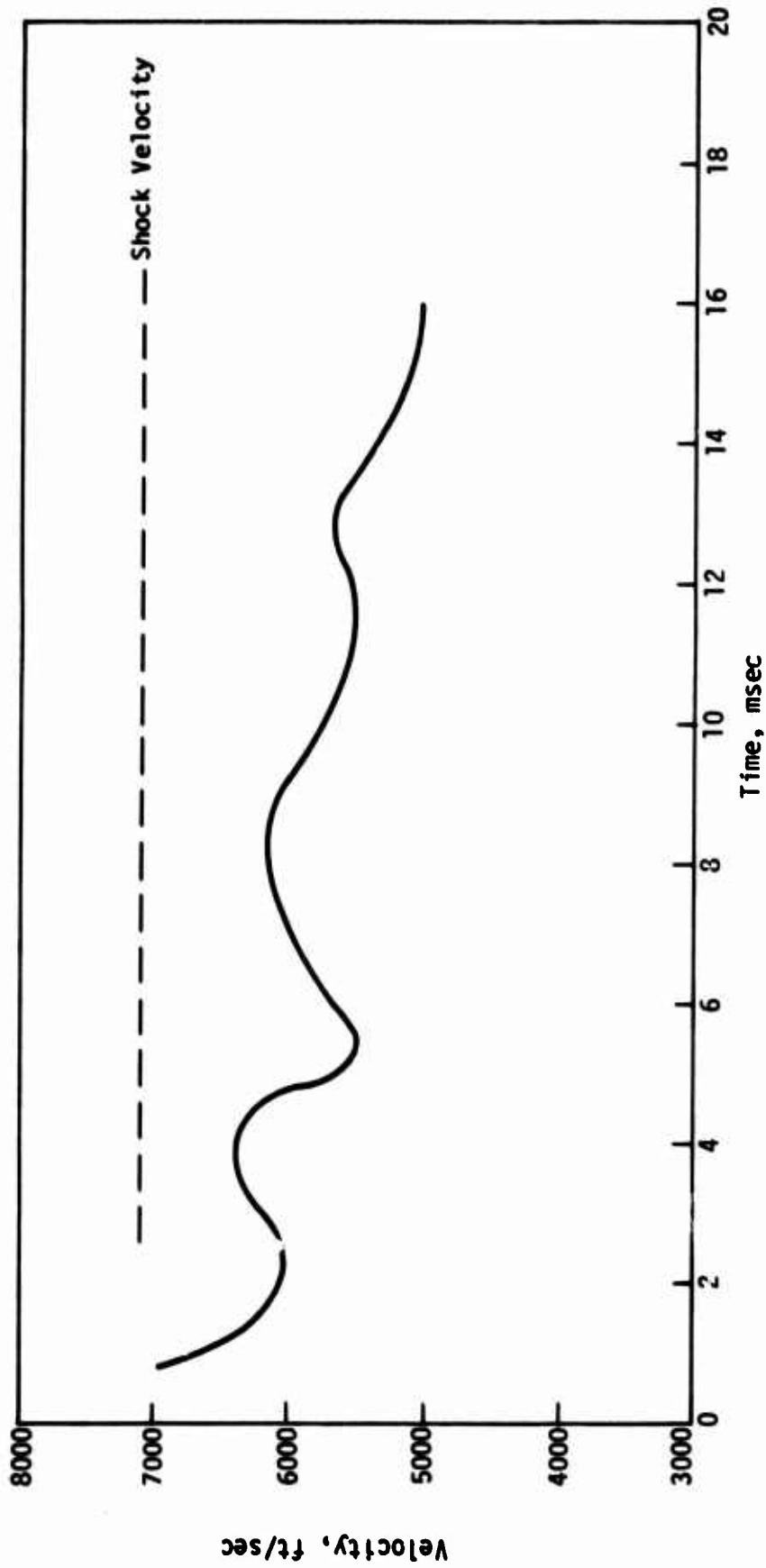


Figure 9. Radar Velocity Data from DABS IE

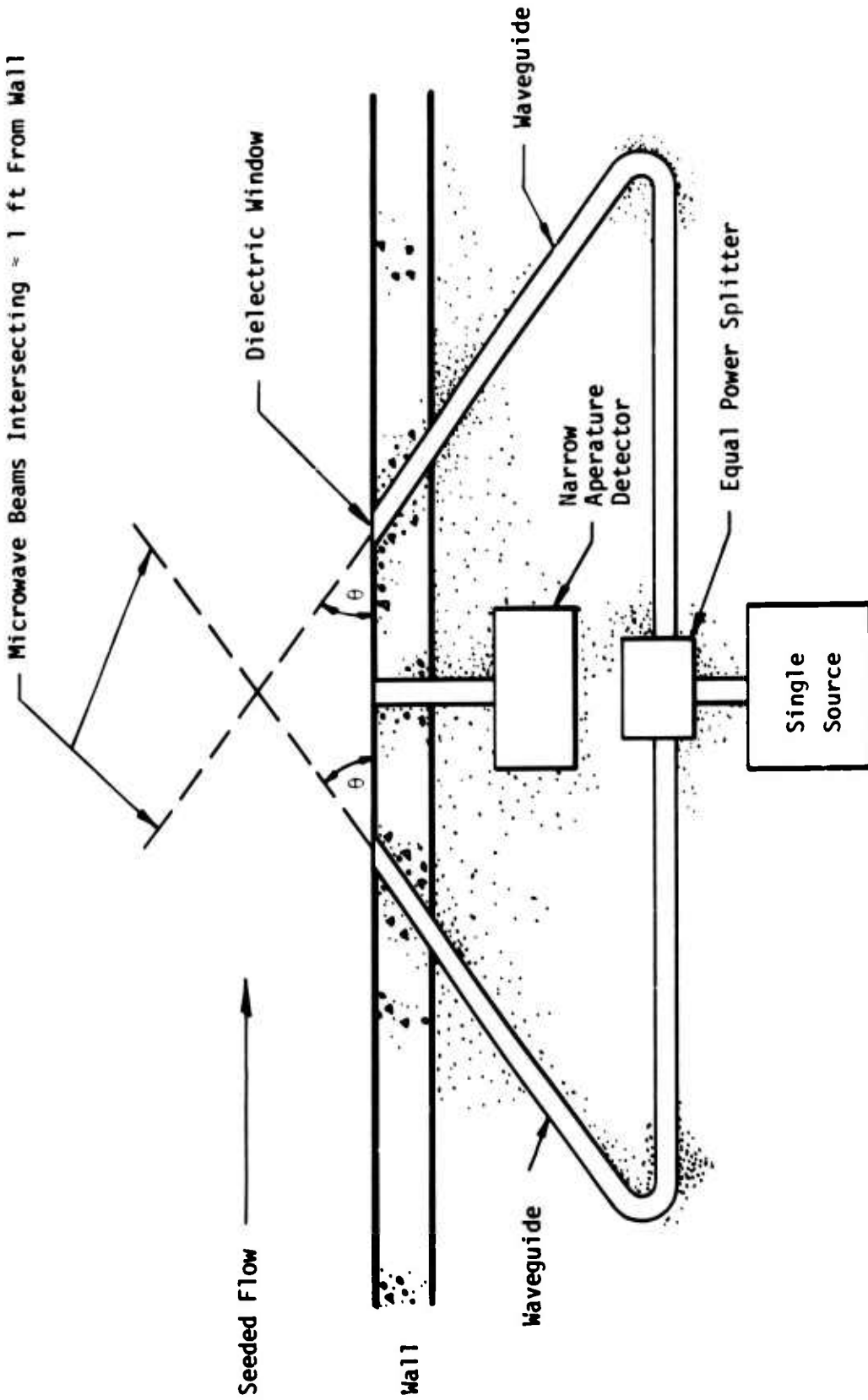


Figure 10. Microwave Particle Velocimeter System

Since it was believed that the extremely dirty atmosphere in DABS would not adequately transmit optical radiation, the particle velocimeter was chosen. However, when the debris particles are small compared to the wavelength, as in the case of microwave radiation, the beam can be transmitted.

The particle velocimeter system was originally proposed by the author to the personnel at the Radar Target Scattering Facility, Holloman Air Force Base, New Mexico. Their evaluation of the proposal was that it might work with their existing 100-GHz unit. The reason for this choice of the millimeter wave band was that there are fewer problems at the higher frequency associated with transmission through hot gases. The reason it was not fielded on the DABS series was that, if it did work, the cost of procurement and construction of a complete unit would be prohibitive (more than \$350,000). However, the fact that the 10.5-GHz beam propagated through the plasma opened the door to the use of frequencies in this range and thus the costs have been significantly lowered. As a result, the University of Texas Applied Research Laboratory was funded to do a feasibility and cost study of the proposed system. The results of this study are presented in appendix B. From the study it was recommended that a 16.2-GHz source be used in a geometry similar to that proposed. Theoretically, this system is sound and if it is financially feasible, it should be constructed and tested for DABS.

SECTION 3 INFRARED DETECTOR

Some photographic experiments were performed on DABS IA. High-speed motion-picture cameras photographically recorded the motion of an MX type pool as the shock wave passed over the water. Thick glass windows were used beside the pool and a light was shone through the pool for illumination.

The results of these experiments were quite confusing. Shortly after the shock arrival, the atmosphere above the pool turned completely black, i.e., the atmosphere appeared opaque to visible radiation. This led to some speculation about the possibility of treating the atmosphere as a black body. If this could be done, the temperature could be determined from the infrared spectrum emitted from the shocked gases. This can be shown by Planck's Black-Body Distribution Function, viz.,

$$I(\lambda, T) = \frac{2\pi C^2 h}{\lambda^5 \left(e^{\frac{Ch}{\lambda KT}} - 1 \right)}$$

where $I(\lambda, T)$ is the intensity as a function of the wavelength, λ , and absolute temperature T ; C is the speed of light; h is Planck's constant (6.6252×10^{-34} Joule-sec) and k is Boltzmann's constant. Figure 11 shows a plot of this function for different temperatures. Thus, if narrow bandpass filters are used on a number of different wavelengths, it can be determined if the spectrum is that of a black body, and if it is the temperature is uniquely defined.

The first experiments were directed toward developing the gage package for DABS. Since the interface between the detonation products and the clean air shock is burning, a plain infrared detector should be able to detect its arrival time. The information gained from this type of experiment would not only provide a functional check of the infrared system but also a cross check with the radar data to determine whether or not the detector was really tracking the interface. This approach was taken first primarily because of the increased complexity and cost inherent in making a five-channel instrument with narrow bandpass filters. This latter experiment would be undertaken only if the first was successful.

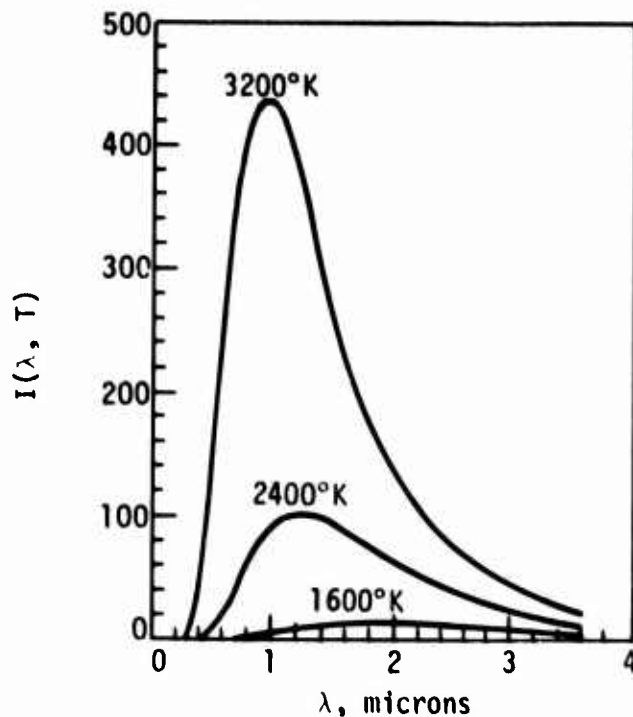


Figure 11. Spectral Distribution of Black-Body Radiation at Various Temperatures

The first event on which an infrared detector was used was DABS ID. This detector was a lead selenide photoresistor (Model No. 4007) manufactured by Infrared Industries. It has a 1- μ sec time constant and a response as shown in figure 12. This detector was chosen because of its sensitivity in the appropriate range of wavelengths (fig. 11), and since the van recording capability was limited to 20 kHz, the 1- μ sec time constant was considered adequate. The conditioning circuitry is shown in figure 13. Ac-coupling into the operational amplifier was necessary in order to block the dc offset of the detector when the power source (500 Vdc) was turned on.

The mechanical design for the mount is shown in figure 14. It consisted of a 2-in-diameter (inside) pipe, 4 ft in length. The bottom of the pipe was covered and it had a 1/4-in-wide slit through the mounting flange. A second slit was used to limit the field of view of the detector. These slits were oriented in the DABS tunnel so that they would be parallel to the shock front. The detector, suspended by three threaded rods which were mechanically coupled to the

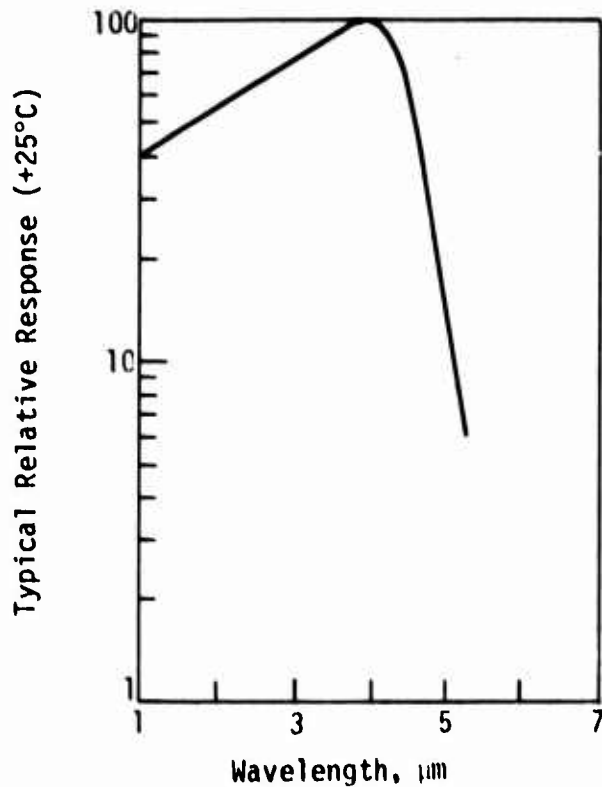


Figure 12. Infrared Detector Response

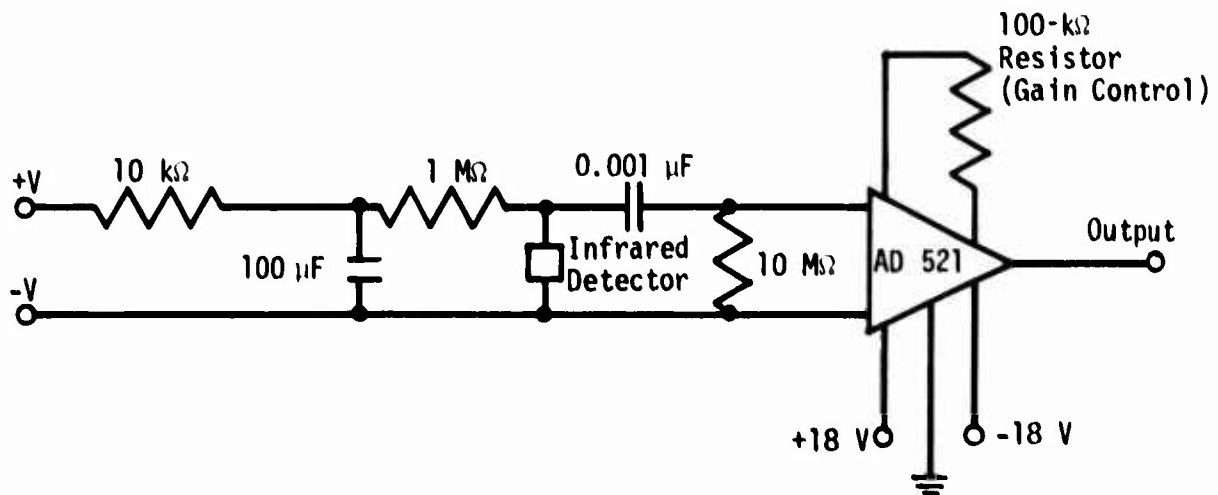
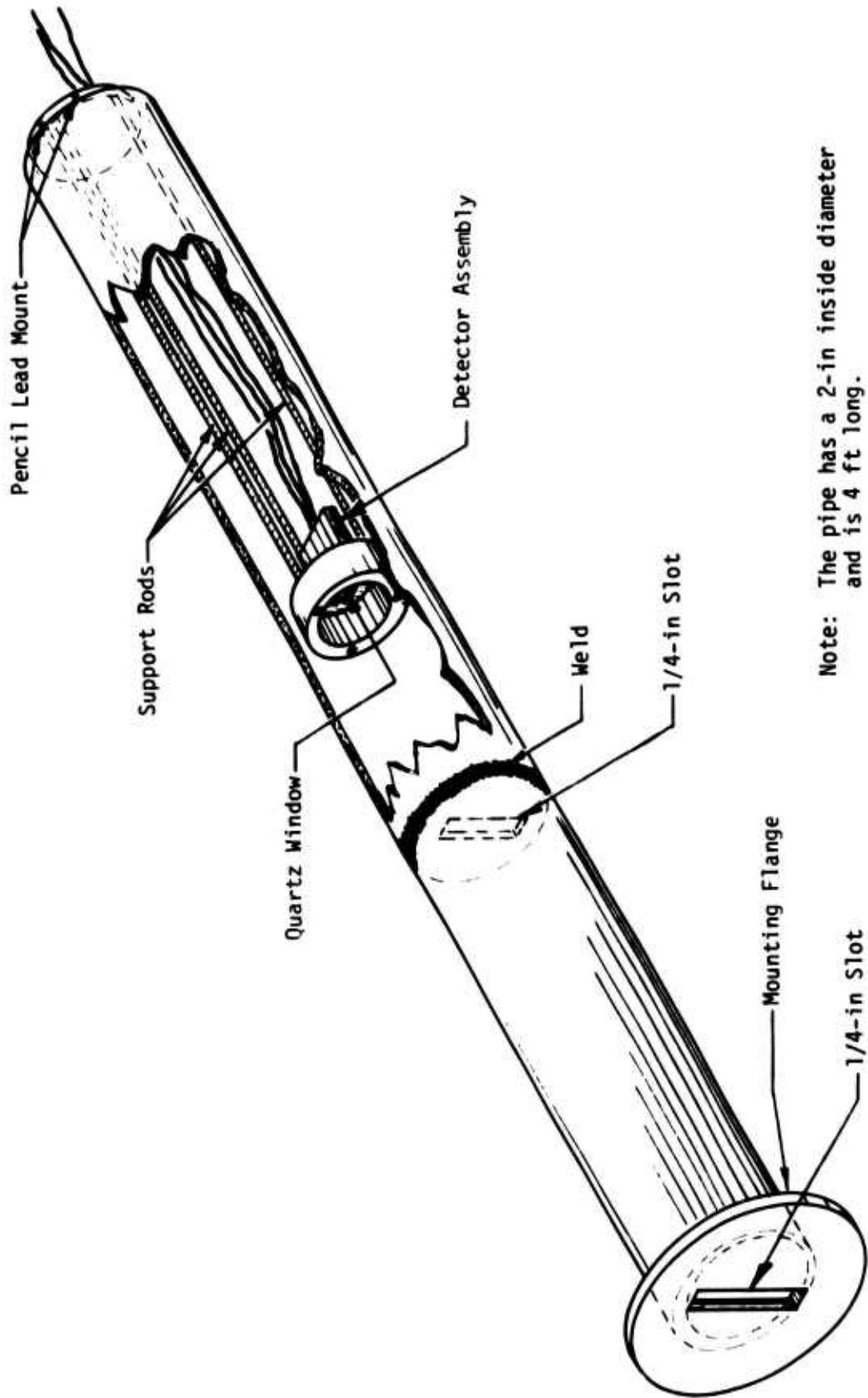


Figure 13. Infrared Detector Circuitry on DABS ID



Note: The pipe has a 2-in inside diameter and is 4 ft long.

Figure 14. Mount for Infrared Detector

pipe through pencil leads, was dropped down 2 ft into the pipe. The purpose of this mount was to ensure that when the shock wave passed under the detector and propagated up the pipe walls, the detector would free fall and thus be isolated from the shock. A quartz window was added for further protection of the detector. The calculated fill time for the cavity produced in front of the detector was 20 msec and thus the detector could be expected to function correctly for this length of time. However, when the oxygen-poor detonation products enter this cavity they will begin to burn and cause an illumination visible to the detector. This problem can be alleviated simply by locating the quartz window at the bottom of the pipe. Although this problem was recognized it was not acted upon simply because of procurement time and not knowing when the quartz window would arrive. However, because of the design used the expected signal would be a monotonically increasing function until after shock arrival because of secondary scattering of the molecules in the air (primarily CO_2). When the detonation products initially arrive, a saddle point or peak should be achieved. After the burning interface between the detonation products and the clean air shock passes, the unburned detonation products will begin to burn in the cavity beneath the detector.

Before insertion on DABS ID, the detectors were checked with a Sandia Laboratories black-body source in conjunction with an iris and camera shutter. The iris was set so that the detector would have the same field of view as it would in DABS and the camera shutter was used to give the fast rise-time pulse necessary because of the ac-coupling (15 Hz high pass). The signal, observed on an oscilloscope, was approximately 10 V for all the detectors when the black-body temperature was 2000°C. This agreed with detector sensitivity calculations and thus the detectors were installed.

Four detector packages were installed on DABS ID. These packages were installed in the roof at 25.21, 48.25, 75.21, and 99.33 ft from the explosive-driver end of the DABS facility. Two of the packages failed before the test. It was presumed that the input was overloaded. This caused a failure in the operational amplifier power supply, which resulted in a large dc-offset signal. However, since this occurred during the countdown, there was no effort made to repair the detectors.

The infrared data are shown in figure 15. Figure 15a shows a peak at shock arrival (determined from time-of-arrival measurements). This was probably caused by the fact that at close-in stations the shock front itself is quite hot. The next large peak (0.9 msec later) was probably the arrival of the detonation products. However, the existence of a peak and saddle point between 4.0 and 4.7 msec makes this doubtful. From strictly shock-propagation considerations, it seems that the first large peak (0.9 msec after shock arrival) is the arrival time of the detonation products. The second trace (fig. 15b) is much more classic in nature. At shock arrival the signal began to increase in magnitude to a saddle point and then increased further after the detonation products commenced to burn in the detector cavity. The uncertainty in the arrival-time measurement at the first station indicates that the average velocity of the interface between the detonation products and the clean air shock was in the band of 4800 to 5100 ft/sec when it was propagating between the 25- and 99-ft stations. This reason for the aforementioned uncertainty should give a heavier weight to the lower velocity. These results--the measured shock velocity, the radar velocity output, and the infrared band of velocities--are shown in figure 16. It can be noticed that the lower limit of the infrared velocity band agrees quite well with that expected for an average of the radar velocity measurements during the same time frame.

Channel limitations made it necessary that the number of infrared experiments be limited to two on DABS IE. The previously mentioned electrical problems prompted a change in the conditioning circuit for these tests (fig. 17). The mechanical configuration was identical with the exception that a 1-in-diameter quartz window replaced the slot at the bottom of the pipe. The particular problem with this experiment was that the roof on DABS IE was sloped at 26 deg. That presented the options of either sloping the window with respect to the axis of the mount and accepting the lower transmission or allowing the pencil lead mounted detector to rest against the side of the pipe and accepting the increased vulnerability to shock loading. The latter option was chosen and the detectors failed shortly after shock arrival.

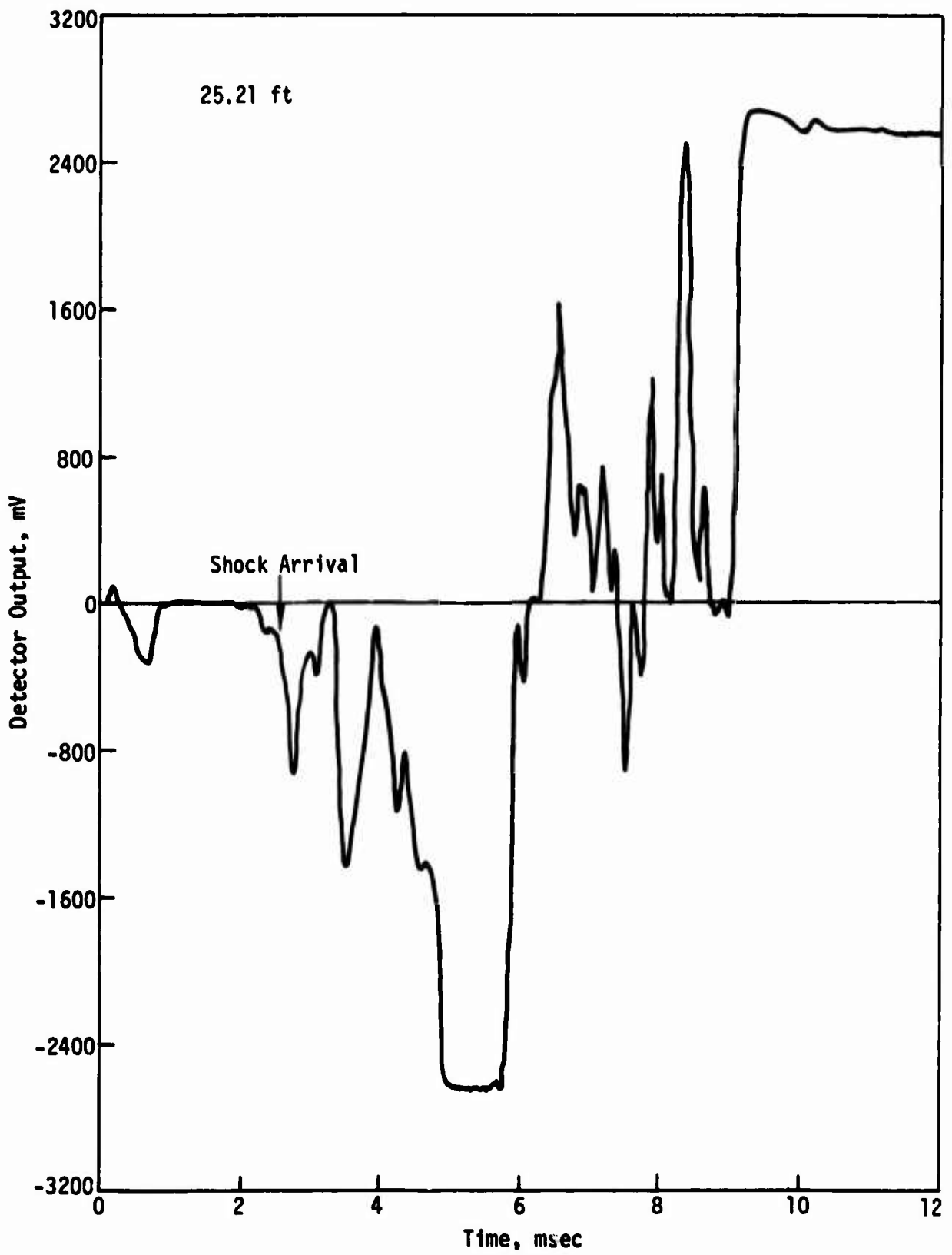


Figure 15. Response from Infrared Detector (1 of 2)

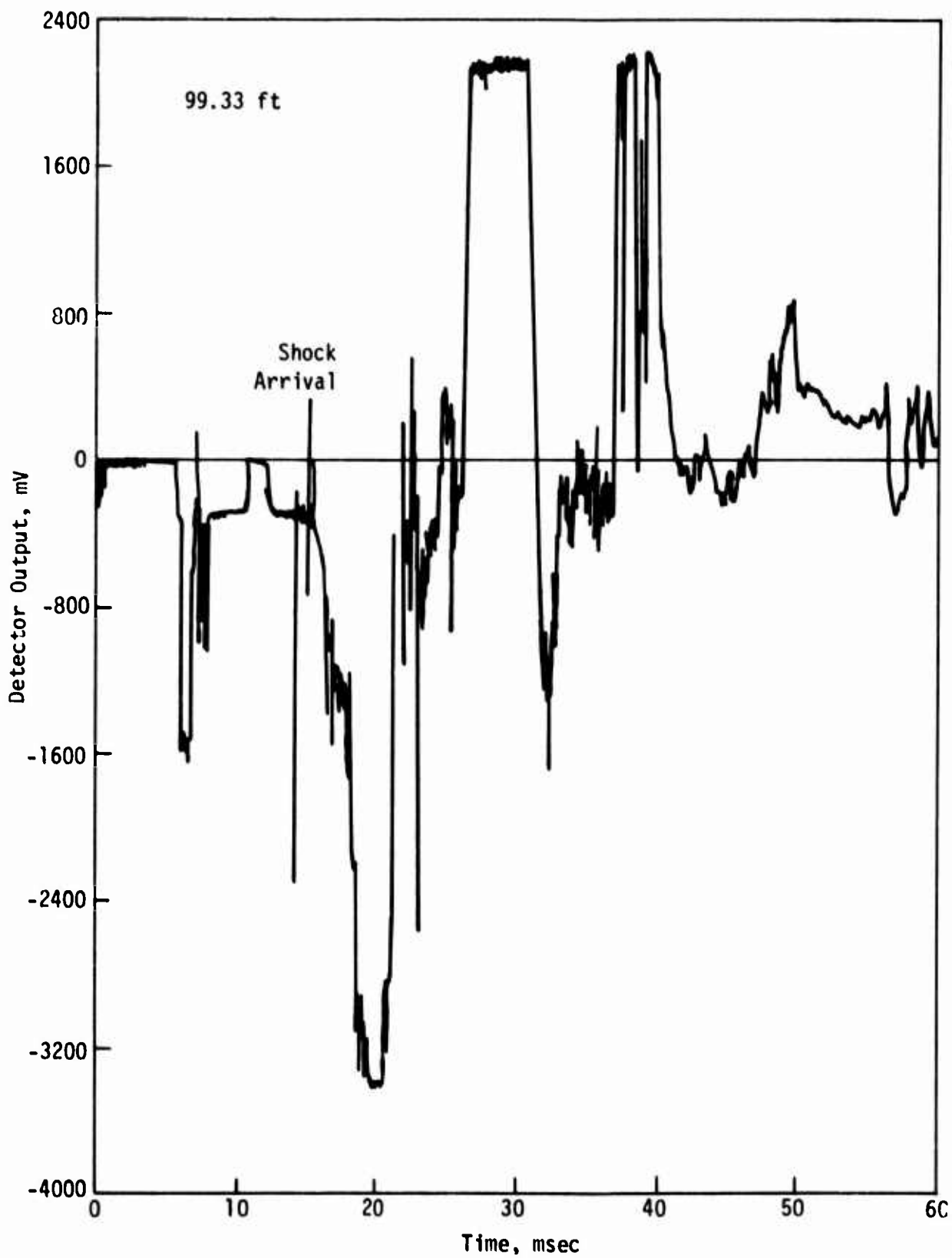


Figure 15. Response from Infrared Detector (2 of 2)

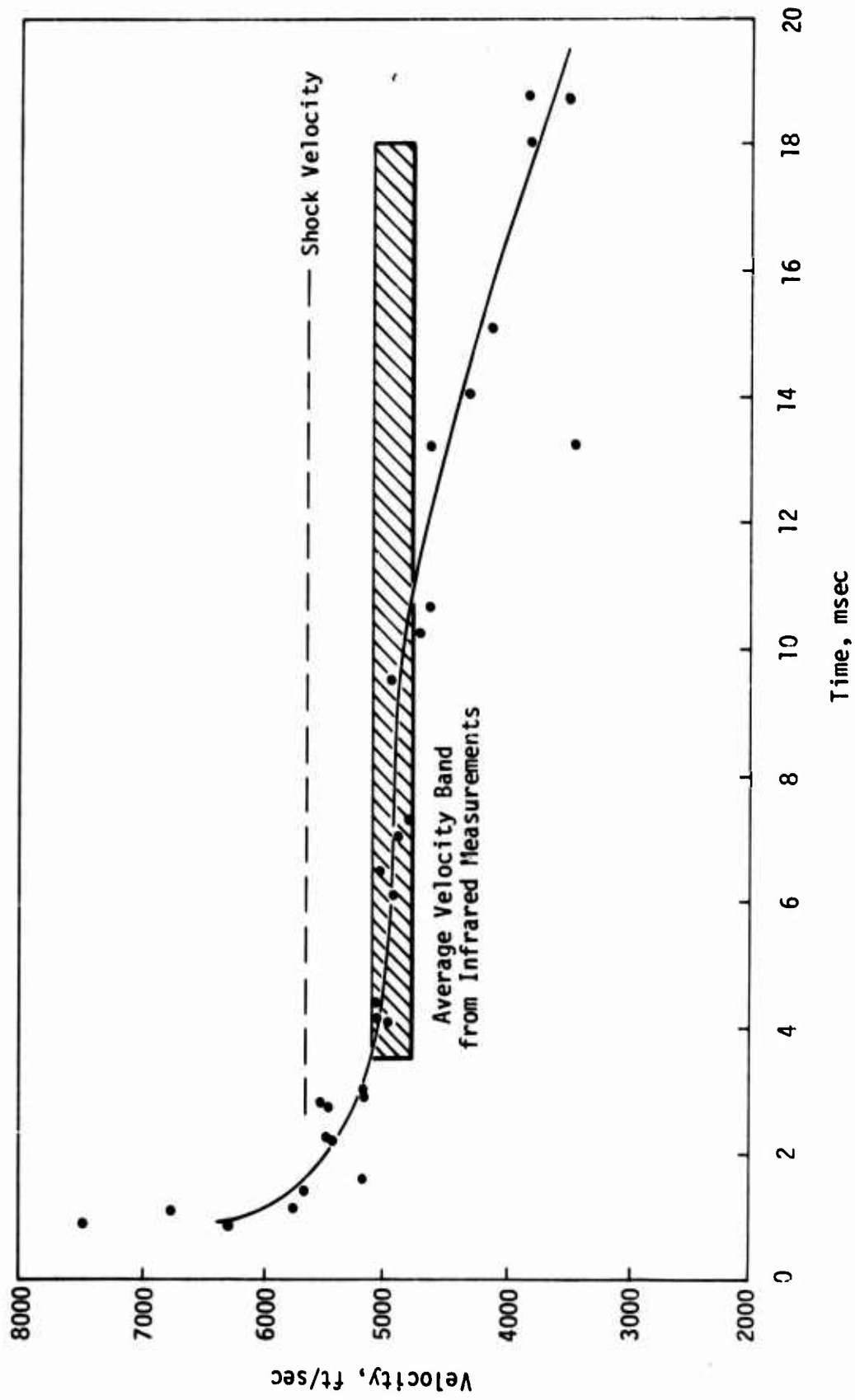


Figure 16. Comparison of Infrared and Radar Data

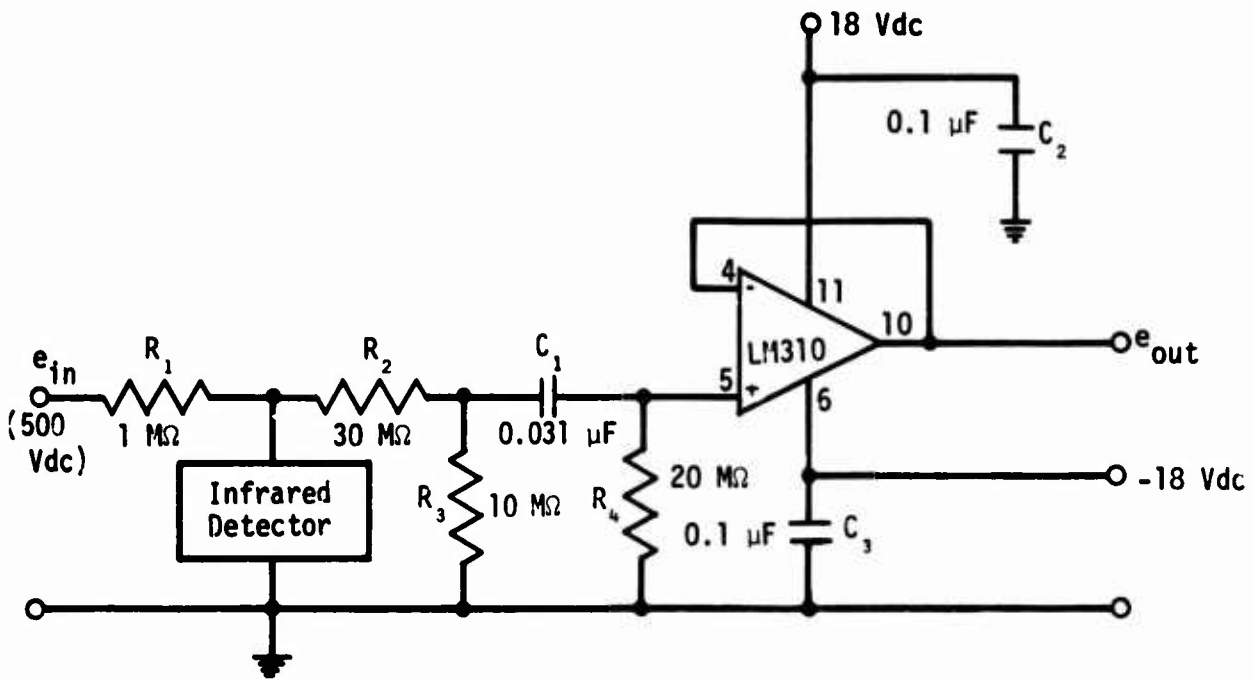


Figure 17. Infrared Detector Circuit for DABS IE

The infrared detector needs further check out before a multichannel temperature detector is made. The problems mentioned, however, are trivial enough that there is a good prospect for success with the detector package. There is some question as to whether or not the detonation products really behave as a black body. This can be answered only by using a temperature gage and determining whether or not the spectrum is equivalent to that of a black body. This will be tested in the follow-on effort (DABS Instrumentation Development-Phase II).

SECTION 4

OPTICAL PHOTODIODE

Performing optical experiments in DABS was quite intriguing. The possibility of determining temperature, particle velocity, and acoustic velocity certainly merited investigation. Specific interests were directed toward making temperature measurements by the Rotational Raman Scattering Technique. The proposed idea was to use a pulsed ruby laser system as a source and measure the frequency shifts in the rotational Raman lines as a direct inference of temperature. However, doing this was questionable because of the complete or nearly complete opacity behind the shock front. (See section 3.) Therefore, the purpose of this experiment was to determine if the atmosphere behind the shock front was really opaque to visible radiation.

A 650-W quartz iodide photographic lamp was placed on one side of the DABS ID tunnel behind a 2-in-thick glass window. The lamp, used in the spotlight mode, was aimed across the tunnel at a photodiode which was also placed behind a 2-in-thick glass window. Both items were shock mounted. The photodiode was an RCA Model C30822 N-Type Silicon Photodiode. The spectral response of this device is shown in figure 18. The response in the infrared range is extremely poor, and thus the signal from the photodiode was dependent only upon the visible light present. Since the cavity in which the lamp was placed was small, the lamp was turned on by a relay switch activated from the timing and firing van associated with DABS ID. The lamp was turned on 10 sec before detonation time. This prevented overheating and subsequent destruction of the lamp before the actual test. Power for the lamp was supplied by a 5-kW portable generator. Since the lamp, specifically the filament, was quite susceptible to shock damage, the current to the lamp was monitored.

The electrical circuit for the photodiode is shown in figure 19. The rise time of this circuit was tested in the laboratory with a strobe source and found to be less than 100 nsec; the published rise-time is 7 nsec. Since a fast enough light source was not available to verify this, the published value was assumed to be correct. The signal cable, an RG331, was terminated at 50 Ω . A Bell & Howell 3700 B Tape Recorder operated in the Wideband II FM mode (500-kHz response) was used to record the data.

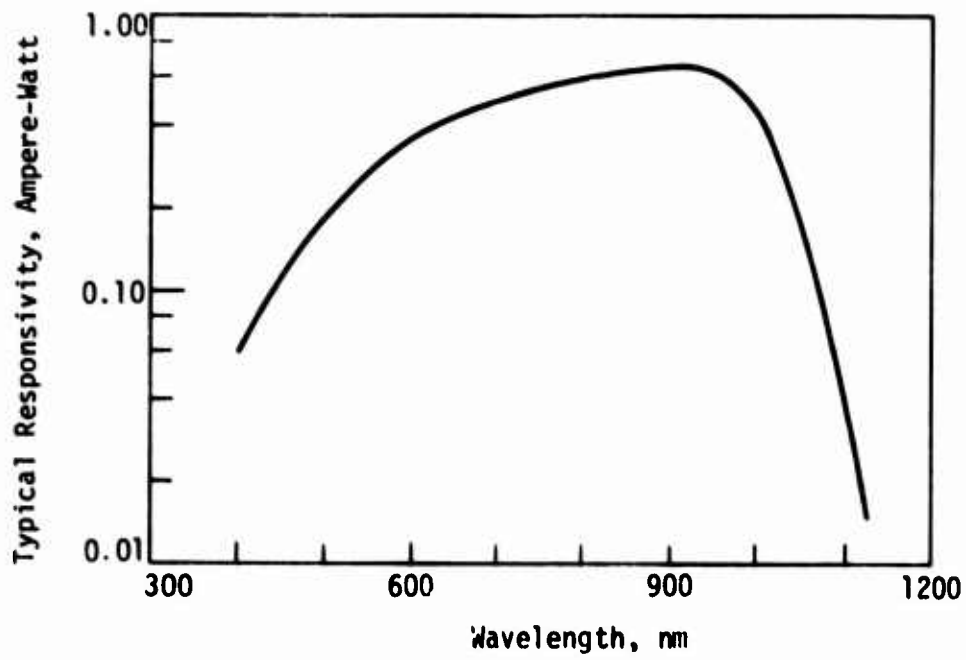


Figure 18. Spectral Response of Photodiode

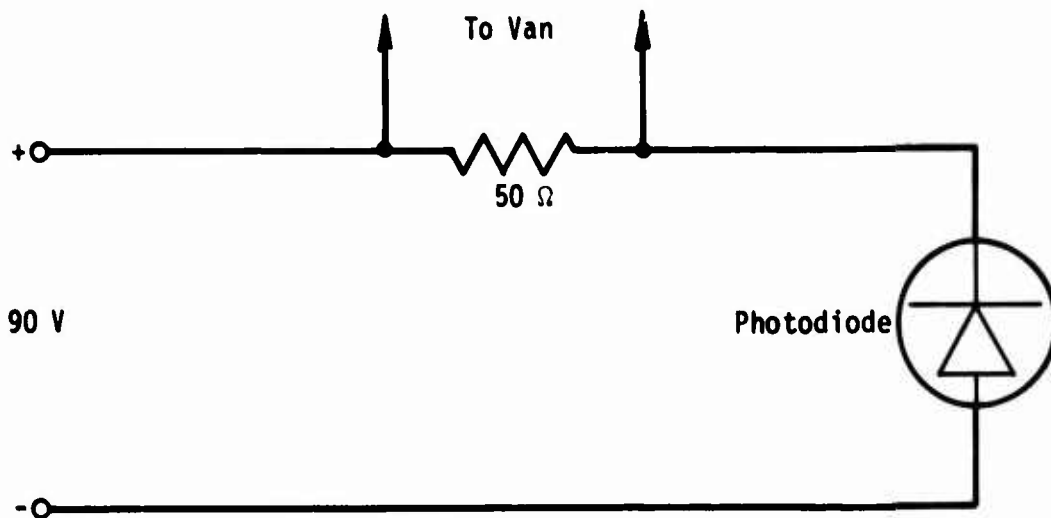


Figure 19. Photodiode Circuit

The light source for the potential rotational Raman scattering experiment was a pulsed ruby system that emitted a series of very short (20 nsec) high-powered light pulses. The argument can be made that if debris is the principal cause of optical absorption, there exists a higher probability of apparent transmission of a short pulse with a high-frequency response recording system than there is of propagating a continuous beam with a comparatively low-frequency response system. There are two reasons for this. First, much higher light intensities can be obtained with pulsed systems than with continuous wave systems. Second, the short-length pulse propagating at the speed of light has a much lower probability of interacting with the discrete scattering centers (debris) than does the continuous wave. For these reasons along with the desire to determine if a continuous wave could propagate, a high-frequency recording system was used in addition to the tape recorder. This was the particular reason for using the RG351 cable (foamflex). In addition a Tektronix 555 delay triggered oscilloscope swept at 100 nsec/cm was used to record the data.

The data obtained from this experiment are shown in figures 20 and 21. The current monitor output (fig. 20) indicates that the lamp ceased to function 12.2 msec after detonation. The arrival-time data for DABS ID indicate that the shock front arrived at the lamp and photodiode locations 7.4 msec after detonation or the lamp failed 4.8 msec after shock arrival. Figure 21 shows that the optical photodiode continued to function even after the lamp failed. Thus there was some source of light other than the lamp. In fact almost immediately after detonation, a pulse was observed, after which the light intensity increased until it reached tape recorder bandedge (twice the intensity provided by the lamp). The light signal remained at bandedge until 12.6 msec after detonation and then proceeded to zero or near zero intensity in a period of 3 to 4 msec. At later times the light intensity increased again. This could have been due to venting into the cavity which encapsulated the photodiode. During the period of time that the signal was bandedged, the oscilloscope was triggered and as expected the trace was off screen.

A reasonable hypothesis as to what occurred is that right after detonation, a bright flash illuminated the tunnel. (This is the spike on the photodiode trace.) After the burning interface between the explosive products

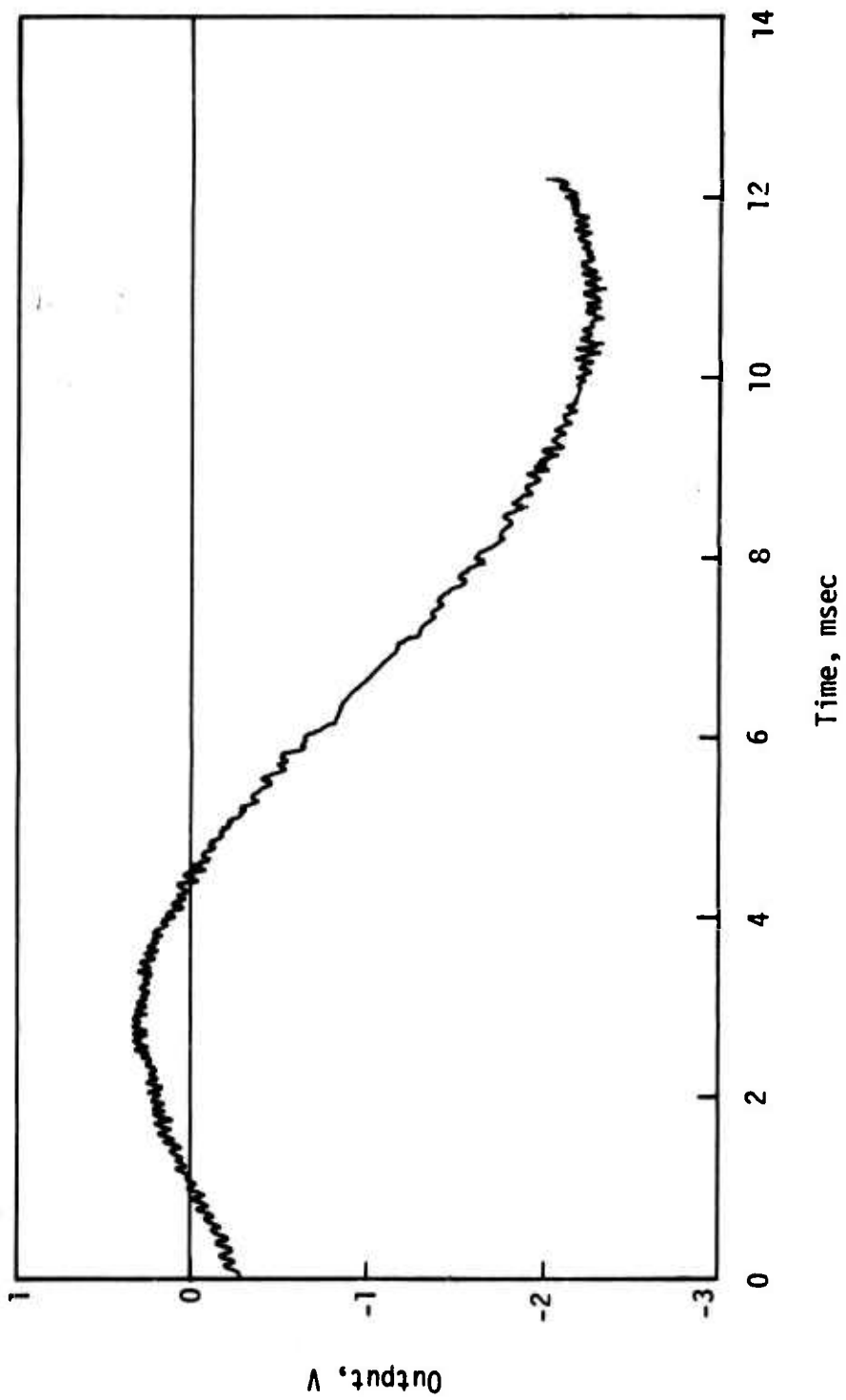
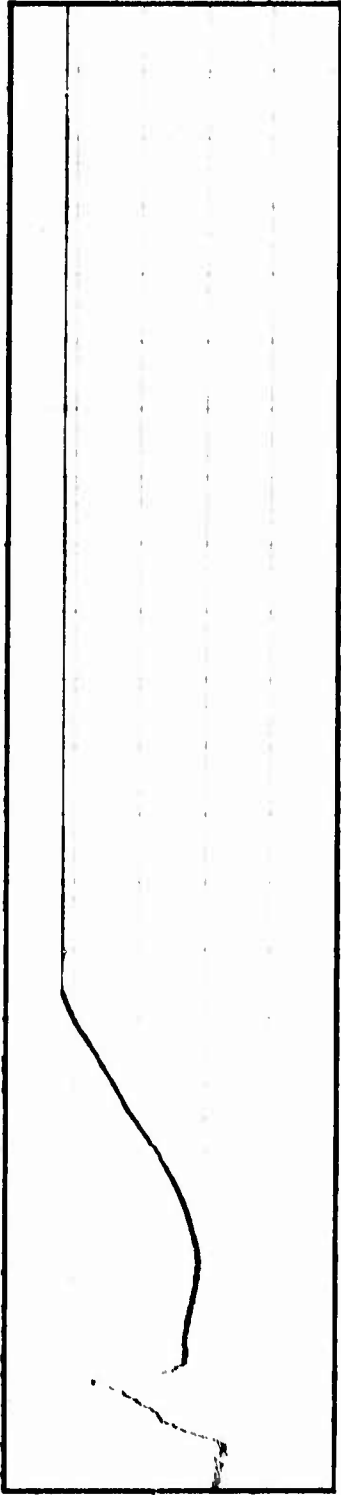
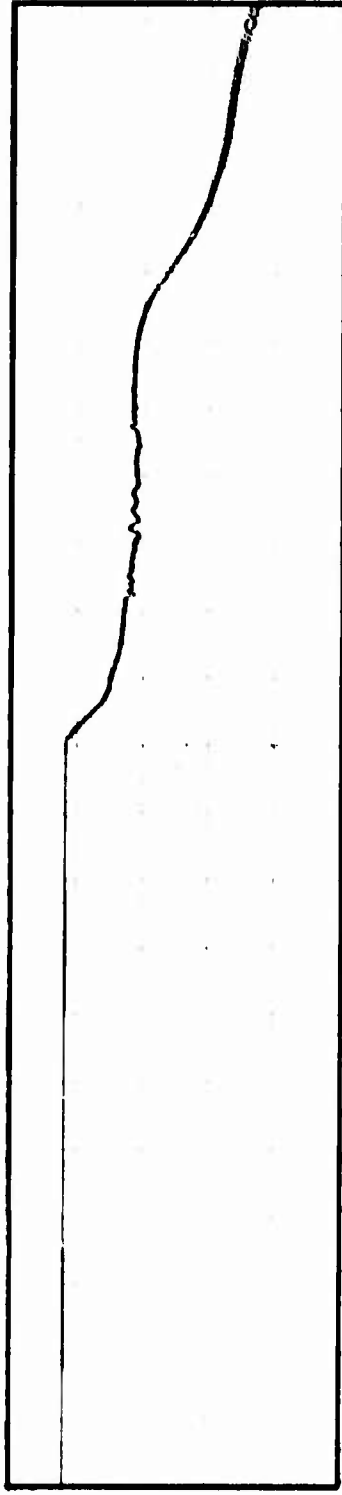


Figure 20. Current Monitor Output



Arbitrary Voltage



0.4 msec/div

Figure 21. Photodiode Output from DABS ID

and the clean air shock passed the detector, the signal magnitude decreased to a level below bandedge. This was within 3 msec after the burning interface passed the photodiode. As this interface proceeded to propagate down the tunnel, the light intensity (incident upon the photodiode) due to this burning interface decreased rapidly. Thus, since the intensity decreased over a period of 3 to 7 msec, the detonation products did transmit light. However, the late-time transmission of this light was somewhat minimal.

The results of this experiment are somewhat conflicting with those of the photographic experiment on DABS IA. The DABS IA results indicated opacity; the DABS ID photodiode indicated transmission. This discrepancy and cost considerations lead to the conclusion that the Rotational Raman experiment would not be attempted at this time.

SECTION 5
DEBRIS COLLECTOR

The stagnation pressure data generated in DABS show an anomalous second peak. One of the postulated reasons for this peak is that pressure gages were affected by debris impact. For this reason a debris collector was fielded on DABS ID. It consisted of a simple pipe mounted on top of the second post. The inside diameter of this pipe was 1.5 in and the total mass of debris collected in the pipe was 36.78 g. This yielded an areal density of 0.0458 lb/in². This debris was subjected to a sieve analysis and the results are shown in table 1. The prime fault with the experiment was that there was no way to separate the debris collected from the flow from that collected as a result of fallback.

If some assumptions about the average velocity at which the debris was moving are made, the impulse can be determined from the assumption that the momentum of the particles impacting the stagnation-pressure gages is converted to an effective pressure reading at the gages. Thus if \bar{V} is the average velocity and m is the areal density of the debris mass, the specific debris impulse, I_D , is $m\bar{V}$.

Table 1. DABS ID Debris Distribution

Sieve No.	Particle Size, in	Mass, g
> 20	0.0331	9.2
40	0.0165	9.3
60	0.0098	7.0
140	0.0041	5.8
200	0.0029	2.0
< 200	0.0029	3.5

The next assumption made was that the bulk of the debris was picked up right after the detonation, where the turbulence is great. Thus, it can be expected that the bulk of the debris was generated in the area close to the detonation chamber. If this was the case, the debris was mostly located near and behind the detonation-products interface. The presumption was that the radar unit tracked the interface itself or the debris near it (fig. 16). The infrared data show the range of average velocities for the interface during the time period noted on the graph. The agreement is fairly good and at the times of interest the peak velocity of the interface varied from 5100 to 3600 ft/sec. Since the particle velocity falls off rapidly behind the interface, the average velocity of the debris in this region is certainly lower than the peak velocity. Thus, if the presumption that the bulk of the debris is near to or behind the interface is correct, average debris velocities in the range of 2000 to 4000 ft/sec could be expected.

The next question to answer is, "How much of the debris came from the fallback as opposed to the shock?" It is believed that the large particles (greater than 0.0331 in diameter) came from the fallback or came so late and so slow that they did not appreciably add to the impulses. This presumption leads to an areal density of 0.0344 lb/in².

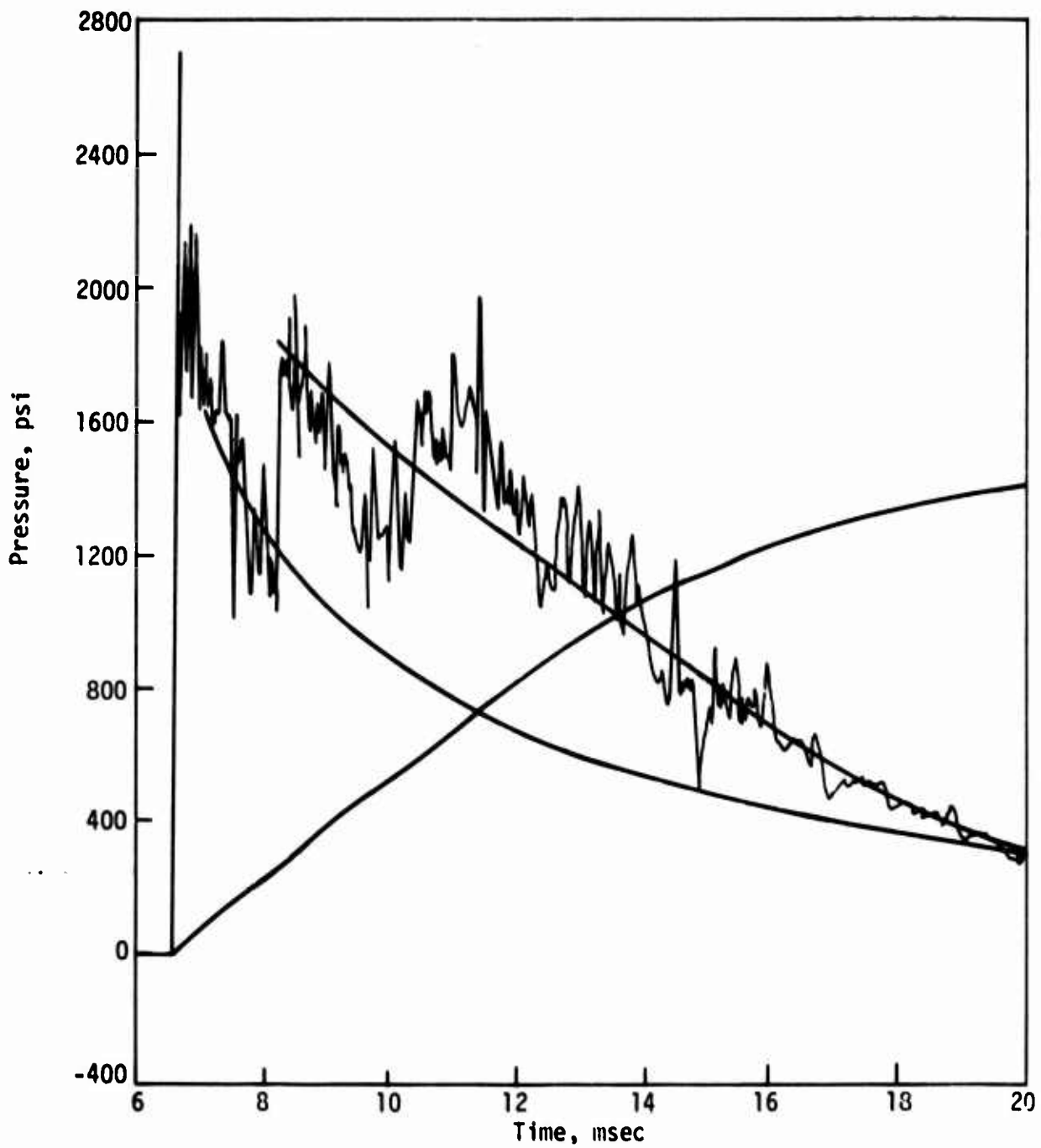
The last assumption made was that the second peak on the stagnation-pressure measurements was totally due to the debris in the flow. If this was the case, an average velocity for the debris can be calculated from the impulse due to the second peak. This was accomplished by simply smoothing the entire curve and taking the area under the second peak (fig. 22). In both these cases the specific impulse was approximately 3.25 psi-sec. Thus

$$m\bar{V} = \frac{0.0344}{32} \bar{V} = 3.25$$

or

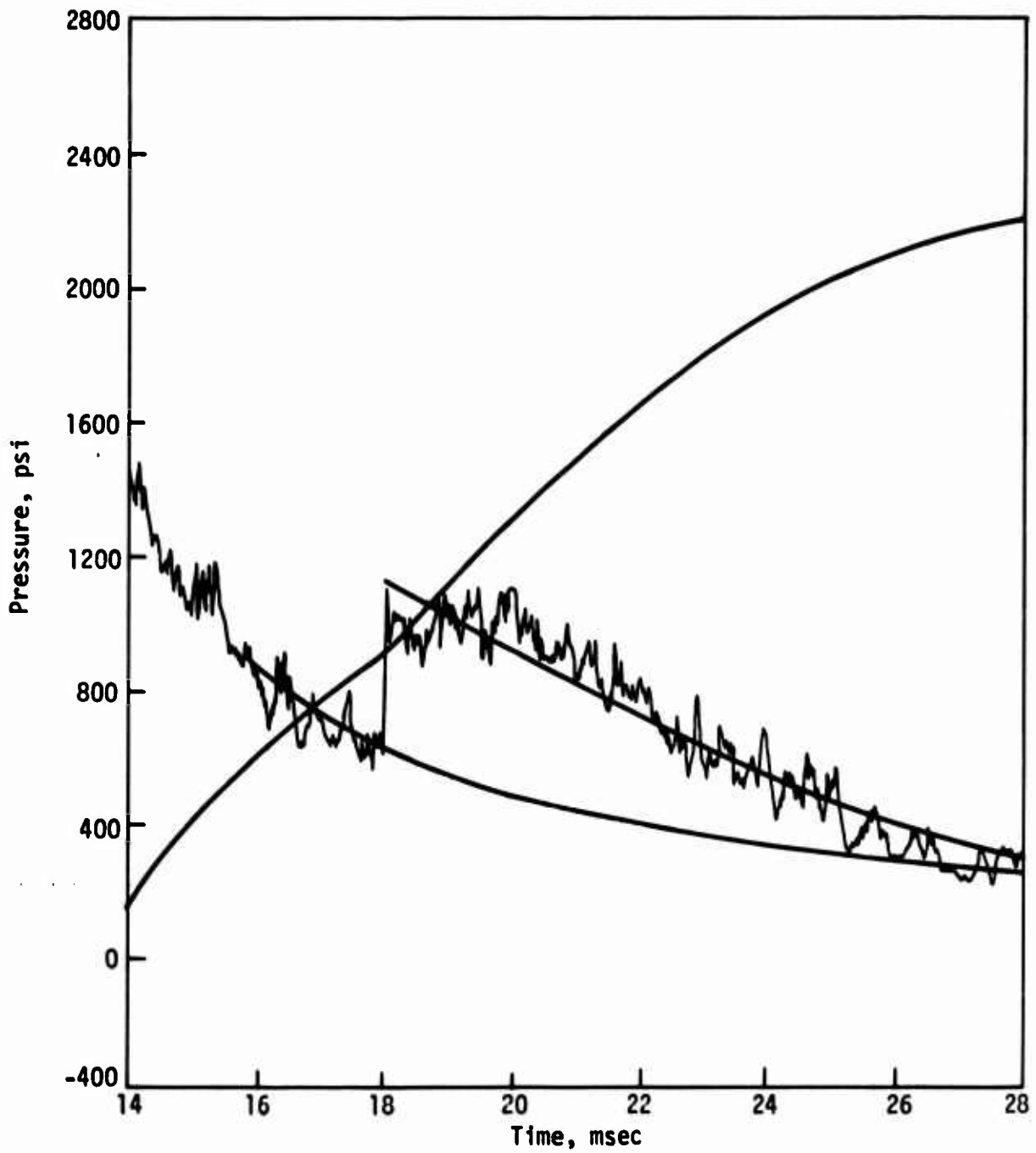
$$\bar{V} \approx 3000 \text{ ft/sec}$$

This is a reasonable value. Thus, as much as one is able to generalize with one datum point, the second peak can be plausibly explained with a debris-impacting model. Obviously, however, the second pulse on the stagnation measurements was not totally due to debris; it is more likely that it was due to a combination of the higher density detonation products and the debris.



$$\begin{aligned}
 I_{\text{Second Peak}} &\approx \frac{1}{2}(650 \text{ psi})(10 \times 10^{-3} \text{ sec}) \\
 &= 3.25 \text{ psi-sec}
 \end{aligned}$$

Figure 22. Second Peak in DABS ID (1 of 2)



$$\begin{aligned}
 I_{\text{Second Peak}} &\sim 1/2(525 \text{ psi})(12 \times 10^{-3} \text{ sec}) \\
 &= 3.15 \text{ psi-sec}
 \end{aligned}$$

Figure 22. Second Peak in DABS ID (2 of 2)

The prime difficulty with the experiment was the inability to correct for the fallback. Thus, the next obvious step in the development was to separate the debris in the flow from the fallback debris. Figure 23 shows the mechanism used on DABS IE. This device consisted of a pipe (the same type as that used on DABS ID) mounted on a wing with a closing mechanism designed such that the debris in the rear of the pipe would be separated from the fallback debris in the front of the collector. The closing mechanism was a spring-driven door. The spring provided a force of approximately 20 lb on the door. The triggering mechanism was simply a plate with a tongue that was inserted into a slot in the door when the device was in the cocked mode. Cocking was accomplished by inserting a screw through a threaded hole in the top of the pipe. When the shock wave reaches the device, the flow is stagnated by the trigger plate and the resultant force on the plate (between 15,000 and 22,000 lb) simply blows the trigger plate downstream; this releases the door and allows it to close.

The triggering mechanism, however, caused some concern because of the differential pressures created along the door. These differential pressures resulted from the hole in the side of the wing for the trigger plate. It caused the pressure there to be approximately the side-on pressure (nominally 600 to 700 psi), while the pressure inside the pipe was the stagnation pressure (nominally a few thousand pounds per square inch). Thus there was the strong possibility that the debris contained in the flow passing the door could jam the door. For this reason, other concepts were considered. These included electrical-shutting, explosive-shutting, and pencil-lead triggering techniques. However, all these were rejected because of their complexity or poor reliability. With this expressed reservation, it was felt that the chosen option was the simplest, least expensive, and most reliable system.

An important factor considered in the design was the time it would take for the door to close. The door would not start to close until after the shock front reached the device and the differential loading on the door, resulting from the flow mechanism, became less than 20 lb. Thus, the door would close the fastest with no differential loading on it. This time was measured through high-speed photography; the results are shown in figure 24. These data show that the debris collector was halfway closed 16 msec after the shock arrival; for the DABS waveforms, this was deemed adequate.

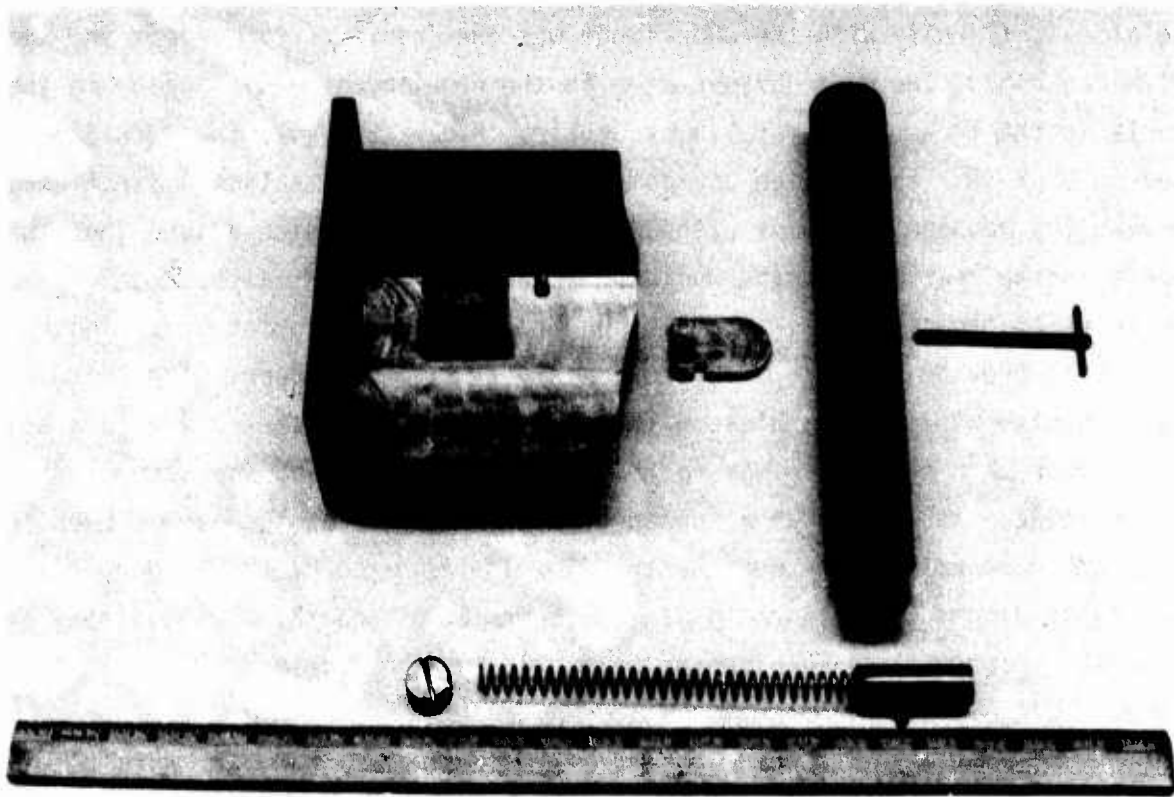


Figure 23. Debris Collector

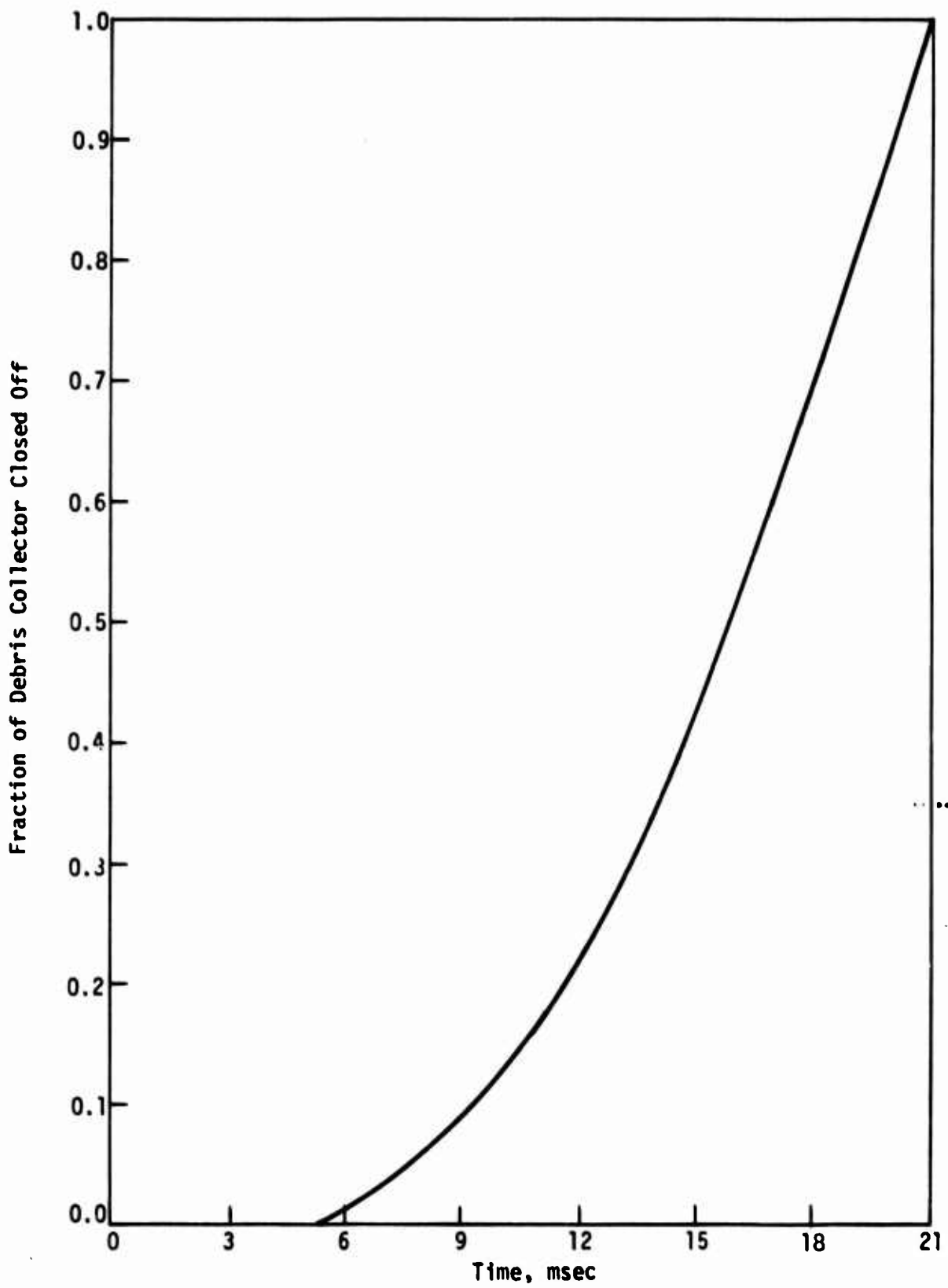


Figure 24. Time of Closure of Mechanism for Debris Collector

The system on DABS IE did not work as planned. The door closed only halfway; it was jammed by a small amount of debris. There was no noticeable debris in the spring cavity below the door. However, this problem was not serious since the overburden fallback was minimal; on DABS ID the fallback literally covered the debris collector. The design of DABS IE with its sloped roof minimized this problem. The bulk of the overburden fell back outside the tunnel. The collector was examined immediately after the test and no noticeable debris was found in the front of the collector; all of the debris was behind the half-closed door. The total debris collected was 15.66 g. The sieve analysis is shown in table 2.

An areal density of 0.0195 lb/in² can be inferred from the total weight of the debris. Figure 25 shows the output from one of the stagnation gages. This gage was located approximately the same linear distance (75 ft) from the driver end as the debris collector. The apparent impulse due to the second peak was approximately 3 psi-sec. If it is presumed that this was entirely due to debris,

$$m\bar{V} = \frac{0.0195}{32} \bar{V} = 3$$

or

$$\bar{V} = 4923 \text{ ft/sec}$$

Table 2. DABS IE Debris Distribution

Sieve No.	Particle Size, in	Mass, g
> 20	0.0331	4.99
40	0.0165	3.59
60	0.0098	2.36
140	0.0041	1.91
200	0.0029	0.73
< 200	0.0029	1.78

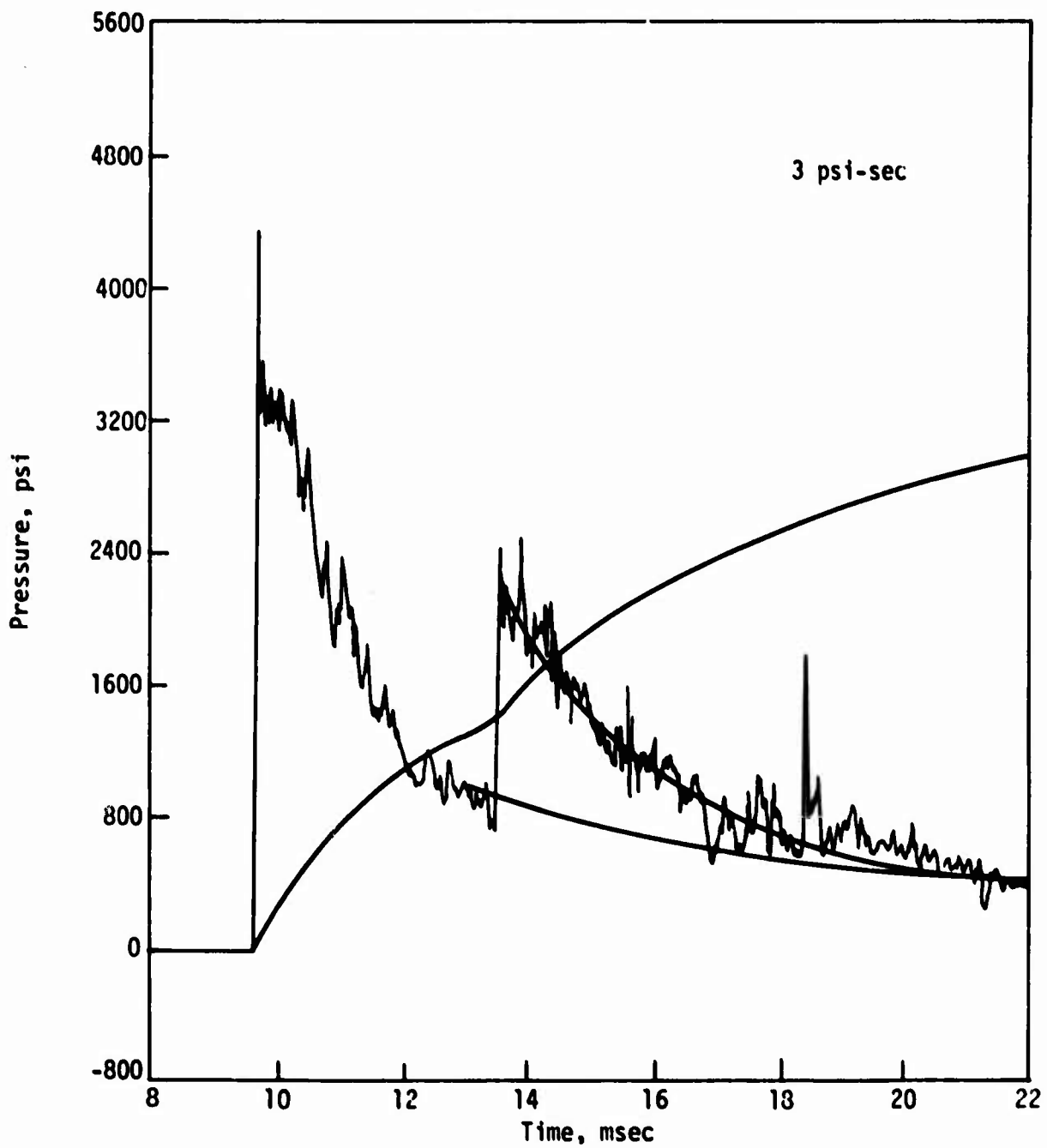


Figure 25. Stagnation Pulse from DABS IE

At the time the second pulse occurred (13.5 msec after detonation), the velocity of the interface between the detonation products and the clean air shock was 5500 ft/sec (fig. 9). Thus the average debris velocity of 4923 ft/sec is probably high and it may be concluded that the second pulse is not entirely due to debris impact but a significant portion of the impulse in this case is most likely due to debris.

Visual inspection of the debris showed that it consisted of carbon, concrete, sand, and wood. The bulk of the carbon probably came from the decomposition of the plastic jacket surrounding the detonating cord.

It seems that the basic concept of a debris collector is quite valid to support the analysis of the data from DABS. However, the design needs some improvement or possibly some radical change. An obvious improvement would be to modify the door-closing technique used to separate the debris from overburden fall-back. In addition, the stagnation of the flow in a plugged pipe indicates that there is a possible back flux of debris out of the collector as the outside pressure decreases. Admittedly, this effect should be small since all the debris goes to the end of the collector and is deposited on the plug. However, since there is the possibility of putting the collector tube into resonance during unloading and sweeping out the debris is finite, some modification may be desired. Additionally, the present debris collector gives no information regarding the time history of the debris flow. Debris collectors to do this have been designed but little success has been attained. Primarily they operate with the timed detonation of shaped charges around both ends of a tube. It is apparent that these designs can be improved and this should be undertaken. Another device that may be of use because of the high cross section that debris has to beta particles is the beta densitometer.

SECTION 6
SHOCK-ON-SHOCK INSTRUMENTATION

One of the flow variables of primary importance in DABS is the mach number in the flow. Mach number is defined as *the ratio of flow or particle velocity to local acoustic velocity*. The stagnation pressure is inferred from pitot tube type measurements from DABS. The supersonic pitot type measurement technique is diagrammed in figure 26. With the notation that M_x is the local mach number in the flow, p_x the static pressure in the flow, p_o the stagnation pressure, p_y the static pressure in the stagnated region, and p_{oy} the pitot tube pressure,

$$\frac{p_{oy}}{p_x} = \left(\frac{\gamma + 1}{2} M_x^2 \right)^{\frac{\gamma}{\gamma - 1}} / \left(\frac{2\gamma}{\gamma + 1} M_x^2 - \frac{\gamma - 1}{\gamma + 1} \right)^{\frac{1}{\gamma - 1}}$$

and

$$\frac{p_o}{p_x} = \left(1 + \frac{\gamma - 1}{2} M_x^2 \right)^{\frac{\gamma}{\gamma - 1}} \quad (\text{ref. 2})$$

The relationship between these measured quantities is greatly dependent upon a knowledge of the local mach number. Thus, the experimental determination of local mach number is of primary importance in understanding the flow conditions... in DABS. Normally, a shock-diffraction experiment is performed and from a measurement of mach angle, the mach number is inferred. Unfortunately DABS is the worst of all possible worlds to do this type of experiment in, since the major part of the flow is transonic. Therefore, an experiment suggested by R. Shunk of Electromechanical Systems and B. Sturtevant of the California Institute of Technology was implemented. The theoretical analysis of this experiment is contained in appendix C.

The experimental layout is shown in figure 27. A 2-lb charge of C4 explosive was mounted in the wall of DABS IE. Three fast-response (PCB quartz) gages were placed downstream and above the explosive charge. Piezoelectric pins were placed further downstream (≈ 15 ft past the gages). These pins were used to trigger the detonation system for the explosive charge. Thus, at the time

2. Shapiro, A., *The Dynamics and Thermodynamics of Compressible Fluid Flow*, Vol. I, The Ronald Press Company, N.Y., N. Y., 1953.

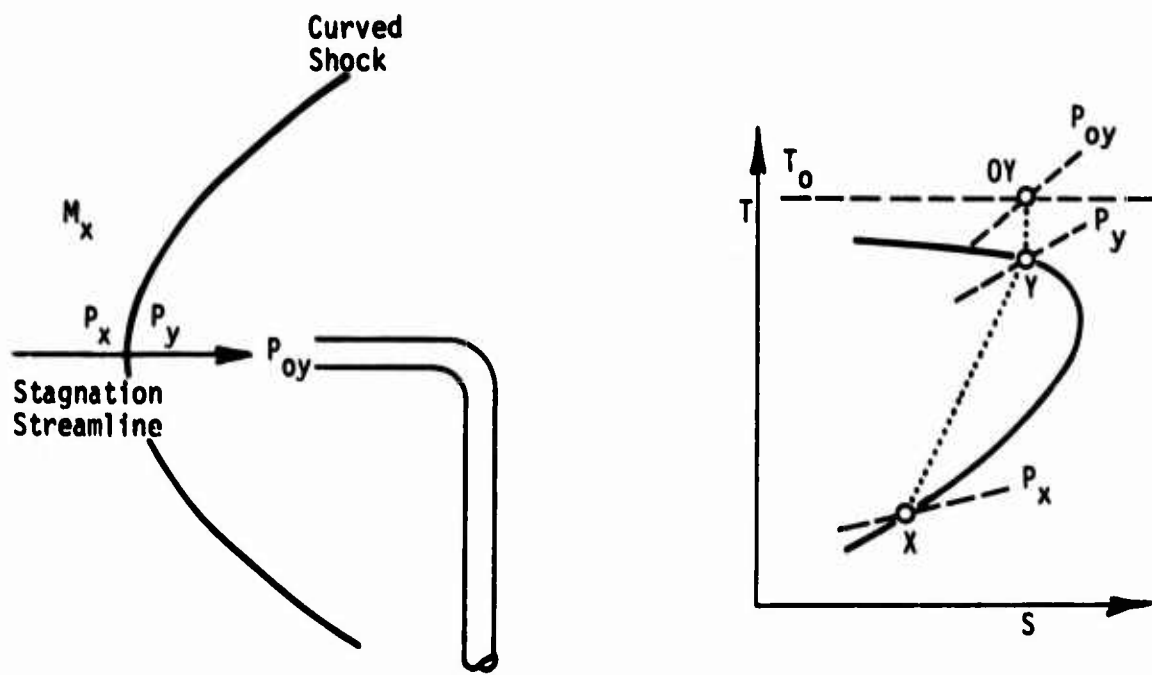


Figure 26. Supersonic Pitot Tube [after Shapiro (ref. 2)]

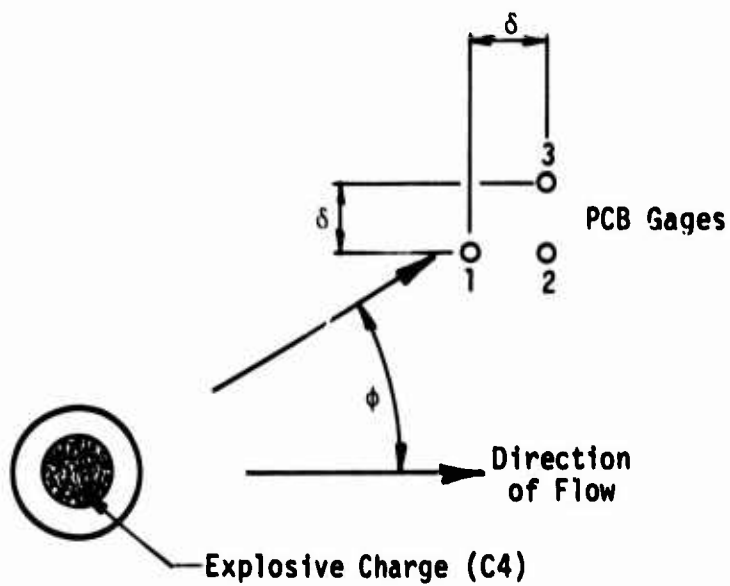


Figure 27. Layout for Shock-on-Shock Experiment

of detonation of the small charge, the shock wave produced would be added to the shock wave in DABS (shock on shock). As the secondary shock wave propagates in the flow it will pass over the three pressure transducers. Since these transducers were close together (4 in apart) and far from the source (4 ft), the secondary shock would propagate across these transducers with a constant direction with respect to the DABS flow. The angle between this secondary shock propagation and the DABS is defined as θ . (See appendix C.) If ϕ is the angle between a line connecting the explosive charge and the gages and flow direction and if δ is the distance between the gages (as shown in appendix D),

$$\tan\theta = \frac{\Delta t_2}{\Delta t_1}$$

$$c = \frac{\delta}{\Delta t_2} \sin\theta \left[1 - \frac{\tan(\theta - \phi)}{\tan\theta} \right]$$

$$u = \frac{\delta}{\Delta t_2} \tan(\theta - \phi)$$

where c is the secondary shock velocity, u is the DABS flow velocity, Δt_1 is the time between secondary shock arrivals at gages 1 and 2, and Δt_2 is the time between secondary shock arrivals at gages 2 and 3 (fig. 27). If the mach number of this secondary shock were known, the experiment would simultaneously determine both the particle velocity and the acoustic velocity in the flow, and since the mach number is the ratio of these two quantities, it too could be determined.

The particular disadvantages of this type of measurement are as follows:

- (1) only the mach number at one given time back in the flow is determined,
- (2) the pressure pulses are so noisy that discriminating the secondary shock from the primary shock or other noise is difficult, and
- (3) geometry and time dictate that the explosive charge be put in a steel canister mounted in the same wall as the gages. (This mounting tends to direct the blast from the small charge away from the wall and thus limits the secondary shock impingement upon the gage.)

The experiment was a qualitative, but not a quantitative, success. Figure 28 shows the data trace obtained from gage 1. The magnitude of the secondary shock is quite small. Although this shock was present on the other traces, the one on this trace was the most clearly defined. This low level, combined with the noise, precluded the possibility of making the time-of-arrival measurement within the required precision. It is expected that this problem can be overcome by directing the shock toward the gages instead of away from them. This can be accomplished by placing the charge in the floor upstream from the gages. In this manner the secondary shock would propagate more in the direction of the gages. The importance of this type of measurement mandates the further development of this technique and appropriate instrumentation should be fielded on future DABS events.

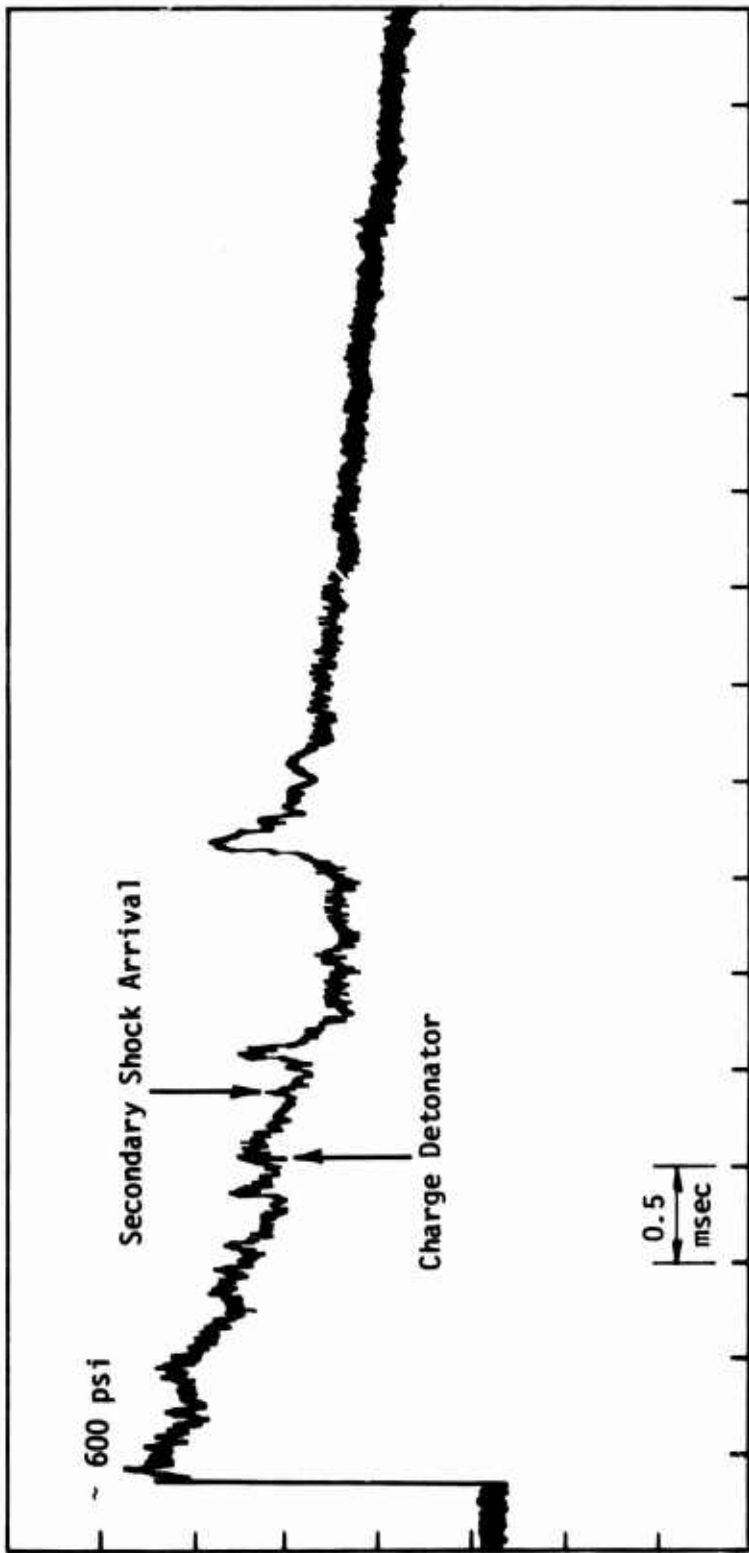


Figure 28. Shock-on-Shock Experimental Data (Gage 1 Output)

SECTION 7 PRESSURE AND VELOCITY GAGES

STAGNATION PRESSURE GAGE

Primary development of the bar gage has already been reported in reference 3. The only modification to this gage was the addition of a 0.2-in-thick shield of RTV silastic filled with coarse lead-powder granules. Although this addition caused some ringing and slapping effects in the reflected pressure mode, no effects were noted in the dynamic flow encountered in DABS. Apparently this shield decreased the posttest dc-offset of the gage. This offset was probably due to debris impact which caused permanent deformation on the front surface of the gage. Obviously the shield absorbed most of the momentum of the debris particles and thus lessened the effect.

DRIVER-CHAMBER PRESSURE GAGES

An attempt was made on DABS IA to measure the equilibrium driver pressure. This pressure is defined as the initial driving pressure due to detonation of the detonating cord distributed in a known volume. On DABS IA a bar gage was mounted surface flush in the floor in the center of the driver chamber. No protection was used on the front surface and the gage failed before any pressure could be determined from its output. Another attempt was made on DABS IE.

The expected pressure can be calculated by

$$P = (\gamma - 1) \frac{E}{V}$$

where P is the driver pressure, E/V is the specific explosive energy density in the driver chamber, and γ is the ratio of isobaric to isovolumetric specific

3. Simmons, Kenneth B., *Development of Piezoresistive Bar Gage*, AFWL-TR-76-65, Air Force Weapons Laboratory, Kirtland Air Force Base, New Mexico, December 1976.

heats. With a γ of 1.2, a charge density of 6.4 lb/ft³, and an explosive energy of 2×10^6 ft-lb/lb, the resultant pressure is approximately 18,000 psi. Since the gages were located near the detonating-cord array, peak pressure could be much higher than this because the peak pressure of the shock wave emanating from the explosive is higher than the equilibrium gas pressure in the vicinity of the explosive. Since these detonation wave pressures can be many times greater than the desired measurement, the gages must either be able to measure them and survive or a mounting scheme must be devised to ensure that their effect will be limited. Two different schemes were fielded on DABS IE-- a 30,000-psi Kulite gage with a MOD V debris shield, and a ported bar gage.

The description of the MOD V debris shield experiment as given by J. Quintana of AFWL/DED-I is as follows:

The debris-shielded Kulite gage sensing scheme is shown in figure 29. The sensing installation to measure driver chamber pressure is shown in figure 30. The installation consisted of the regular AFWL-developed hardware cast into the concrete side wall of the driver chamber. In the preshot configuration the Primacord bundle was approximately 8 cm from the module sensing surface.

The ported mount for the bar gage is shown in figure 31. The nylon insert was used as a shock isolator for the gage. The port geometry was modeled after the design of a B filter. The response of the porting scheme is described in reference 4. The 10-to-90 rise time of the B filter was 55 μ sec. In this case the rise time will be slightly longer because of the slightly larger cavity below the entrance port (0.36 in diameter as opposed to 0.306 in diameter). This difference was necessitated since the original design was for a Kulite gage with a smaller active gage area. This ported mount was designed to act as a low-pass acoustic filter and thus protect the gage from the high-pressure spikes caused by the detonation waves emanating from the individual explosive charges. Since the rise-time requirement for the measurement was in the range of 100 to 500 μ sec, the design was judged adequate. Additional protection for the gage was afforded by using a lead particle load RTV compound over the front surface of the gage. This 0.2-in-thick shield protected the gage from debris impinging on the gage through the 0.125-in-diameter port.

4. Baum, Neal, *Shock Tube Gage Evaluation Quick-Look Data Report*, CERF Letter Report FI-3, Eric H. Wang Civil Engineering Research Facility, University of New Mexico, Albuquerque, New Mexico, August 1975.

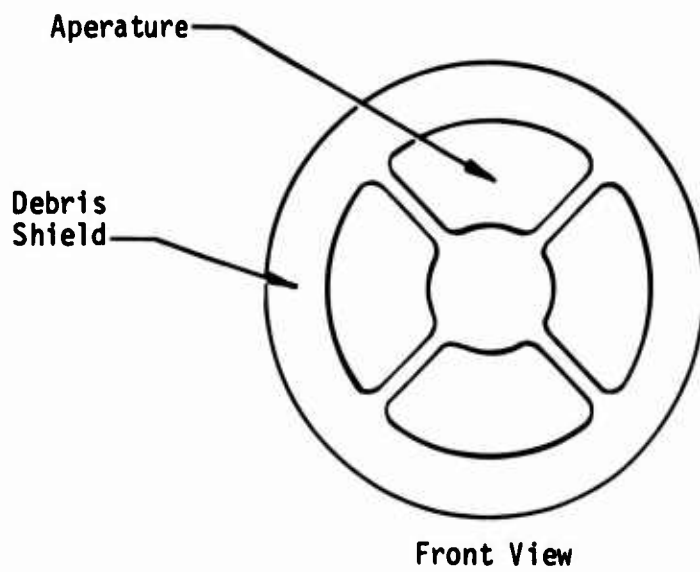
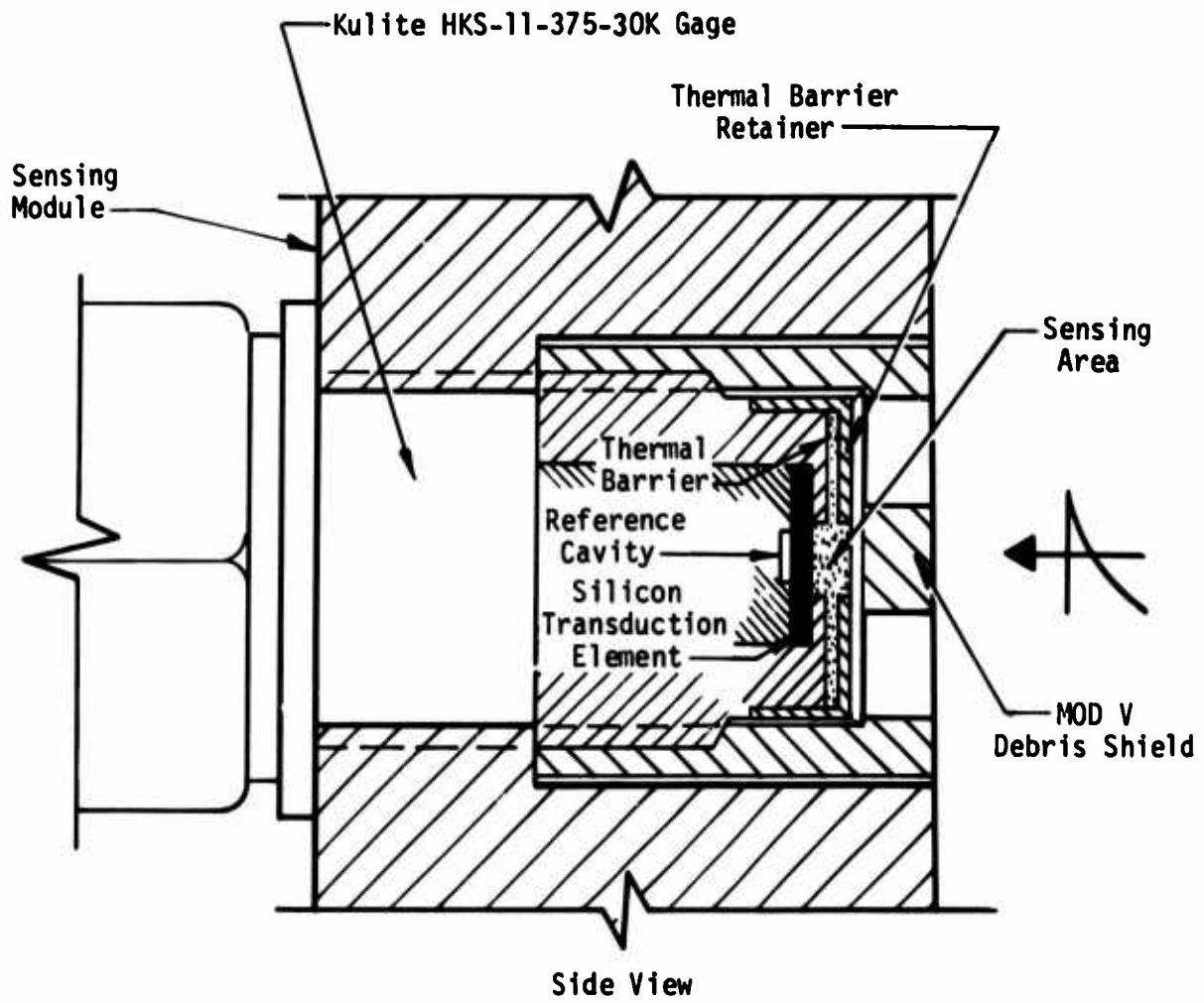


Figure 29. Debris-Shielded Kulite Gage Sensing Scheme



Detonating
Cord Bundle

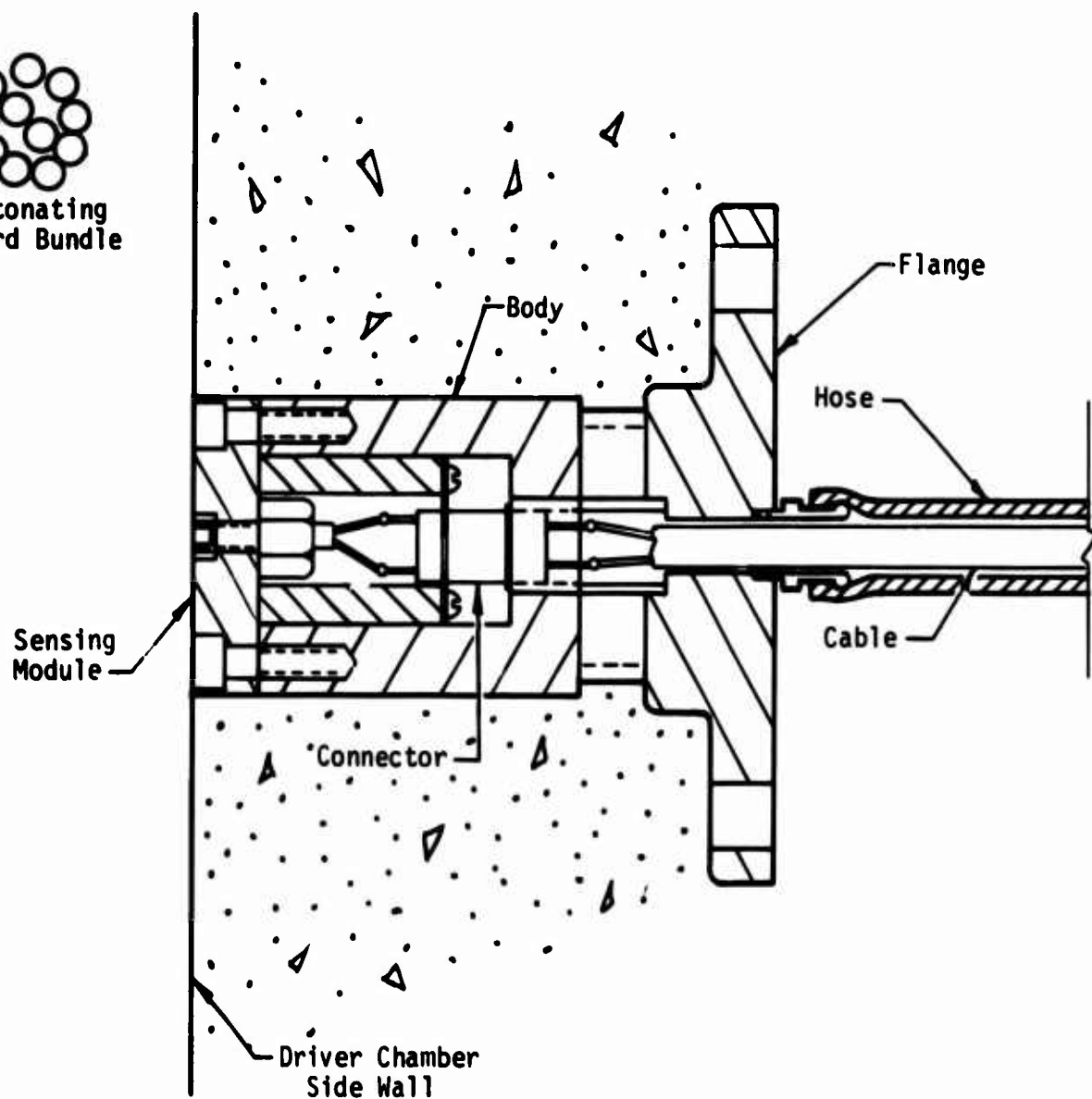


Figure 30. Sensing Installation

One of the questionable points concerned with the gage was the weakness of the nylon grommet isolator. However, the gage has a finite mass (≈ 50 g) and the time required to make a meaningful measurement is relatively short (100 to 500 μ sec). Thus with an 18,000-psi pressure applied to its surface and the strength of the nylon threads neglected, the gage will move only 0.03 to 0.75 in and the space behind the gage is adequate for this.

The result of this experiment is shown in figure 32. There was an obvious catastrophic failure, which was probably due to cable failure since the gage was still functioning after removal from DABS IE. The atmosphere was obviously quite harsh (fig. 33). The front surface of the gage mount was dimpled inward (2 to 3 mm). According to J. Quintana,

Figure 34 is the data plot from the debris-shielded Kulite gage sensing installation. Posttest inspection of the installation revealed the effects of the severe environment (fig. 35). One web of the debris shield was impacted by competent debris, which caused severe deformation of the web. However, the debris shield did effectively prevent damage to the transducer from the direct impact of debris on the sensitive area of the unit. The geometry of the steel module showed very little deformation. However, some deformation occurred in the connector shell in that the module could not be unplugged normally and removed from the body. A post-mortem dissection of the transducer revealed that a portion (shaped like a truncated cone) of the silicon disk sensing element was dislodged from the backside, and this destroyed the electrical strain-sensing elements located in the active area of the transducer. Microscopic examination of the cavity created in the backside indicated crystal line shear failure from massive overstressing of the element due to overpressure. Electrical continuity of the land-line cable to the sensing location was checked, and all conductors were intact and operational.

Thus, further development of the driver-pressure measurement technique is necessary. This will probably involve the use of much more rugged gages (ytterbium or carbon).

MAGNETOHYDRODYNAMIC VELOCITY GAGE

The magnetohydrodynamic technique of generating power has long been known and has recently come into *vogue* as one of the possible alternatives for the production of electrical power. The use of this principle to design a flow or particle-velocity gage appears attractive, since a self-generating measurement is involved.

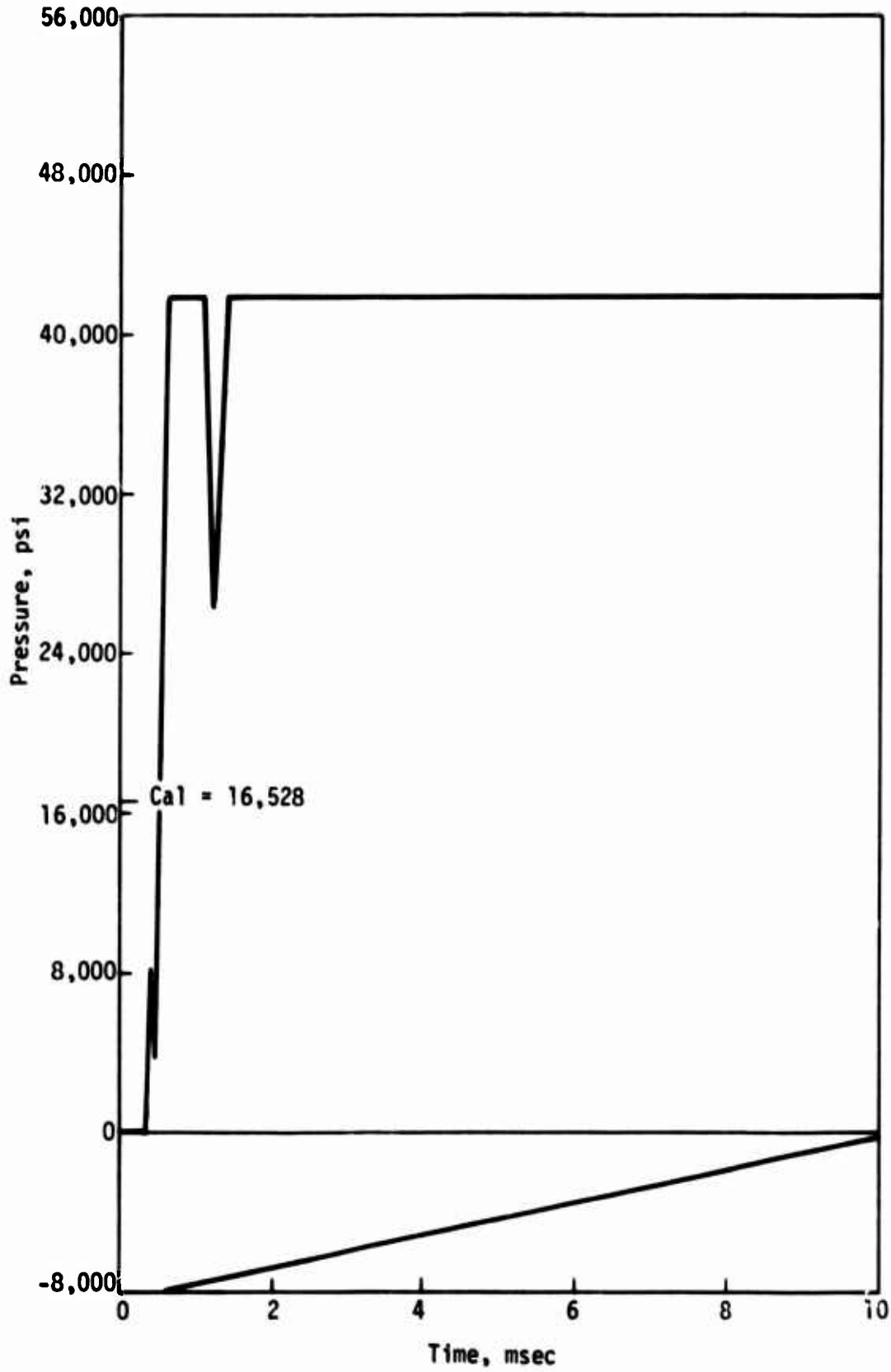


Figure 32. Bar Gage Driver Pressure from DABS IE



Figure 33. Bar Gage Mount After Test

The principle is briefly explained in figure 36. If two parallel conducting plates (parallel to the xz -plane) are oriented so that the flowing gases in a shock wave can pass between them, the flow velocity can be determined through the utilization of a magnetic field. If \vec{F} is the force on a charged particle in the flow, \vec{V} the velocity of that particle, n_1 the number of particles with q_1 charge, B the magnetic field, and E the electric field, with Einstein notation the Lorentz force equation can be written

$$\vec{F} = n_1 q_1 (\vec{E} + \vec{V} \times \vec{B})$$

Now if it is presumed that there is some measurement resistance (gage termination resistance) between the plates that is much greater than that caused by the resistance of the hot gases in the flow, the current flow between the plates will be essentially zero or

$$F_y = n_1 q_1 (E_y - V_x B_z) = 0$$

or

$$E_y = V_x B_z$$

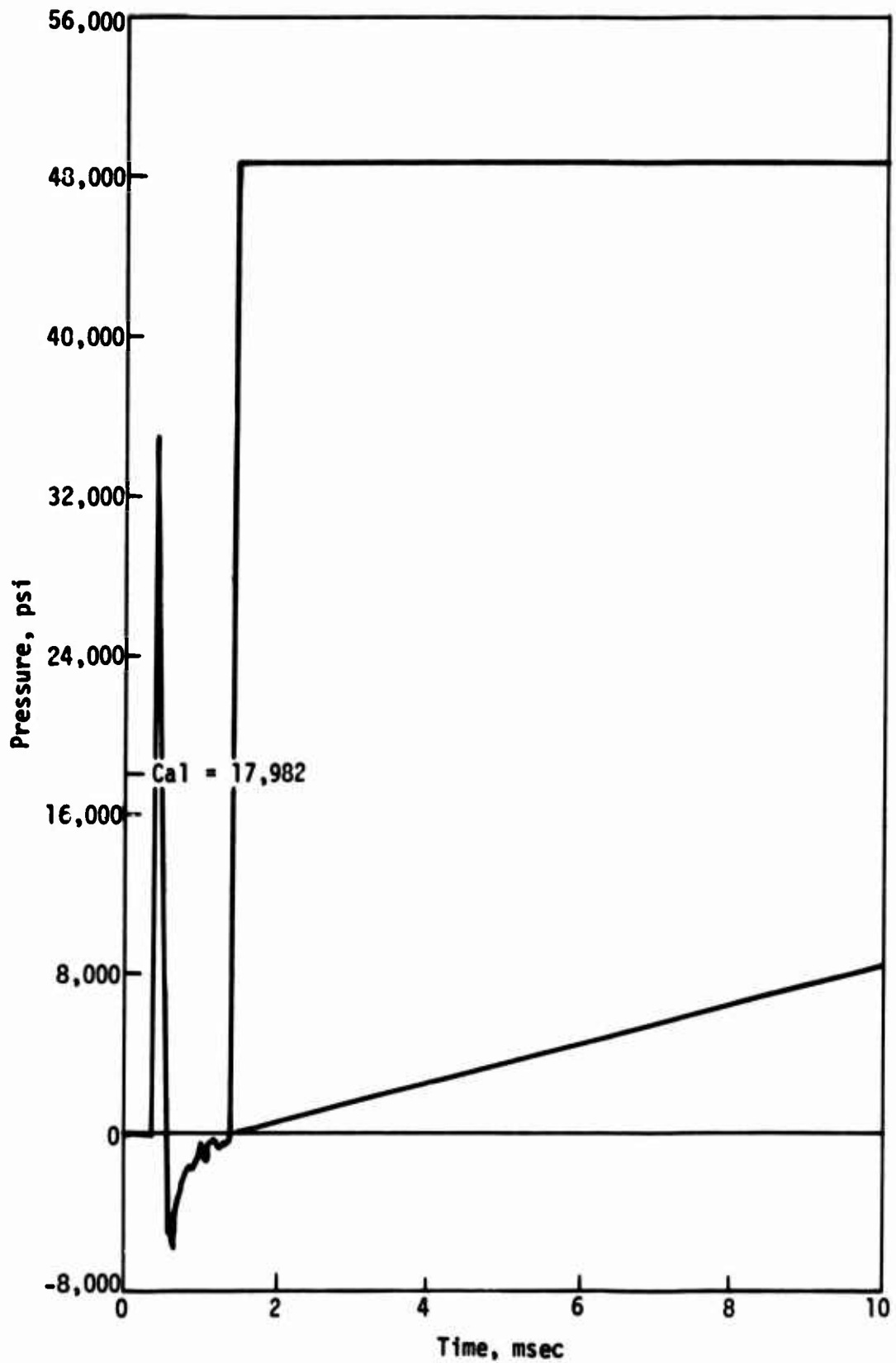


Figure 34. Kulite Gage Driver Pressure from DABS IE

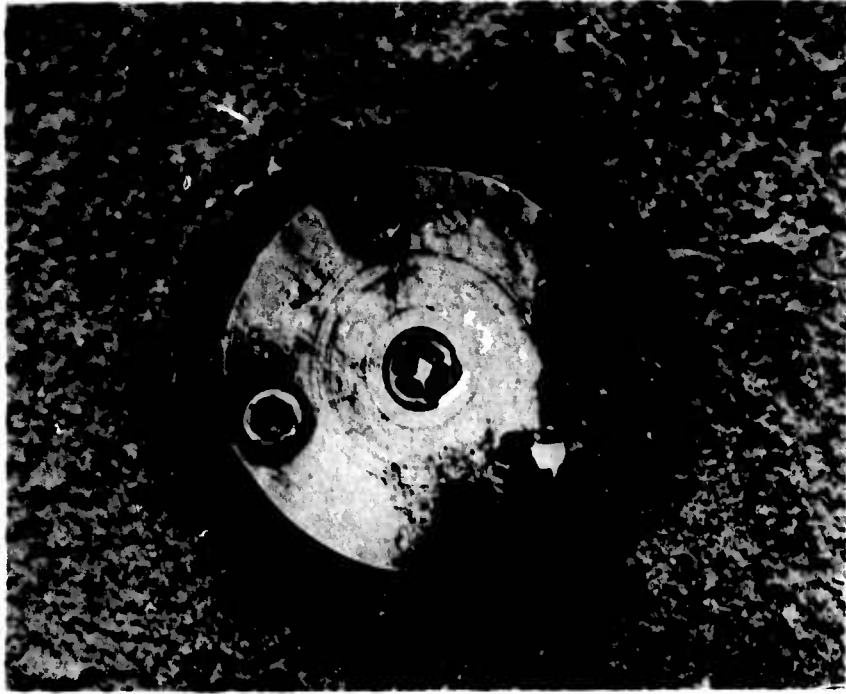


Figure 35. Kulite Gage After Test

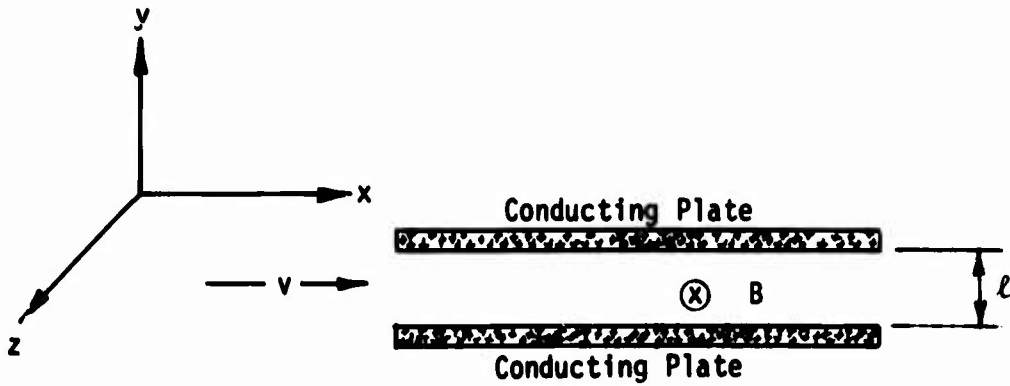


Figure 36. Principle of Magnetohydrodynamic Velocity Gage

If v is the voltage between the two plates and ℓ is the distance between the two plates,

$$v = V_x \ell B_z$$

Therefore, if the distance between the plates and the magnetic field are known, a reading of the voltage between the plates becomes a direct measure of the flow velocity. This measurement is completely independent of the charges in the flow in so far as the conductivity of the flow is high with respect to the measurement resistance.

The promise of this type of system was obvious and Artec Associates, Inc. of Hayward, California was funded to pursue its development. The report on this effort is contained in appendix D. In conjunction with this effort an experiment was conducted on DABS IB. The purpose of which was to qualitatively determine if the conductivity within a DABS flow was high enough for a magneto-hydrodynamic experiment.

The experiment consisted of placing two 1-ft² copper plates 1 ft apart in the floor of DABS. One surface of each plate was exposed and the other was insulated with REN Plastics RP-3269-1 Epoxy. The plates were interconnected through a 1-M Ω resistance. The signal across this resistance was buffered through an operational amplifier and a 75- Ω output impedance was used to drive the signal cable.

The observed signal in this experiment oscillated between peak values greater than 30 V. It was believed that static charge deposition on the plates was the reason for this and thus some seeding would be needed. The chosen seed material was potassium chloride. It was chosen over the more optimal cesium chloride because of cost.

Briefly, the result of Artec's experimental effort was that the conductivity of the flow for DABS conditions is not high enough to obtain a reasonably noise-free signal even if the flow is seeded. Thus it was decided not to field these gages on a DABS experiment. However, in spite of the unfavorable signal-to-noise ratio, it was obvious that the velocity signal was present. With higher pressures, such as those achieved in a nuclear test or in the trench program, the performance will improve and the gage should be considered for these types of programs.

SECTION 8 CONCLUSIONS AND RECOMMENDATIONS

Phase I of the DABS instrumentation development has come a long way in the exploration of new and novel techniques for blast instrumentation. Although successes have been significant, there remains areas in which further development is needed. This will probably be the case for some time, since DABS measurements are made in an extremely adverse atmosphere.

The use of a traffic-control radar unit to obtain useful data is one of the unique techniques that has come out of this program. Although one has yet to be built, the Eulerian microwave particle velocimeter is theoretically and economically feasible. The need for particle velocity data from DABS and the opportunity to develop anemometers that would be useful for related and totally different applications make the velocimeter one of the most promising devices.

Complementary data obtained from infrared measurements of the time-of-arrival of the interface between the detonation products and the clean air shock have been useful. Although the technique needs some minor refinement, the obvious extension of making temperature measurements should be pursued. This type of temperature measurement involves the use of a number of infrared detectors with narrow band infrared filters. The data obtained will be self-sufficient proof or disproof of the technique. If the data show that the spectrum is a black-body spectrum, the temperatures will be uniquely defined; if the data do not follow a black-body spectrum, the temperature will not be defined. Contingent upon the failure of this method, some of the more exotic infrared and optical techniques should be considered. Some of these techniques are described in appendix E. Also, additional consideration and development should be given to AFWL's heat-transfer gage. This might also be extended to intrinsic thermocouples.

The results from the optical photodiode were somewhat anomalous in that they radically conflicted with previous photographic data. However, these data reopened the possibility of doing optical experiments such as holography and rotational Raman measurements. However, since these experiments are extremely

expensive to field both in equipment and labor, they should be undertaken only after a low-cost feasibility experiment has been conducted. If this feasibility experiment shows results that indicate a high probability of success with these experiments, then and only then should they be considered.

The debris-collection experiments indicated that debris impact is a probable contributor to the second pulse on the pitot tube measurements in DABS. However, more work needs to be done on closure mechanisms for the debris collectors. Additional considerations should also be given to improvement of the explosive-closing debris collector that traps a segment of the flow. If they can be made to work, they would probably give a time-history record of the size and density of the debris. However, until they are developed, debris collectors similar to those presently used should be fielded. The upcoming variation of explosive drivers necessitates this, since the absence of the plastic jacket containment of the explosive will certainly affect the quantity of debris in the flow.

Although the shock-on-shock experiment was a qualified success, the configuration of the experiment should be changed as recommended in the body of this report. This experiment should be fielded on all possible DABS.

Some advance must be made if driver-chamber pressure is to be measured in DABS. The attempted transduction schemes were clearly inadequate. The most promising devices in this area are the higher-stress ground-shock transducers (carbon and ytterbium). The magnetohydrodynamic velocity gage clearly cannot be used on DABS unless higher pressure levels are achieved. Based on experience with this gage, it clearly functions well when the conductivity is high enough and may have pertinent application on other types of tests such as underground nuclear tests. The bar gage is essentially operational and can be used in lieu of or in addition to normal commercially available gages. There still exists a definite need for a debris-independent pressure gage. This will have to be accomplished if the gas dynamic properties of the flow are to be ascertained. AFWL has been working on this problem with some success and certainly this work should be continued. If this effort is ultimately successful, blunt cylinder drag measurements should be undertaken. These measurements can be used to determine the mach number of the transonic flow (appendix F).

APPENDIX A
DOPPLER RADAR SYSTEM FOR
DYNAMIC AIRBLAST SIMULATOR

	<u>Page</u>
Introduction	74
Radar Unit	74
Frequency Response Test	75
Blast Wave Perturbation	76
Prototype DABS Radar Experiment	80
Conclusions and Recommendations	85

INTRODUCTION

The purpose of the Dynamic Airblast Simulator (DABS) is to load defense structures with airblast pressure similar to that expected from a nuclear detonation. One of the principal quantities to be measured is the particle velocity in the shock wave. It is proposed that a thin aluminum-foil target in the shock wave be tracked by a doppler radar system. The evaluation of such a system and the results obtained with the small-scale prototype DABS, constructed by the University of New Mexico Civil Engineering Research Facility for the Air Force Weapons Laboratory, are presented. A description of the radar unit, the testing of its frequency response, a theoretical look at the possible perturbation of the signal due to the blast wave itself, and the experimental design and results of the prototype DABS radar experiment are included.

RADAR UNIT

The radar unit was a Model JF 100 Speed Gun manufactured by CMI, Inc., Minturn, Colorado. In its normal configuration it is a hand-held, traffic-control, doppler radar device which gives a digital display of velocity in miles per hour. The pertinent specifications as given by the manufacturer are as follows:

- (1) Frequency -- $10,525 \pm 25$ MHz
- (2) Polarization -- Circular
- (3) Beam Width -- 8° or Less (Side lobes suppressed greater than 24 dB down)
- (4) Antenna -- 4-Inch Aperture; Circular Horn Type
- (5) Microwave Oscillator -- Solid-State Gunn Diode
- (6) RF Power -- 20 mW Minimum; 100 mW Maximum
- (7) Receiver Diode -- Schottky Barrier Type Rated for 100-mW Burnout

The unit was ordered without the digital display and its associated electronics since they were not pertinent to the experiment. Thus, the total unit consisted of an antenna, a preamplifier, an amplifier/regulator, a 9-V regulator, and the housing. The system was powered by a 12-V car battery.

The signal was taken from the output of the preamplifier and ac-coupled (high pass 30 Hz, 3-dB point) because of a dc-offset. The only other modification made was the removal of all low-pass filtering from the preamplifier. The output impedance of the device was 1000 Ω . This recorded signal is the amplified doppler signal. Its relationship to the velocity of the target is

$$f_d = \frac{2Vf_r}{C} \quad (A1)$$

where f_d is the doppler frequency, V is the velocity of the target, f_r is the radar frequency, and C is the speed of light. If the unit of velocity is feet per second and the frequency is in Hertz, eq. (A1) reduces to $f_d = 21.40V$.

FREQUENCY RESPONSE TEST

Since the system is normally used to track motor vehicles at speeds up to 200 mph, it was deemed appropriate to use targets with velocities approaching those measured in a shock wave. The fastest target readily available was a rifle bullet which weighed 150 grains. A Remington Model 700, 7-mm Magnum was used to propel the target.

The rifle was aimed so that the bullet would pass within a few inches of the radar antenna, and the doppler signal was recorded on a Bell & Howell Model 3700B Tape Recorder. First, the bullet was fired approximately parallel to the radar beam, both toward and away from the radar unit. The measured velocity was in both cases 3198 ft/sec. Since the listed muzzle velocity of the rifle is 3260 ft/sec, this result was assumed to be accurate. However, to further check the system, the radar unit was placed so that the angle between the beam and the bullet path was approximately 20 deg. The results of this test are shown in figure A1; the measured velocity was 2803 ft/sec. Since the ratio of this velocity to the straight-on velocity equals the cosine of 19 deg, it was verified that the radar unit had tracked the bullet.

The only point of possible concern was the magnitude of the voltage. The voltage was approximately 0.2 V peak-to-peak (fig. A1). If the system records lower velocity inputs from a moving bullet close to the radar unit, the preamplifier

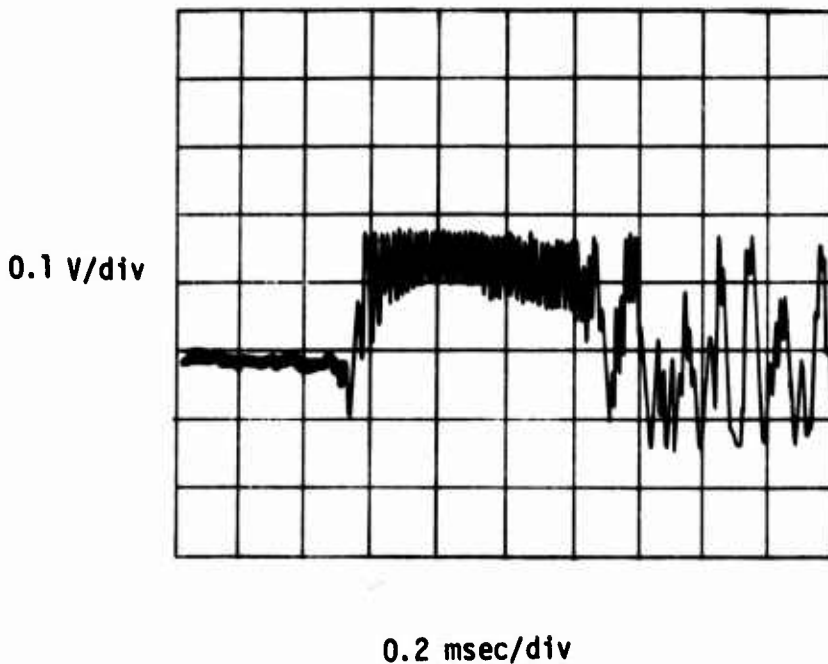


Figure A1. Doppler Signal from Rifle Bullet

will saturate and give a signal of ± 5 V. Thus, the signal will be attenuated by 27 dB. However, it was felt that the magnitude was more than sufficient and signals generated from targets moving at velocities of 4000 to 5000 ft/sec should be easily discernible.

BLAST WAVE PERTURBATION

Since the radar beam tracks a target inside a shock wave, the effects of the shock wave on the microwave beam must be considered. Such effects can possibly arise from the ionization and the increase in air density behind the shock front.

The effect of ionization on the index of refraction, n , of an ionized medium can be expressed to the first approximation by

$$n^2 \approx 1 - \frac{\omega_p^2}{\omega^2} \quad (\text{A2})$$

where ω is the incident radiation and ω_p is the plasma frequency (ref. 1). This relationship shows that when the plasma frequency is greater than the incident frequency, the index of refraction becomes imaginary and the medium totally reflects the incident radiation. In a cgs system of units, the plasma frequency may be expressed by the relationship

$$\omega_p = \frac{4\pi\alpha e^2}{m} \quad (A3)$$

where α is the number of free electrons per cubic centimeter, e is the electron charge, and m is the mass of an electron. Thus, in this radar experiment, in which the incident radiation was 10.525 GHz, the electron density would have to be approximately 3.5×10^{10} electrons/cm³ for this condition of total reflection to occur. Saha (ref. 2) and Predvoditelev (ref. 3) indicate that electron densities are much less than this for the pressures and temperatures expected inside the shock wave produced by a DABS event. However, this disagreement does point out one important design criterion for the radar system; viz., it must be constructed so that the radar target intercepts all or nearly all of the microwave beam since the hot gases generated by the detonation used to drive the shock wave will also reflect the beam and thus generate an additional doppler signal.

The second perturbation to be considered is the effect of the change in air density in the shock wave on the doppler signal. The origin of this effect can be seen if one rewrites eq. (A1) as

$$f_d = - 2[d(nx)/dt]/\lambda \quad (A4)$$

where x is the distance between the radar unit and the target, and λ is the wavelength of the radar beam. If it is assumed in the first approximation

-
1. Jackson, J. D., *Classical Electrodynamics*, John Wiley and Sons, Inc., New York, N.Y., 1962.
 2. Saha, M. N., and Srivastava, B. N., *A Treatise on Heat*, 3rd Edition, Indian Press, Ltd., Calcutta, India, 1950.
 3. Predvoditelev, A. S., *Physical Gas Dynamics*, Pergamon Press, New York, N.Y., 1961.

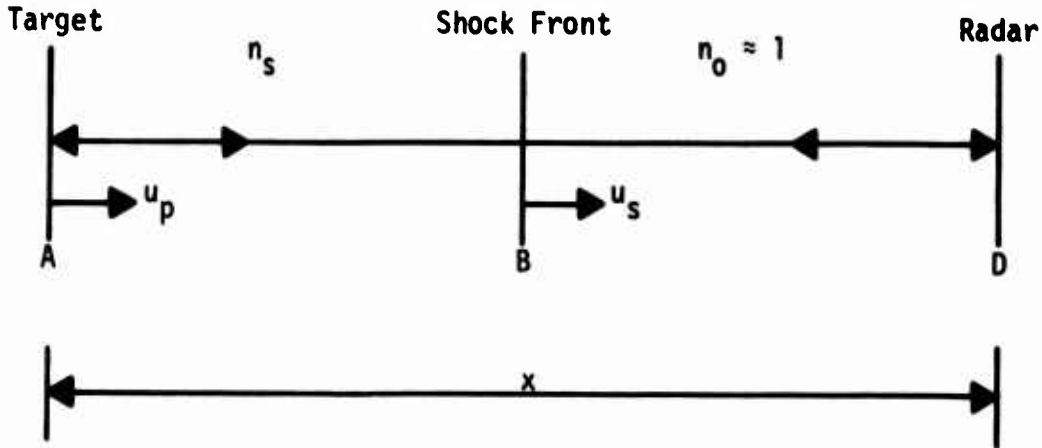


Figure A2. Density Effects

that the index of refraction is some constant value, n_s , behind the shock front and n_0 in front of it, then with the notation of figure A2,

$$x = n_s AB + n_0 BD$$

Substitution of this into eq. (A1) yields

$$f_d = 2 \left[n \frac{dAB}{dt} + n_0 \frac{dBD}{dt} \right] / \lambda$$

With u_s as the shock velocity and u_p as the particle velocity,

$$\frac{dAB}{dt} = u_p - u_s$$

and

$$\frac{dBD}{dt} = u_s$$

or

$$f_d = \frac{2 \left[n_s (u_p - u_s) + n_0 u_s \right]}{\lambda} \quad (A5)$$

The percentage of error in the particle velocity measurement because of this effect is

$$\left[\frac{100}{n_0} (n_s - n_0) + (n_0 - n_s) \frac{u_s}{u_p} \right]$$

As an example, if the index of refraction increases by 10 percent and the ratio of the shock velocity to the particle velocity is about 5:4, the error in the particle velocity measurement is only 2.5 percent with $n_0 \approx 1$.

The change in density will cause a change in the index of refraction that is much smaller than that estimated in the example. If, as a first approximation, one uses the Drude model,

$$\frac{d\rho}{\rho} = \frac{dn}{n - 1}$$

where ρ is the density; since for a ratio, γ , of the isobaric specific heat of air to the isovolumetric specific heat of air of 1.4 the density only changes by a maximum factor of 6 (ref. 4) and the index of refraction of air at standard temperature and pressure is only slightly larger than 1, the change in the index is quite small.

The last point to consider is the reflectivity of the shock front itself compared to the target. But since the reflectivity, R , of the front may be shown to be

$$R = \frac{n_s - n_0}{n_s + n_0}$$

and the change in the index of refraction at the shock front is quite small, reflectivity of the shock front is negligible. Thus for the expected conditions encountered in DABS, the blast-induced perturbations on the measurement of the particle velocity are insignificant.

4. Zel'dovich, Ya. B., and Raizer, Yu. P., *Physics of Shock Waves and High-Temperature Hydrodynamic Phenomena*, Vol. I, Academic Press, New York, N.Y., 1966.

PROTOTYPE DABS RADAR EXPERIMENT

Basically a disposable shock tube constructed from a corrugated pipe arch was used in the prototype DABS radar experiment. The pipe was 160 ft long and its cross section was approximately oblate (\approx 8 ft wide by 5 ft high). Figure A3 shows the basic layout for the radar particle-velocity experiment.

The target consisted of three layers of 0.001-in-thick aluminum foil, spaced 0.5 in apart. The target was placed normal to the direction of shock propagation and completely blocked the tube. This target design was chosen for the following reasons:

- (1) Rise Time. The round-trip shock transit time in each 0.001-in foil is less than 10 nsec. Thus, with 6 to 10 transit times allowed for the foil to come up to the particle velocity, the rise time of the target becomes 60 to 100 nsec. Since this figure is much better than the effect of possible misalignment and lack of planarity with respect to the shock front and since the expected doppler frequencies are in the range of 90 to 100 kHz, the target should be adequate.
- (2) Opacity. Since the target as previously explained must shield the microwave beam from the detonation products, a three-layer spaced system was chosen. It was felt that even after the possible turbulence in and behind the shock front had shredded the target, the three-layer system would not allow the microwave beam to propagate through it; i.e., the gaps in the target would, for the most part, be smaller than the half wavelength of the microwave beam (\approx 1.4 cm).

The radar unit was placed 20 ft downstream from the target and aimed directly at its center (fig. A4). Since the beam width was only 8 deg, the reflected

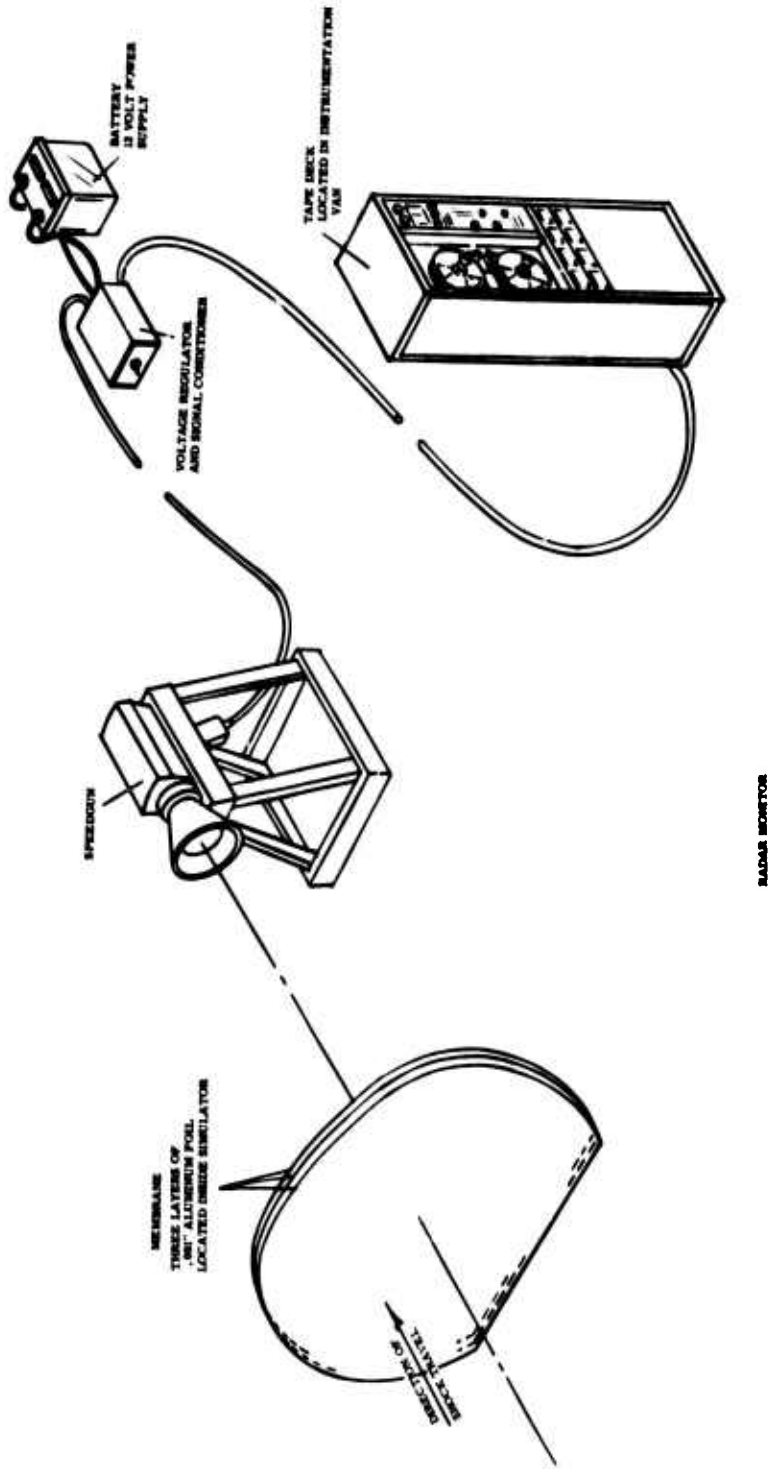


Figure A3. Layout for Particle-Velocity Experiment

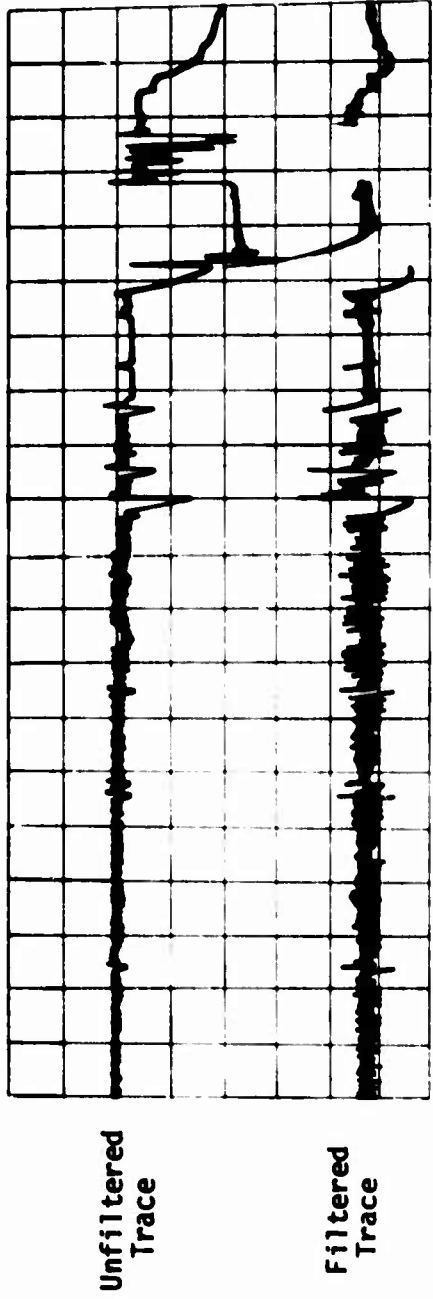
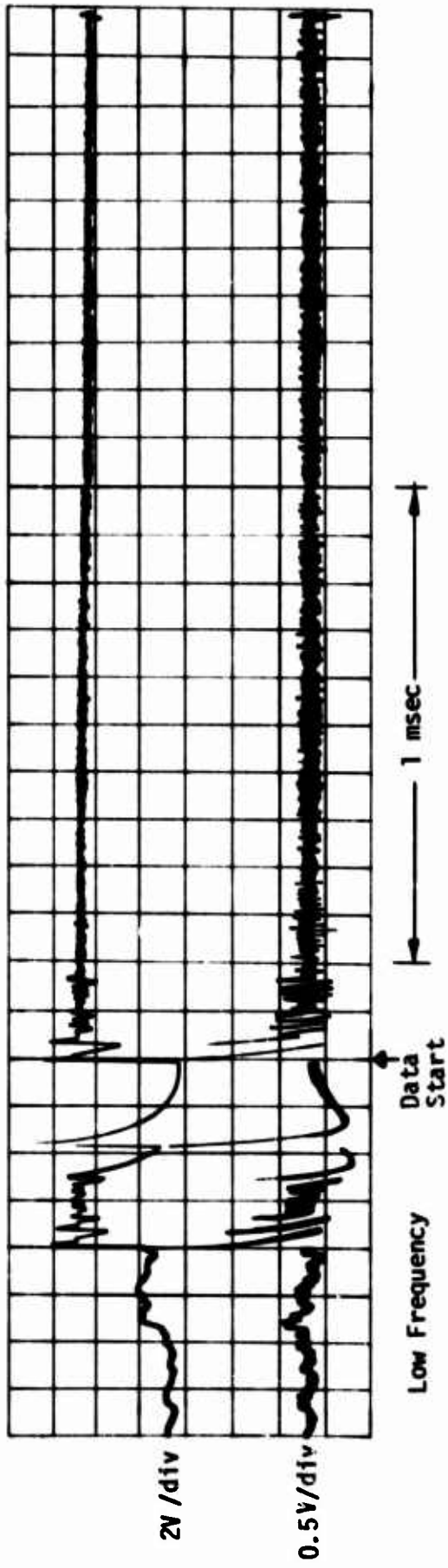


Figure A4. Location of Radar Unit for Test

signal came from the target and not from the walls of the tube. The doppler signal was recorded on two channels of a Bell & Howell Model 3700B Tape Recorder. One of these channels was ac-coupled (high pass 10 kHz, 3-dB point); this channel was a Bell & Howell Wideband II FM Channel with a 500-kHz response. The unfiltered channel was a Bell & Howell Wideband I FM Channel with an 80-kHz response.

The results of the experiment are shown in figure A5. The initial low-frequency signal was probably caused by wall vibrations coupling into the target before the arrival of the shock front. The period of the data was measured with a traveling microscope and the data were divided into 10 approximately equal segments.

The average period measured was 10.41 μ sec (96 kHz) and the standard deviation was 0.36 μ sec. This corresponds to a particle velocity of 4489 ft/sec.



Radar Destroyed

Figure A5. Doppler Radar Signal

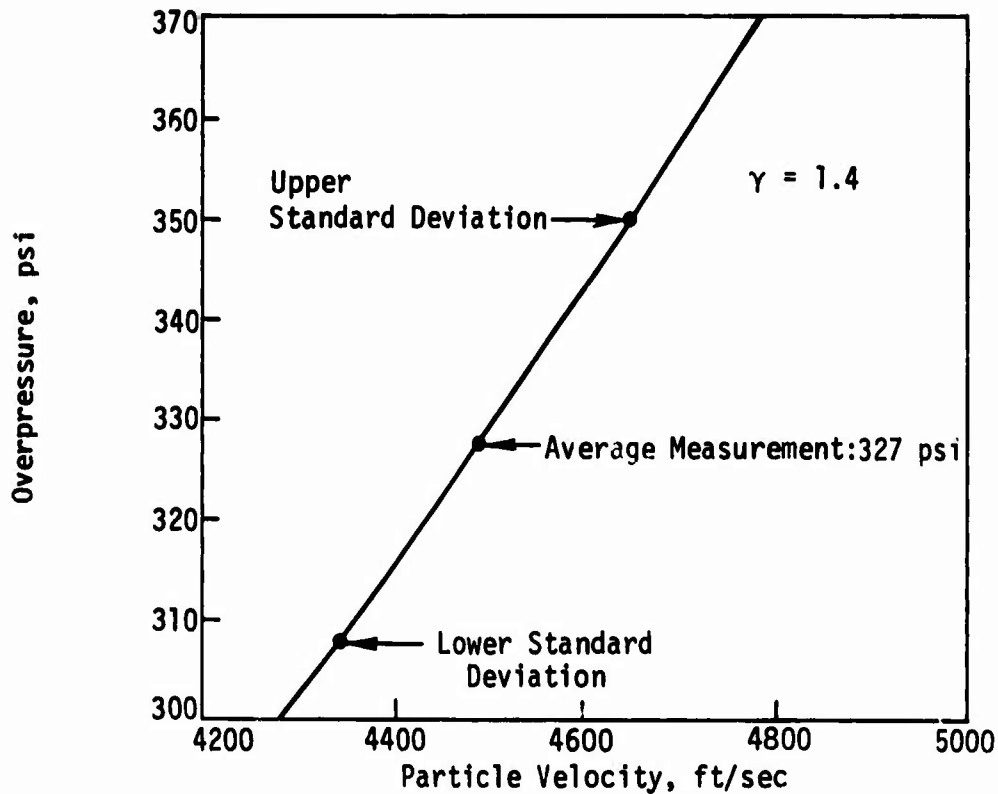


Figure A6. Particle Velocity Versus Overpressure

With the relationships

$$u_s = c_0 \sqrt{\frac{(\gamma - 1) + (\gamma + 1) \frac{P_1}{P_0}}{2\gamma}}$$

and

$$u_s - u_p = u_s \frac{(\gamma + 1) + (\gamma - 1) \frac{P_1}{P_0}}{(\gamma - 1) + (\gamma + 1) \frac{P_1}{P_0}} \quad (\text{ref. 4})$$

where P_1 is the absolute pressure in the shock wave and P_0 is the absolute pressure of the unshocked air (12 psi in and around Albuquerque, New Mexico) and with a γ of 1.4, the curve of particle velocity versus overpressure (fig. A6) can be generated. The average value of 327 psi agrees quite well with the incident pressure measured in DABS. At the closest station (≈ 20 ft upstream), the measured pressures varied from 320 to 350 psi. The shock velocity approximately 10 ft upstream (5765 ft/sec) indicates a pressure of 345 psi.

CONCLUSIONS AND RECOMMENDATIONS

The prime conclusion from this study is that the doppler radar system can measure the particle velocity in the airblast wave produced by DABS. However, it should be noted that the scope of this effort only permitted the measurement of particle velocity at one point (327 psi) but it certainly can be assumed that the system will function at lower pressures than this. The system should be adequate at pressures of at least 600 psi, since ionization should not pose a problem. However, this conclusion must await experimental verification.

A more adequate frequency analysis of the data should be undertaken in order to reduce the scatter in the data and develop a velocity profile. To accomplish this, high-frequency digitization (1 MHz) of the tape and Fourier analysis of the signal are presently being considered.

Since the output impedance of the device is relatively high, it should be buffered to a much lower impedance so that the line may be terminated to obtain a better frequency response.

Experiments in which metal reflectors are used for the microwave beam should be undertaken since they would shield the radar unit from the flow field and thus the unit could be reused.

APPENDIX B
RADAR TECHNIQUES FOR VELOCITY FIELD
MEASUREMENTS BEHIND A TUNNEL-CONFINED SHOCK WAVE

	<u>Page</u>
Introduction	88
Microwave Doppler Velocimeter Theory	89
Plasma Effects	101
EM Wave Scattering	108
Bistatic Radar Equation	113
References	126

INTRODUCTION

When a large amount of explosive is detonated at one end of a tunnel, a shock wave with velocity up to Mach 6 or 7 is formed with corresponding peak pressure in the atmosphere. The overpressure above the ambient constitutes the shock front, along with rapid fluctuations in the dynamic pressure occurring behind the shock front.

The phenomena associated with such a blast consist of waves moving much faster than sound, in addition to "well behaved" acoustic waves, large but finite changes in pressure, density and temperature, wave fronts causing jumps or discontinuities in these parameters and finite particle velocities associated with these waves. These conditions are not consistent with acoustic wave theory and empirical measurements and calculations are required to determine the time variation of these quantities.

In order to perform such calculations, data are required for the variations in temperature and in pressure at different points in the tunnel. What is wanted is the time history of the pressure and its spatial distribution, a 4-vector quantity. The response time, or bandwidth, of pressure transducers, and their susceptibility to destruction in the blast, plus other limitations, such as temperature dependence of the pressure response, militate against their use in the main stream of the tunnel blast. Interference with the flow behind the shock front by the transducer cannot be tolerated. No suitable omnidirectional blast transducers exist for obtaining free-field time histories of the pressure in the blast wave.

Therefore, an approach to obtaining the desired data through velocity measurement and temperature measurement has been proposed. The measurement of velocity time histories at various points in the flow behind the shock front of the blast is the subject of this report. It is proposed to perform such measurements using a microwave analog of a laser Doppler velocimeter (LDV).

MICROWAVE DOPPLER VELOCIMETER THEORY

A. Background

Two types of velocity measurement approaches using Doppler velocimeters are covered in Refs. 3 and 4. The first (Ref. 3) optically homodynes the scattered energy from a moving particle in a fluid with a reference beam unscattered by the medium. The Doppler difference frequency is proportional to the velocity of the medium at the scattering point, which is known from the scattering angle.

The second type is described in Ref. 4. The separate coherent beams are focused on the same small volume in the fluid from different angles, and two different scattered radiations are heterodyned to detect a Doppler difference frequency which is proportional to the velocity in the medium for the volume illuminated.

B. Theory

The theory, as developed in Ref. 4, is readily adapted to a microwave analog of the laser system employing two beams. This theory will be expanded to provide insight to the design of a suitable velocity measurement system for application to the tunnel blast wave measurement problem. Figure B1 illustrates the geometry of the problem. The antenna apertures are assumed to be circular with Gaussian illumination so as to produce a Gaussian pencil beam pattern of diameter $2b_0$ at the $1/e^2$ level. Figure B2a illustrates the diffraction region for each beam and the intersecting volume V of Fig. B1. The two radiations are mutually coherent, being derived from the same source over identical path lengths, and with the same linear polarization. The planar phase fronts from the two beams interfere over the volume $\Delta x \Delta y \Delta z (1/e^2)$. A set of closely-spaced planar interference fringes in the beam crossover region occur as indicated in Fig. B2b. The spacing of these interference fringes is given by the half-wavelength $\lambda/2$, divided by the sine of the half angle between the two beams. Figure B2c indicates the relative signal amplitude regions for the $1/e$ and $1/e^2$ levels. The energy from either beam within this ellipsoid will be at or above 86.5% of maximum. At the parallel lines of phase reinforcement, the two waves will add constructively, elsewhere they will add in various degrees of phase opposition.

Separation between the maxima is $y = \frac{\lambda}{2 \sin(\theta/2)}$, where θ is the angle between the beams.

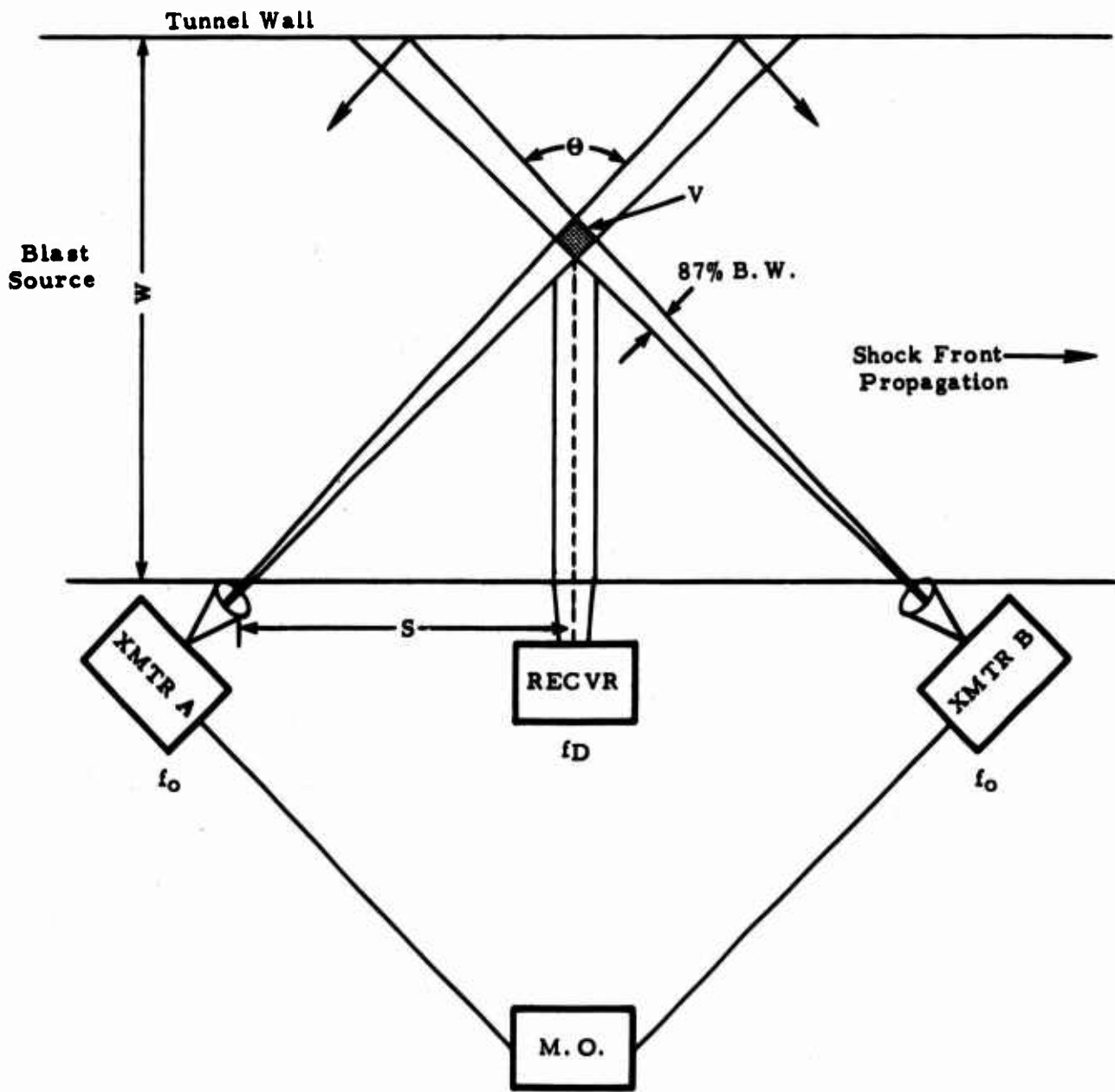
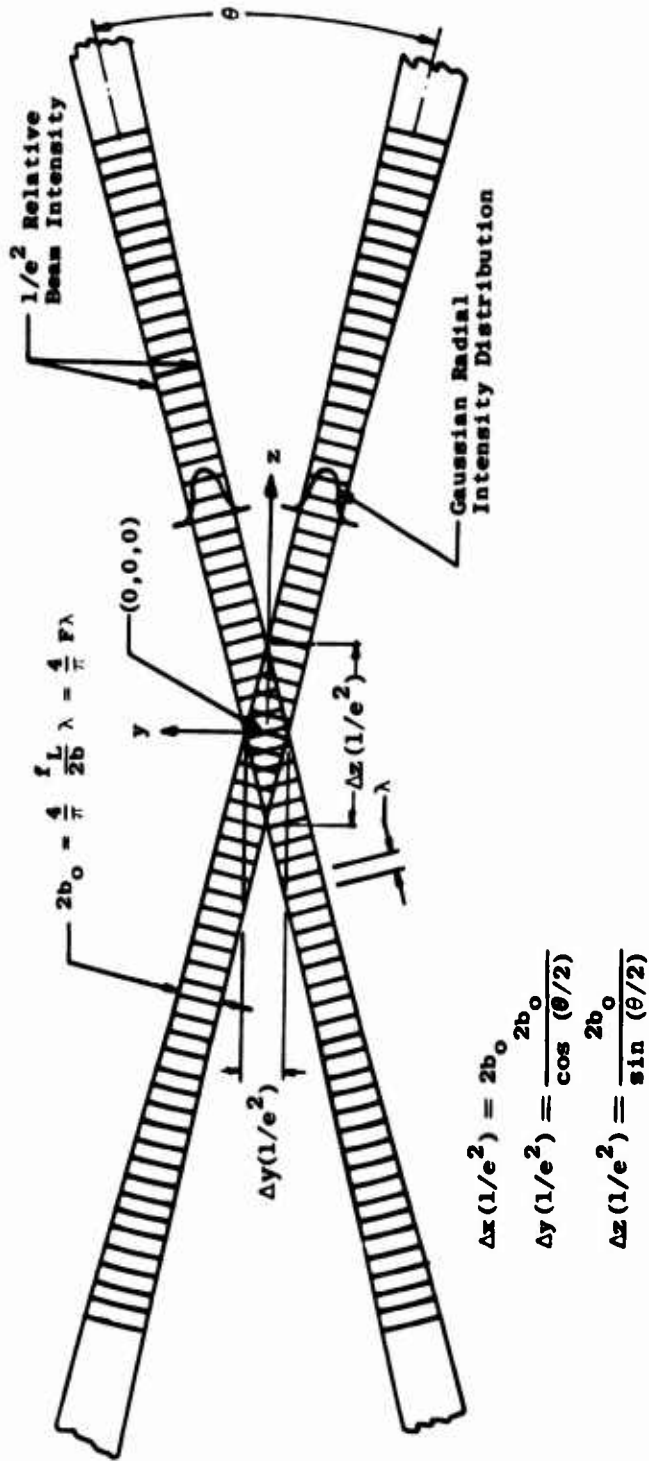
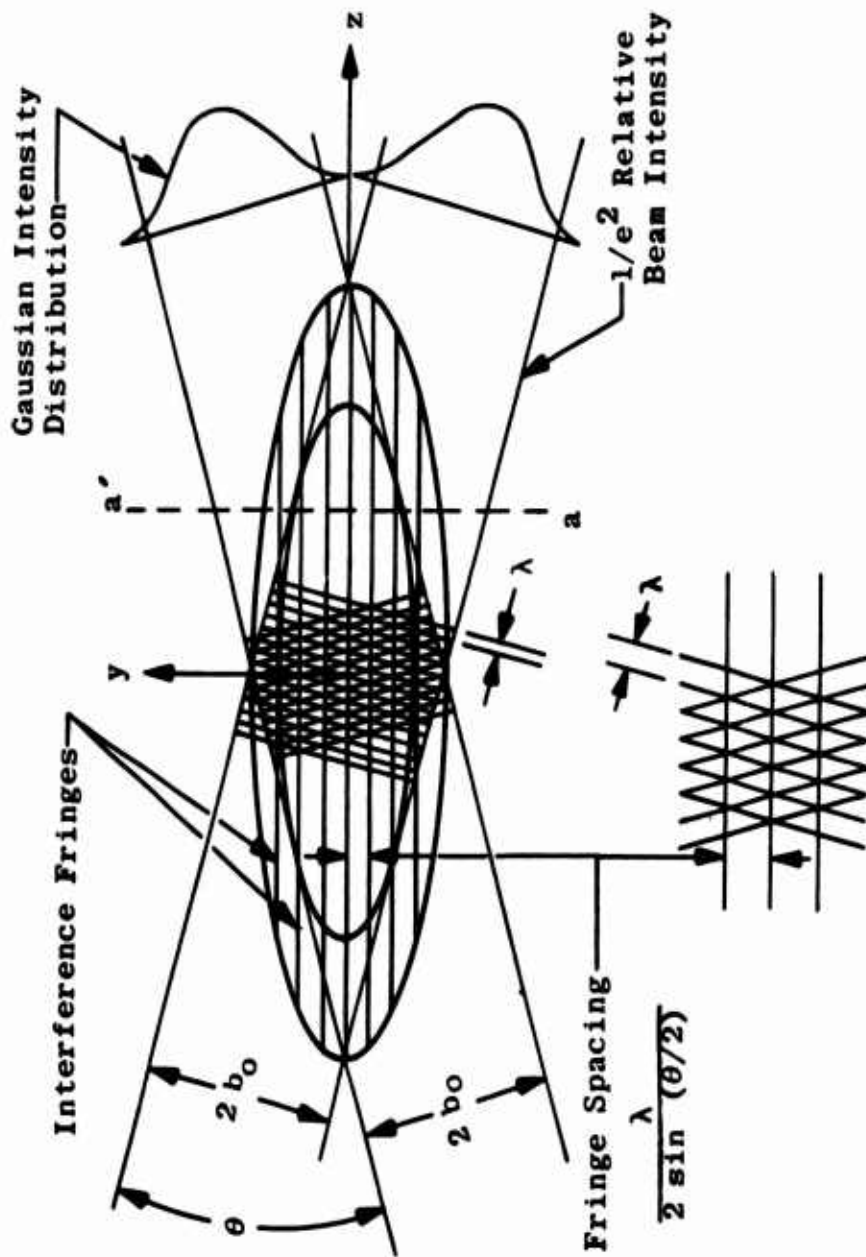


Figure B1. Conceptual Microwave Velocimeter



a. Schematic of Beam Crossover Region

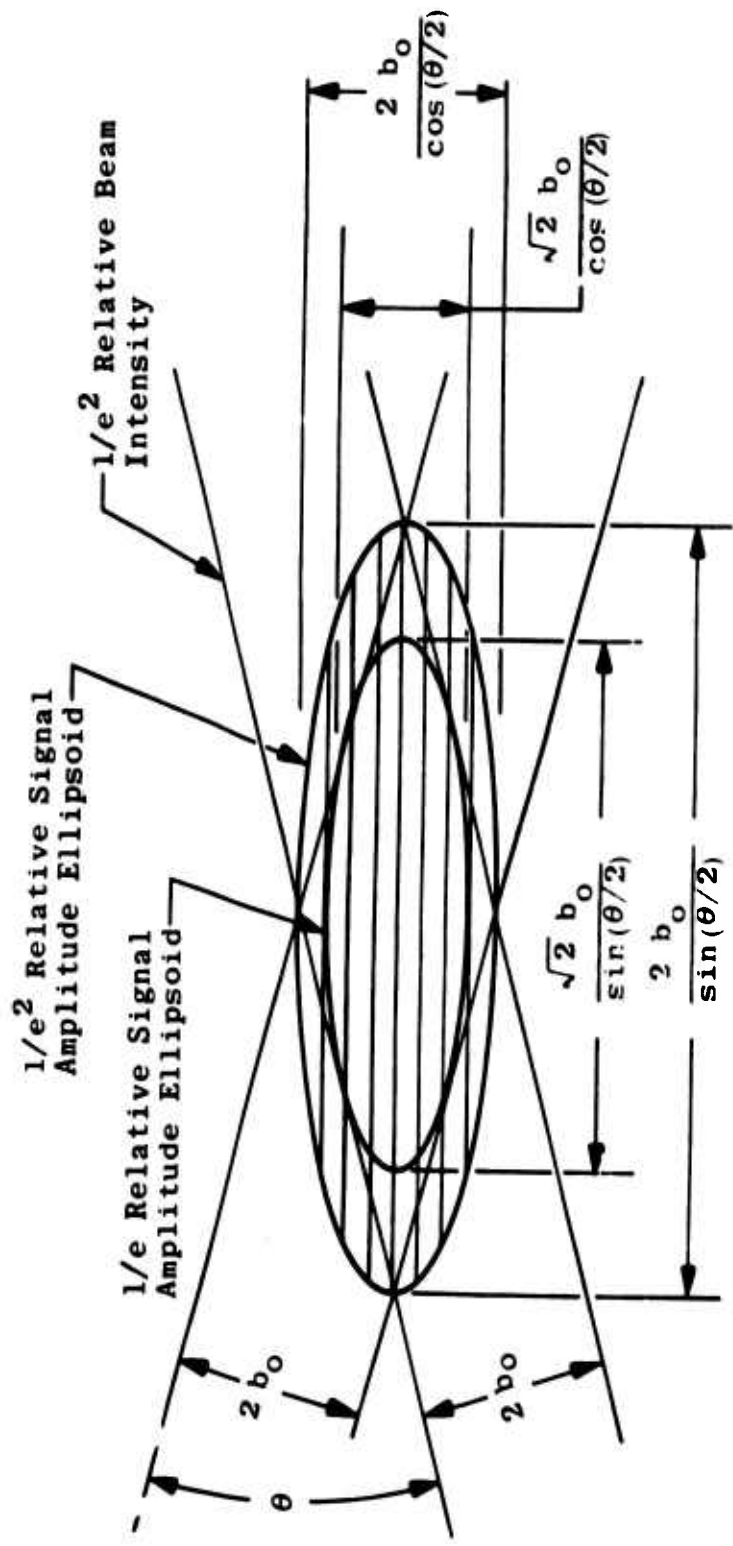
Figure B2. Laser Beam Crossover Region (Ref. 4)



Enlargement of Interference Region

b. Beam Crossover Fringes

Figure B2 (continued) (Ref. 4)



c. Relative Signal Amplitude Ellipsoids

Figure B2 (concluded) (Ref. 4)

A particle passing through this region (see Fig.B3) with velocity components v_y only, will cut the fringes at a rate proportional to its velocity and thus produce an alternating scattered signal at a frequency proportional to the velocity. The only component of velocity detected is that oriented normal to the interference fringes.

Since the amount of energy scattered in any direction is solely a function of the fringe pattern intensity at the point of scattering, the frequency is independent of the direction of scattering. This means that a larger scattering volume on receive will increase the sensitivity of the detection system.

The number of cycles (N) of information obtained from a scatterer passing through the center of the probe volume is given by

$N(1/e^2) = 2b_0 \frac{\tan(\theta/2)}{\lambda/2}$ where N is the number of cycles between the $1/e^2$ relative signal amplitude points, $2b_0$ is the $1/e^2$ beamwidth, and θ is the angle between beams. Obviously more cycles (and greater accuracy) result when λ is small, θ and b_0 are large. On the other hand, b_0 large reduces the positional resolution of a measurement. It is reemphasized that this development applies only to the discrete case of a single scatterer.

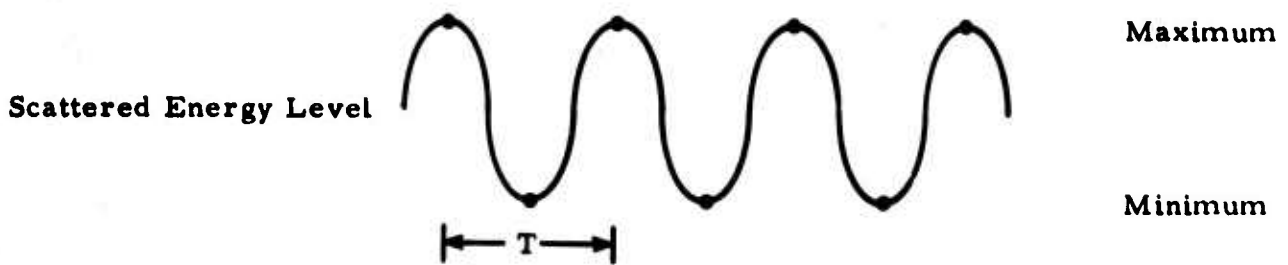
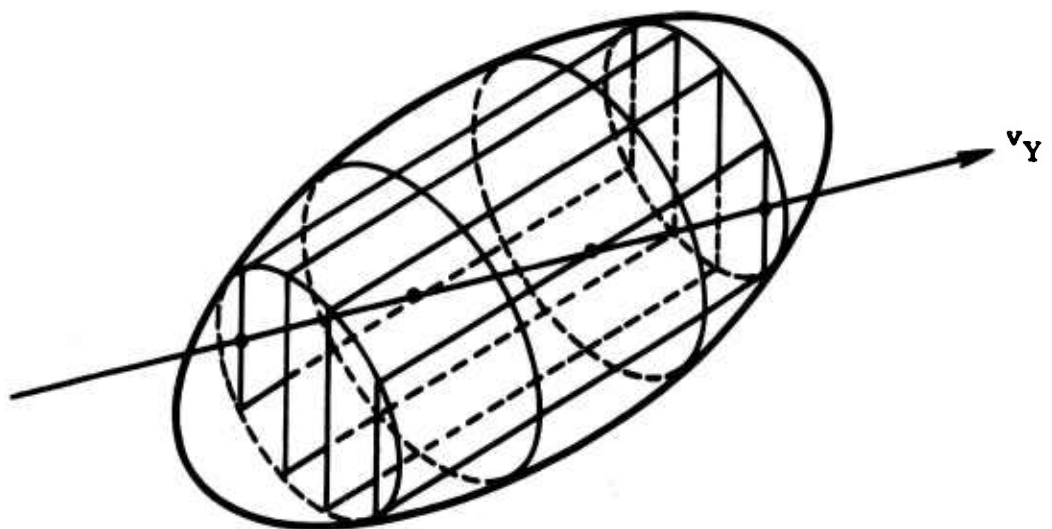
C. Differential Doppler Shifted Scattering

The Doppler shift in the energy scattered into any particular direction from beam 1 (Fig.B4), is given by

$$\Delta f_1 = \frac{1}{\lambda} (\bar{a}_s - \bar{a}_1) \cdot \bar{V} \quad (B1)$$

where f_1 is the Doppler shift in energy scattered in the direction denoted by the unit vector \bar{a}_s , \bar{a}_1 is a unit vector in the direction of beam 1, and \bar{V} is the velocity vector of the scattering center. The Doppler shift of energy scattered from beam 2 in the direction of \bar{a}_s is

$$\Delta f_2 = \frac{1}{\lambda} (\bar{a}_s - \bar{a}_2) \cdot \bar{V} \quad (B2)$$



$$f_d = \frac{1}{T} = \frac{v_Y}{\Delta Y} = \frac{2v_Y \sin(\theta/2)}{\lambda}$$

Figure B3. Cross Section of Ellipsoidal Interference Region

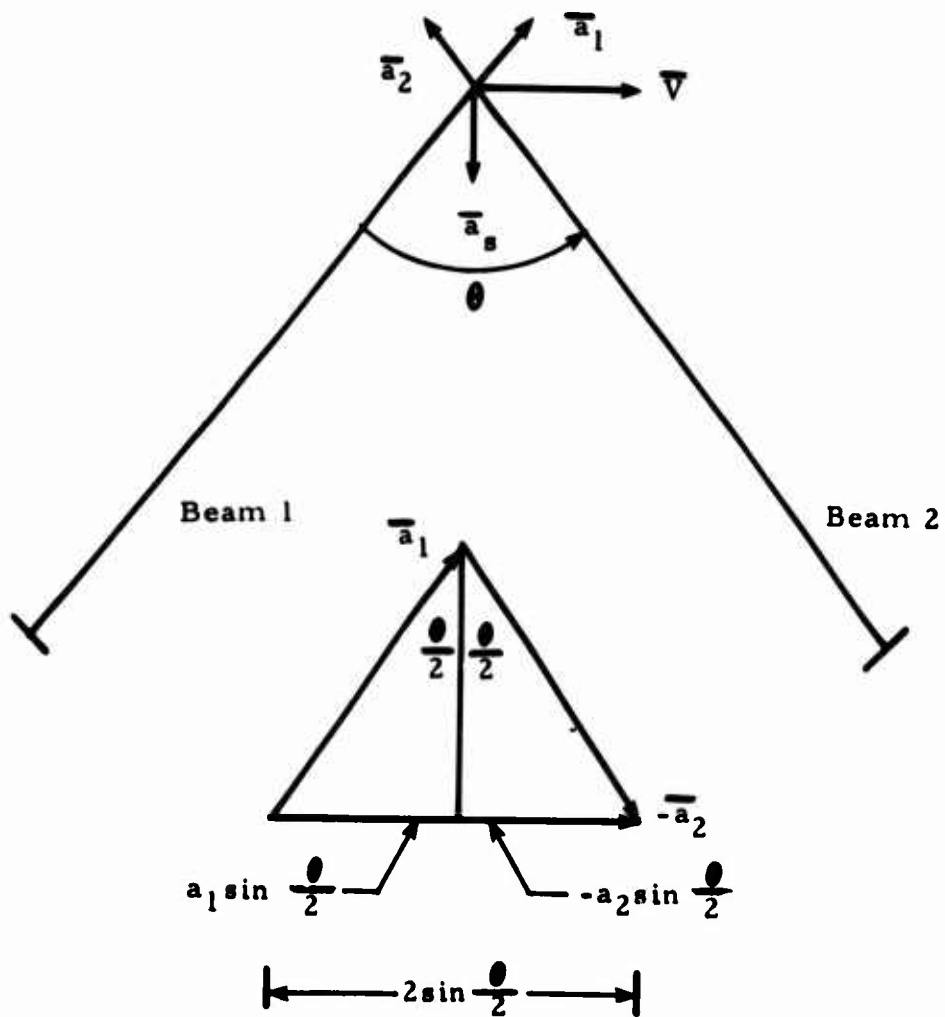


Figure B4. Doppler Difference Measurement Geometry

The output of a mixer with inputs of scattered signals from B1 and B2 includes a difference term between these Doppler shifts, oscillating at a frequency f_d :

$$f_d = \Delta f_2 - \Delta f_1 = \frac{1}{\lambda} (\bar{a}_1 - \bar{a}_2) \cdot \bar{V} \quad (B3)$$

The Doppler difference frequency is independent of \bar{a}_s , and as previously noted, the detector antenna position can be chosen for maximum collection of scattered energy. This frequency is also proportional to the velocity component in the direction of $\bar{a}_1 - \bar{a}_2$, which is perpendicular to the bisector of the two incident beams and in the plane of the two. For the situation of Fig. B1, the sensed velocity component V_s is given by $\frac{V}{\lambda} 2 \sin \frac{\theta}{2}$ since $|\bar{a}_1 - \bar{a}_2| = 2 \sin \frac{\theta}{2}$.

The differential Doppler signal will be modulated in both phase and amplitude, and will require analysis of the recorded output of the homodyne detector.

The frequency spectrum broadening over any given observation time is due to the residence time of a scattering center within the defined scattering volume or transit time, spatial variations in the velocity within the sample volume, and phase and amplitude variation differences for the two transmit beams over their separate propagation paths.

The mixer output power is proportional to the square of the incident fields scattered from the two beams:

$$P(t) \sim [E_1(t) + E_2(t)]^2 \quad (B4)$$

The power spectrum $P(\bar{K}_1, \omega)$ of the mixer output is the Fourier transform of the autocorrelation function for a stationary random process:

$$P(K_1, \omega) = R_e \int_{-\infty}^{\infty} \langle P(o) P(\tau) \rangle e^{-j\omega\tau} d\tau \quad (B5)$$

where the brackets denote the average of the ensemble for the autocorrelation function. Then

$$\langle P(o) P(\tau) \rangle \sim \langle [E_1(o) + E_2(o)]^2 [E_1(\tau) + E_2(\tau)]^2 \rangle \quad (B6)$$

The transmitted energy at the scattering volume has a time varying waveform

$$E_1(t) = E_2(t) = A(t) \cos[\omega_0 t + \alpha(t)] \quad (B7)$$

since the wave is affected by the time varying character of the propagation medium. Since the scattered fields at the receiving antenna are detected as the sum of $E_1(t)$ and $E_2(t)$, it will have time varying amplitude and phase depending on the position and motion of the scattering centers, and will be of the form:

$$E(t) = B(t) \cos \left\{ [\omega_0 + \Delta\omega(t)]t + \Delta\alpha(t) + \alpha(t) \right\} \quad (B8)$$

where $\alpha(t)$ is the varying phase angle due to propagation path phase shift of the two transmit beams over their separate propagation paths, $\Delta\omega(t)$ is the varying Doppler shift frequency component due to the composite motion effects of the scattering centers, and $\Delta\alpha(t)$ is a random phase shift caused by the random positions of the scattering centers.

If B6 is expanded we obtain

$$\langle P(o)P(\tau) \rangle \sim \langle [E_1^2(o) + 2E_1(o)E_2^2(o)] [E_1^2(\tau) + 2E_1(\tau)E_2(\tau) + E_2^2(\tau)] \rangle \quad (B9)$$

Without performing the expansion, it can be noted that certain terms will contribute to spectrum spreading and others will not. Of the nine terms, four containing factors of the following form integrate to zero value:

$$\langle \cos[\Delta\alpha(o)] \rangle, \langle \cos[\Delta\alpha(\tau)] \rangle, \langle \cos[\Delta\alpha(o) + \Delta\alpha(\tau)] \rangle$$

This is because the phase shift takes on all values and the average value of the sinusoids is zero.

The terms $\langle E_1^2(o)E_1^2(\tau) \rangle$ and $\langle E_2^2(o)E_2^2(\tau) \rangle$ will result in spectral components at frequency $2(\omega_0 + \Delta\omega)$ and zero (dc). The upper one will not appear in the mixer output. The dc terms have a varying amplitude of the form $\langle (1/4)[B^2(o)B^2(\tau)] \rangle$ which is due to the amplitude variation in the transmit beams and to the varying positions of the scattering centers. It is not due to the Doppler shift effect, or velocity of the scattering centers.

Two other nonzero terms at zero frequency (dc) result from the crosscorrelation of the two amplitudes B_1 and B_2 .

The final term contains the information of interest

$$\begin{aligned} & \langle E_1(o)E_2(\tau) E_2(o)E_1(\tau) \rangle \\ & = \langle 2MB_1(o)B_2(\tau)B_2(o)B_1(\tau) \cos \left\{ [\Delta\omega_2(\tau) - \Delta\omega_1(\tau)]\tau \right. \\ & \quad \left. + \Delta\alpha_2(\tau) - \Delta\alpha_1(\tau) + \alpha_2(\tau) - \alpha_1(\tau) \right\} \rangle \end{aligned} \quad (B10)$$

where

$$M = \cos [\Delta\alpha_1(o) + \alpha_1(o)] \cos [\Delta\alpha_2(o) + \alpha_2(o)] \quad (B11)$$

Now rewriting B10

$$\begin{aligned} & \langle E_1(o)E_2(\tau) E_2(o)E_1(\tau) \rangle \\ & = \langle 4B_1(o)B_2(\tau)B_2(o)B_1(\tau) \left\{ \cos [\Delta\alpha_1(o) + \alpha_1(o) + \Delta\alpha_2(o) + \alpha_2(o)] \right. \\ & \quad \left. + \cos [\Delta\alpha_1(o) + \alpha_1(o) - \Delta\alpha_2(o) - \alpha_2(o)] \right\} \cos \left\{ [\Delta\omega_2(\tau) - \Delta\omega_1(\tau)]\tau \right. \\ & \quad \left. + \Delta\alpha_2(\tau) - \Delta\alpha_1(\tau) + \alpha_2(\tau) - \alpha_1(\tau) \right\} \rangle \end{aligned} \quad (B12)$$

and it becomes apparent that there are numerous cross-products involving $\Delta\alpha$ and α . If the difference phase shift represented for example by the argument

$$\begin{aligned} & [\Delta\alpha_1(o) + \alpha_1(o) + \Delta\alpha_2(o) + \alpha_2(o) - \Delta\alpha_2(\tau) + \Delta\alpha_1(\tau) \\ & \quad - \alpha_2(\tau) + \alpha_1(\tau)] \end{aligned}$$

is uncorrelated for large values of τ , then the variable in the brackets is a random one, and its cosine averages to zero. This effectively would destroy the term in $[\Delta\omega_2(\tau) - \Delta\omega_1(\tau)]$. If the transit time of particles across the sampling volume is t_v , then at frequencies less than $1/t_v$ the random phase effects will mask the Doppler shift frequency difference which it is desired to detect. Therefore, the sampling volume should be kept as large as possible.

At a velocity of 300 fps or 91.4 m/sec, a 10 cm observation zone results in a transit time $t_V = 1.09$ msec, which approximately corresponds to a frequency of 1000 Hz. It is unlikely that the Doppler difference frequency would be observable below this velocity.

It must be realized that Fourier analysis of the detector output will be required to extract the velocity information from the broadened spectrum due to the random phase shifts with time. The receiver amplifiers should be designed to accommodate a spectrum broadening of 5 percent greater than the maximum Doppler difference frequency requirement.

In addition to the variable phase shift with time, the amplitude varies with time and also with position because of the shape of the scattering volume. This further contributes to the spectrum broadening.

PLASMA EFFECTS

A critical consideration is the cut-off frequency for propagation through a medium likely to be highly dispersive, because of the high temperatures in the combustion products, and the resulting ionization, as well as the solid constituents in the medium, such as dust and unburned cordite particles.

A. Shock Wave Phenomena

1. Simple Shocks - Relatively high gas temperatures and pressures may be achieved (simultaneously) with "simple gas shocks", or in "blast waves". In a shock, the motions are so rapid that very little momentum or energy is transported across the flow lines. A shock front is rather thin. In the shock the speed of sound is greater at the density maximum than at the plateaus on either side of the shock wave, consequently the shock wave gets steeper and steeper as the maximum catches up with its own base. This rapid increase in pressure poses a serious problem in designing radiating structures (antennas or radomes) for a microwave velocity measurement system.

From considerations of conservation of mass, conservation of momentum, and conservation of energy, the physical relations connecting the media across the shock can be deduced. The resulting equations are known as the HUGONIOT relations.

2. Shock Waves - The motion of a disturbance relative to a fluid is known as "wave motion", and the speed of propagation is the "wave speed". Consider one-dimensional motion, that is, the case of plane waves. A shock wave propagating into a stationary fluid sets the fluid into motion and raises its pressure, temperature and density. The "ideal" gas "jump" (shock wave) conditions can be related by:

$$\frac{\rho_2}{\rho_1} = \frac{U_1}{U_2} = \frac{(\gamma + 1) M_1^2}{(\gamma - 1) M_1^2 + 2} \quad \text{Density-Velocity}$$

$$\frac{P_2}{P_1} = \frac{2\gamma M_1^2 - \gamma + 1}{\gamma + 1} \quad \text{Pressure}$$

$$\frac{T_2}{T_1} = \frac{[2\gamma M_1^2 - \gamma + 1][(\gamma - 1)M_1^2 + 2]}{(\gamma + 1)^2 M_1^2} \quad \text{Temperature}$$

where 1, 2 denote physical quantities in front of and behind the shock, respectively; M_1 = Mach number in region 1, equal to $\frac{U_1}{c_{s1}}$ and $c_s^2 = \frac{\gamma T}{\rho}$. γ is the ratio of specific heats: $\gamma = \frac{c_p}{c_v}$, the ratio of the specific heat at constant pressure to the specific heat at constant volume. γ is also equal to $\frac{f+2}{f}$, where f is the number of degrees of freedom for the fluid. The shock wave speed is denoted by c_s .

A "weak shock" is defined as one for which the normalized pressure jump is very small, that is:

$$\frac{\Delta P}{P_1} = \frac{P_2 - P_1}{P_1} \ll 1.0$$

A "very strong shock" is defined as one for which the pressure ratio P_2/P_1 is very large.

3. Strong Shock (Rankine-Hugoniot) Equations

For very strong shocks, $P_2/P_1 \gg 1$, then

$$\frac{\rho_2}{\rho_1} \rightarrow \frac{\gamma + 1}{\gamma - 1}$$

$$\frac{T_2}{T_1} \rightarrow \frac{\gamma - 1}{\gamma + 1} \frac{P_2}{P_1}$$

$$c_s \rightarrow a_1 \left(\frac{\gamma + 1}{2\gamma} \frac{P_2}{P_1} \right)^{1/2}$$

and $U_P \rightarrow a_1 \left(\frac{2}{\gamma(\gamma + 1)} \frac{P_2}{P_1} \right)^{1/2}$ where ρ_1 and ρ_2 are the mass

densities in front of and behind the shock, respectively; T_2 and T_1 are the temperatures; a_1 is the speed of sound in front of the shock, and c_s is the shock wave speed. Thus the Mach number of the shock is

$$M_1 = \frac{c_s}{a_1} \quad \text{where } a_1 = \sqrt{\left(\frac{dp}{d\rho}\right)_1}$$

The fluid velocity behind the shock is U_p . Based on data obtained to date from DABS experiments, the following values will be used:

$$c_s = 6000 \text{ ft/sec}$$

$$\frac{\rho_2}{\rho_1} \sim 5$$

$$P_2 \sim 600 \text{ psi}$$

$$T_2 \sim 2500^\circ\text{K}$$

Consider a gas with 3 degrees of freedom, i. e., $f = 3$, then

$$\gamma = \frac{f+2}{f} = \frac{5}{3}. \quad \text{From this}$$

$$\frac{\rho_2}{\rho_1} = \frac{\gamma+1}{\gamma-1} = \frac{5/3+1}{5/3-1} = 4.$$

Similarly for a gas with 4 degrees of freedom, $\frac{\rho_2}{\rho_1} = 5$.

Consider now the shock velocity ($c_s = 6000 \text{ ft/sec}$), the sound speed in front of the shock a_1 , and the associated mach number

$$M_1 = \frac{c_s}{a_1}$$

For $c_s = 6000 \text{ ft/sec}$, $a_1 = 1135 \text{ ft/sec}$ (standard temperature and pressure in air),

$$M_1 = \frac{6000}{1135} = 5.3$$

Next consider $P_2 = 600$ psi, $P_1 = 14.5$ psi, then

$$\frac{T_2}{T_1} = \frac{\gamma - 1}{\gamma + 1} \frac{P_2}{P_1} = \frac{\gamma - 1}{\gamma + 1} \left(\frac{600}{14.5} \right)$$

with

$$\gamma = 3/2, \quad \frac{T_2}{T_1} = \frac{3/2 - 1}{3/2 + 1} \left(\frac{600}{14.5} \right) = 8.28$$

If $T_1 = 300^\circ\text{K}$, then $T_2 \approx 2500^\circ\text{K}$. Thus we have an estimate of the temperature from which to compute the electron density. For $\gamma = 1.4$ (air) $T_2 \approx 2100^\circ\text{K}$, and for conservatism we will use 2500°K in subsequent calculations.

B. Electron Density and Plasma Frequency

The plasma frequency, ω_{pe} , due to free electron density in an ionized medium of electromagnetic wave propagation, represents a critical frequency below which incident E-M waves are reflected from the plasma. This frequency depends on the electron density, $n_e^{1/2}$. The relationship is

$$\omega_{pe} = \sqrt{\frac{n_e e^2}{m_e \epsilon_0}} \approx 56.4 n_e^{1/2} \text{ radians/sec (MKS)}$$

The plasma density results from the ionization of gas atoms or molecules as a result of the thermal condition (temperature) of the gas. In deriving an expression for the total number of ionized particles, the recombination of the positive ions with the electrons must be considered. When thermodynamic equilibrium exists, the number of new ions equals the number of recombinations. Using this condition, SAHA derived an equation giving the degree of ionization α in terms of the gas pressure P and the temperature T .

$$\frac{\alpha^2}{1 - \alpha^2} = \frac{2.4 \times 10^{-4}}{P} T^{2.5} \exp(-W_i/kT) \text{ where } P \text{ is in Torr}$$

(mmHg), W_i is the ionization energy in electron-volts, k is Boltzmann's constant in (ev)/°K. Having determined α , n_e may be determined. The equation is extremely sensitive to the value selected for W_i , which depends on the medium.

Let

$$W_i = 15 \text{ ev}, k = \frac{1.38 \times 10^{-23}}{1.602 \times 10^{-19}} = 8.614 \times 10^{-5} \text{ ev}$$

then for $T_2 = 2500^\circ\text{K}$, $\exp(-W_i/kT) = 5.6 \times 10^{-31}$.

If $W_i = 12 \text{ ev}$, $\exp(-W_i/kT) = 6.3 \times 10^{-25}$; or if $W_i = 13 \text{ ev}$, $\exp(-W_i/kT) = 6.1 \times 10^{-27}$.

It is apparent that the value of α is quite sensitive to the ionization potential, so an accurate value of W_i for the composite medium of air, and combustion products mixed with it, is needed.

If a value for W_i of 11 ev is chosen, and $\alpha^2 \ll 1$, the equation simplifies to

$$\alpha^2 = \frac{(2.4 \times 10^4)(2500)^{2.5}}{3.1 \times 10^4} (6.55 \times 10^{-23}) = 1.58 \times 10^{-14}$$

The density, with standard temperature and pressure, is 2.685×10^{25} molecules/m³, but at 600 psi, $\frac{P_2}{P_1} \gg 1$ and $\frac{\rho_2}{\rho_1} = \frac{2.4}{.4} = 6$. Thus the density is about 6 times as great. The ionized electron density is therefore

$$n_e = (2.685 \times 10^{25})(6)(1.25 \times 10^{-7}) = 2 \times 10^{19} \text{ electrons/m}^3$$

For this value of n_e , ω_{pe} is obtained as

$$\omega_{pe} = 56.4 n_e^{1/2} \text{ rad/sec} = 8.976 n_e^{1/2} \text{ Hz}$$

$$f_{pe} = 40.3 \text{ GHz}$$

For other values of W_i we obtain

$W_i(\text{ev})$	α^2	$n_e(/m^3)$	$f_{pe}(\text{GHz})$
10	1.65×10^{-12}	2.07×10^{20}	129
11	1.58×10^{-14}	2.02×10^{19}	40.4
12	1.52×10^{-16}	1.99×10^{18}	12.7
13	1.47×10^{-18}	1.74×10^{17}	3.74
14	1.41×10^{-20}	1.91×10^{16}	1.24
15	1.35×10^{-22}	1.87×10^{15}	0.38

If the ionization potential and the assumed temperature and pressure produce an electron density of $10^{18}/m^3$, then any frequency in X-band or above should propagate satisfactorily through the medium.

1. Plasma Conductivity (skin depth) - The relationship between the conductivity and the temperature (in the absence of an external magnetic field) is given by Spitzer's equation:

$$\sigma = 0.015 \frac{T^{3/2}}{Z \ln \Lambda} \text{ mho/m}$$

with T the electron temperature in $^{\circ}\text{K}$, Z the effective ionic charge, and Λ is given by

$$\Lambda = \frac{12 \pi (\epsilon_0 k T / e^2)^{3/2}}{n_e^{1/2}}$$

where ϵ_0 is free space permittivity, e is electronic charge, n_e is number density of electrons. Thus σ depends on temperature and electron density. For the numbers used previously, i. e. $T = 2500^{\circ}\text{K}$, and selecting n_e as $10^{12}/\text{cm}^3$, we obtain:

$$\Lambda = 4.9 \times 10^{14} \frac{T_e^{3/2}}{n_e^{1/2}}, \text{ with } T_e \text{ in kev and } n_e/m^3$$

For $T = 2500^\circ\text{K} = \frac{2500}{11,600} \text{ ev} = .215 \times 10^{-3} \text{ kev}$

$$\Lambda = (4.9 \times 10^{14}) \frac{(.215 \times 10^{-3})^{3/2}}{(10^{12})^{1/2}} = 1544$$

$$\ln \Lambda = 7.342$$

In these units (kev and cm),

$$\sigma = \frac{T_e^{3/2}}{(4.8 \times 10^{-7}) \ln \Lambda} = \frac{(.215 \times 10^{-3})^{3/2}}{(4.8 \times 10^{-7})(7.34)} = .895 \text{ mho/cm}$$

$$\sigma = 89.5 \text{ mho/m}$$

Recalling conductivity values for good conductors:

<u>Medium</u>	<u>mhos/m</u>
Sea water	3-5
This plasma	89.5
Aluminum	3.54×10^7
Copper	5.8×10^7

It is apparent that the plasma is a fairly poor conductor, but still dispersive.

2. Plasma Skin Depth - The skin depth δ is calculated from the conductivity--assumed to be 90 mhos/m, and is based on the following equation.

$$\delta = (\pi f \mu \sigma)^{-1/2}$$

where f is the frequency of the E-M wave, μ is the permeability (assumed same as air) and σ the conductivity. For a frequency of 10.525 GHz

$$\begin{aligned} \delta &= [(\pi)(10.525 \times 10^9)(4\pi \times 10^{-7})(89)]^{-1/2} \\ &= 5.2 \times 10^{-4} \text{ m or approximately } 1/2 \text{ mm.} \end{aligned}$$

This indicates that the E-M wave is absorbed/reflected by the relatively good conductors in the hottest part of the plasma.

EM WAVE SCATTERING

The various types of scattering to be considered (since scattered energy must be detected to obtain the velocity shifted Doppler frequency) are:

Scattering by electrons

Scattering by conducting and by dielectric spheres

Scattering by "particles".

A. Scattering by Electrons (Thomson scattering; Thomson cross-section)

If a plane wave of monochromatic E-M radiation is incident on a free particle of charge e and mass m_e (e.g., an electron), the particle will be accelerated and emit radiation. The emitted radiation will be in directions other than that of the incident plane E-M wave. This process may be described as "scattering" of the incident E-M wave. The Thomson cross-section, σ_e , is given by⁵

$$\sigma_e = \frac{\mu e^2}{4\pi m_e} (\sin \psi)^2$$

in MKS units for a single electron, with ψ the angle between the direction of polarization of the incident field and the direction of the scatterer to the receiver. This reduces to

$$\sigma_{eT} = 8 \times 10^{-30} \sin^2 \psi n_e$$

and for the case in question, assuming a cubic scattering volume of 10 cm on a side, we obtain a maximum value ($\psi = 90^\circ$) at 10.4 GHz.

$$\begin{aligned}\sigma_{eT} &= (8 \times 10^{-30})(1.35 \times 10^{18})(10^{-3}) = 1.08 \times 10^{-11} \text{m}^2 \\ &= -110 \text{ dBm}^2, \text{ an undetectable cross-section.}\end{aligned}$$

B. Scattering by Conducting and by Dielectric Spheres

1. Dielectric Spheres - The medium within the tunnel after the shock front passes is known to be composed of the (partially ionized) ambient air, dust from the tunnel floor and roof, and combustion products. We will examine the backscattering potential of the dust particles and combustion particles in terms of scattering of an E-M wave. The instrumentation situation under discussion is a bistatic one,

with bistatic scattering angle $\theta/2$. A theorem due to Crispin, et al, states "In the limit of vanishing wavelength the bistatic cross-section for the transmitter direction \hat{k} and receiver direction \hat{n}_0 is equal to the monostatic cross-section for the transmitter-receiver direction $\hat{k} + \hat{n}_0$ with $\hat{k} \neq \hat{n}_0$ for bodies which are sufficiently smooth". \hat{k} is a unit vector from transmitter to target, \hat{n}_0 is a unit vector from receiver to target.

Thus, in our case, the monostatic cross-section should be close to the actual bistatic cross-section for individual particles (especially if the particles are spherical), since the bistatic angles will be less than 90° , and the wavelengths of interest are of centimeter dimensions.

In the Rayleigh region, a sphere of circumference small by comparison to the wavelength exhibits a cross-section varying as $1/\lambda^4$ where λ is the wavelength. Dust particles will be considered as dielectric spheres of various diameters uniformly distributed throughout the scattering volume but with random phase. The probability of the scattered signal amplitude x lying between x and $x + dx$ from the radar resolution cell is⁵

$$\rho(x) dx = \frac{2x}{P_0} \exp\left(-\frac{x^2}{P_0}\right) dx$$

where P_0 is the time average of x^2 . This is a Rayleigh distribution, with shape independent of the component amplitudes.

One of the properties of this distribution is that the rms amplitude of the fluctuations about the mean is proportional to the mean, i. e., the ratio of the standard deviation to the mean value is a constant. The above assumes that the incident wave is of constant power.

A potential difficulty in obtaining adequate performance from the system lies in the unwanted fluctuations in four-dimensional probability space. These are the marginal density functions of the two transmitted beams and that of the receive beam because of fluctuations in the medium within the experimental space, and the marginal density of the volumetric radar cross-section, discussed above. If a Rayleigh distribution describes each of these phenomena, which are not independent, then a four-dimensional probability space must be examined in detail to determine the constitutive parameters of the medium required to minimize unwanted signal fluctuations. These could effect.vely mask the desired fluctuations resulting from a single particle passing through clearly defined interference fringe planes.

It is apparent that the scale of the distribution of cross-section in the measurement space must exceed the spacing between the fringes. If scattering centers are uniformly distributed across the measurement volume there will be no discernible signal variation proportional to velocity. Similarly, if the phase velocity of the transmitted beams varies, the fringe positions will vary, and erroneous outputs will result. Finally, if the receiver amplitude fluctuates because of fluctuating attenuation over the propagation path, an erroneous output will result. Essentially the standard deviation to mean ratio must be as small for all four signal modifiers.

2. Cross-Section of Dielectric Spheres - In the Rayleigh region the radar cross-section of a small dielectric sphere of diameter D is:

$$\sigma_i = \frac{\pi^5 D^6}{\lambda^4} |K|^2$$

where K depends on the dielectric constant.

$K = (m^2 - 1)/(m^2 + 1)$, and m is the index of refraction. If we assume sandy dry soil, the dielectric constant is 2.55 at X-band frequencies, with a very small dissipation factor which will be ignored. Then

$$|K| = \frac{1.55}{3.55} = .437 \text{ and, for } f = 10.525 \text{ GHz}$$

$$\sigma_i = \frac{(.437)^2 \pi^5 D^6}{(.0285)^4} = (8.86 \times 10^7) D^6$$

In DABS experiment 1-D, a debris collector collected 36.78 g of material. Table B1 is reproduced from Ref. 6.

TABLE B1
DEBRIS TOTAL WEIGHT 36.78 (g)

<u>Diameter (in.)</u>	<u>D(m)</u>	<u>Mass(g)</u>	<u>Percent of Total</u>
Greater than .0331	84074 X 10 ⁻⁸	9.2	25
Greater than .0165	41910 X 10 ⁻⁸	9.3	25.3
Greater than .0098	24892 X 10 ⁻⁸	7.0	19
Greater than .0058	14732 X 10 ⁻⁸	5.8	15.8
Greater than .0029	7366 X 10 ⁻⁸	2.0	5.4
Less than .0029		<u>3.5</u>	<u>9.5</u>
		36.8	100

Since about half the particles are greater than .0165 in. in diameter and the cross section varies as D^6 , we will calculate the effective cross-section on the basis of the area density for these particles. The pipe collector diameter was 1.5 in., so for the largest particles the area density was 8070 g per m^2 . For the next largest it was 8157 g/ m^2 . Multiplying by the areas of the respective particle sizes we get 4.478×10^{-3} g/particle and 1.125×10^{-3} g/particle respectively. This leads to an estimate of 2.05×10^3 and 8.27×10^3 particles of the largest and next largest size. These particles were deposited over an interval of some 20 msec at an average velocity of 5000 fps, or an effective dimension of 100 ft, or 30.5 m. This, considering the area of the pipe, is a volume of .035 m^3 . The volume densities are then, respectively, $5.9 \times 10^4/m^3$ and $23.6 \times 10^4/m^3$.

In Ref. 6, the point is made that some of the particles are due to fallback. The authors assumed that the largest particles are due to fallback. For the sake of conservatism, this same assumption will be made for this analysis, and a particle density of $236 \times 10^3/m^3$ will be used, with a particle D of 41910×10^{-8} m.

$$\sigma_1 = (8.86 \times 10^7)(4.191 \times 10^{-4})^6 = 4.8 \times 10^{-13} m^2$$

Assuming a scattering volume defined by a 1.5° circular beam and 1 μ sec pulsewidth at a range of 2 km, we get $V_{01} = \pi(26.2)^2(150) = 323477 m^3$. These were the parameters of the measurement performed in Ref. 7, which obtained a measured cross-section of .8 m^2 on a dust cloud. This results in a σ_V volume reflectivity of $247 \times 10^{-8} m^2/m^3$.

Using the particle density for the DABS experiment data we obtain a volume reflectivity σ_V of $\sigma_V = (236 \times 10^3)(4.8 \times 10^{-13})m^2/m^3$, or $\sigma_V = 11.34 \times 10^{-8}m^2/m^3$.

This is within one order of magnitude of the X-band measurement of Ref. 7.

3. Cross-Section of Conducting Spheres - If a system cannot be designed with adequate sensitivity for detecting scattering from dust particles, it may be possible to increase the scattering cross-section by "seeding" the medium with aluminum dust, constituting conducting spheres. The amount and size of the particles required will be determined at that time, in a similar manner as in 1 and 2 above.

C. Scattering by Particles

Since the particulate matter collected in the DABS experiment of Ref. 6 was all dust, it is presumed that high velocity products of the cordite explosive charge in particulate form are carried out of the tunnel with the blast front or behind it. These particles may increase the volume reflectivity just behind the blast front. Calculations of the radar cross-section due to this could be made from radar data available to DABS testing, provided the Doppler radar was first calibrated using a precision sphere. This has not been done to date. For the following analysis a value of $\sigma_V = 10^{-7} \text{ m}^2/\text{m}^3$ will be used.

BISTATIC RADAR EQUATION

The Radar Range Equation is given by

$$P_r = \frac{P_t G_t G_r \lambda^2 \sigma_V \cdot V}{(4\pi)^3 D_t^2 D_r^2 L_P(t) L_P(r) L_s}$$

The parameters are:

- P_r - received signal power (W)
- P_t - transmitted power (W)
- G_t - transmitting antenna gain in target volume direction
- G_r - receiving antenna gain in target volume direction
- V - scattering volume defined by antenna beams (m^3)
- D_t - transmitter to target volume range (m)
- D_r - receiver to target volume range (m)
- $L_P(t)$ - propagation loss over transmitter-to-target path
- $L_P(r)$ - propagation loss over receiver-to-target path
- L_s - system losses

For the system described in II above, coherency is required between the two transmitted signals and this will be achieved by splitting the output of the RF generator and feeding separate antennas over identical wave guide paths. Thus the P_t term and the G_t term will include both transmitting beams. Similarly $L_P(t)$ will apply to both, on the assumption that the medium will be statistically homogeneous and isotropic for the geometry selected. These loss terms $L_P(t)$ and $L_P(r)$ will include radome losses. The selection of a radome material will be covered subsequently.

Selection of range to the scattering volume V will be determined by its dimensions, antenna apertures and far-field requirements. These in turn will dictate P_t to achieve a P_r at least 6 dB above the system noise. Each parameter will be examined in turn, for each of two systems, one operating in the X-band at a frequency of 10.525 GHz, and one at 16 GHz.

A. X-Band System Design Parameters

A required scattering volume of a 10 cm cube has been defined. This will affect the beamwidth and the far field requirements which will be addressed initially. The tunnel is assumed to be 7.2 ft across, or 2.2 m. If the intersection angle of the two transmit beams is θ , referring to Fig. B1, we will choose $\theta = 120^\circ$. Then with $W = 2.2$ m and beam crossing at $D_r = 1.1$ m, the separation between the two transmit antennas is $2s = 3.81$ m, and $D_t = 2.2$ m. A half power beamwidth of $\frac{\lambda}{D}$ radians for a uniformly illuminated aperture D in the far field (at $D_t = \frac{2D^2}{\lambda}$) would require $D = \frac{2.2}{.1} \lambda = 22\lambda$ or .627 m. But this would mean that the far field criterion could not be met, since $\frac{2D^2}{\lambda}$ for $D = .627$ is 27.6 m. We are thus constrained to a near field analysis of the situation, since the receive range to the scattering volume is one half the transmit range.

For a typical antenna with gain G_t , the power density W_t at a distance R in the far field is given by

$$W_t = \frac{P_t G_t}{4\pi R^2}$$

The half power beamwidth in degrees is given by $69 \frac{\lambda}{D}$ when a cosine illumination function is employed. Assuming this in each dimension, the gain is given by $27000 / (69\lambda/D)^2$.

$$\text{Therefore } G_t = \frac{(27 \times 10^3)(.627)^2}{(69)^2(.0285)^2} = 274$$

and

$$W_t = \frac{P_t(274)}{(4\pi)R^2}$$

If we let $R = \frac{2D^2}{\lambda} = 27.6$ m, then $W_t = .0286 P_t$

From Ref. 9, curve No. 34 (power density in the near field normalized to unity at $2D^2/\lambda$, when the normalized range $R_N = \frac{D_t}{2D^2/\lambda} = \frac{2.2}{27.6} =$

.0797, the power density increases by 12 dB, or 15.85 times. Therefore $W_t = .453 P_t$ in W/m^2 .

If now we consider the scattering cross-section as that due to the scattering volume common to two pencil beams of 10 cm diameter, resulting from focusing the antenna radiation at the desired range, a common volume such as indicated in Fig. B5 results. An approximation which may be used for the volume is the area of the parallelogram times the width of the half power beam, which is a volume of .001 m³.

Multiplying this times the particle volume density and the individual particle cross-section we obtain a scattering cross-section

$$V \sigma_V = (.001)(11.34 \times 10^{-8}) = 11.34 \times 10^{-11} \text{m}^2$$

The power which is isotropically scattered is then

$$W_t V \sigma_V = 5.14 \times 10^{-11} P_t \text{ in watts}$$

At a range R the scattered power density W_r is

$$W_r = \frac{5.14 \times 10^{-11} P_t}{4 \pi R^2}$$

If the range is $D_r = 1.1 \text{ m}$, we have

$$W_r = \frac{5.14 \times 10^{-11} P_t}{4 \pi (1.1)^2} = .338 \times 10^{-11} P_t$$

If the receiving aperture is made to match the scattering volume dimensions, a sectoral horn of width 20 cm and height 10 cm is indicated. Using this aperture with an effectiveness ratio of 90% we obtain

$$\begin{aligned} P_r &= W_r A_e = (.338 \times 10^{-11} P_t)(.02)(.9) \\ &= 6.08 \times 10^{-14} P_t \end{aligned}$$

The loss over the propagation paths is given by

$$L_P(t) (\text{dB/m}) = 4.34 \times 10^{-4} \left[\frac{\pi^2}{\lambda} (\sum_i D^3) I_m(-K) \right]$$

where the summation is over a 1m³ volume, D is particle diameter in centimeters, λ is in centimeters, $I_m(-K)$ is the imaginary part of -K,

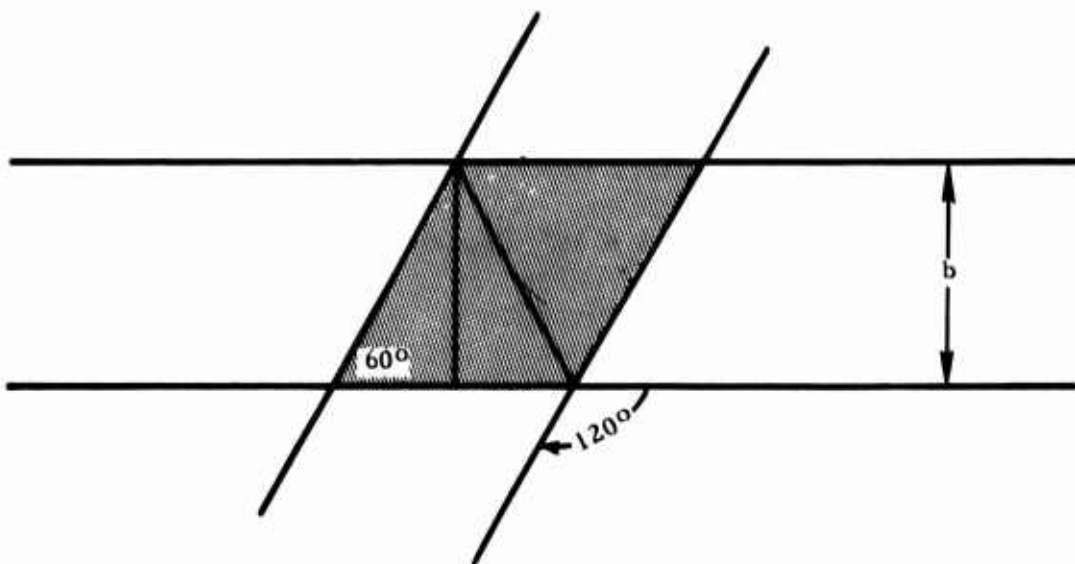
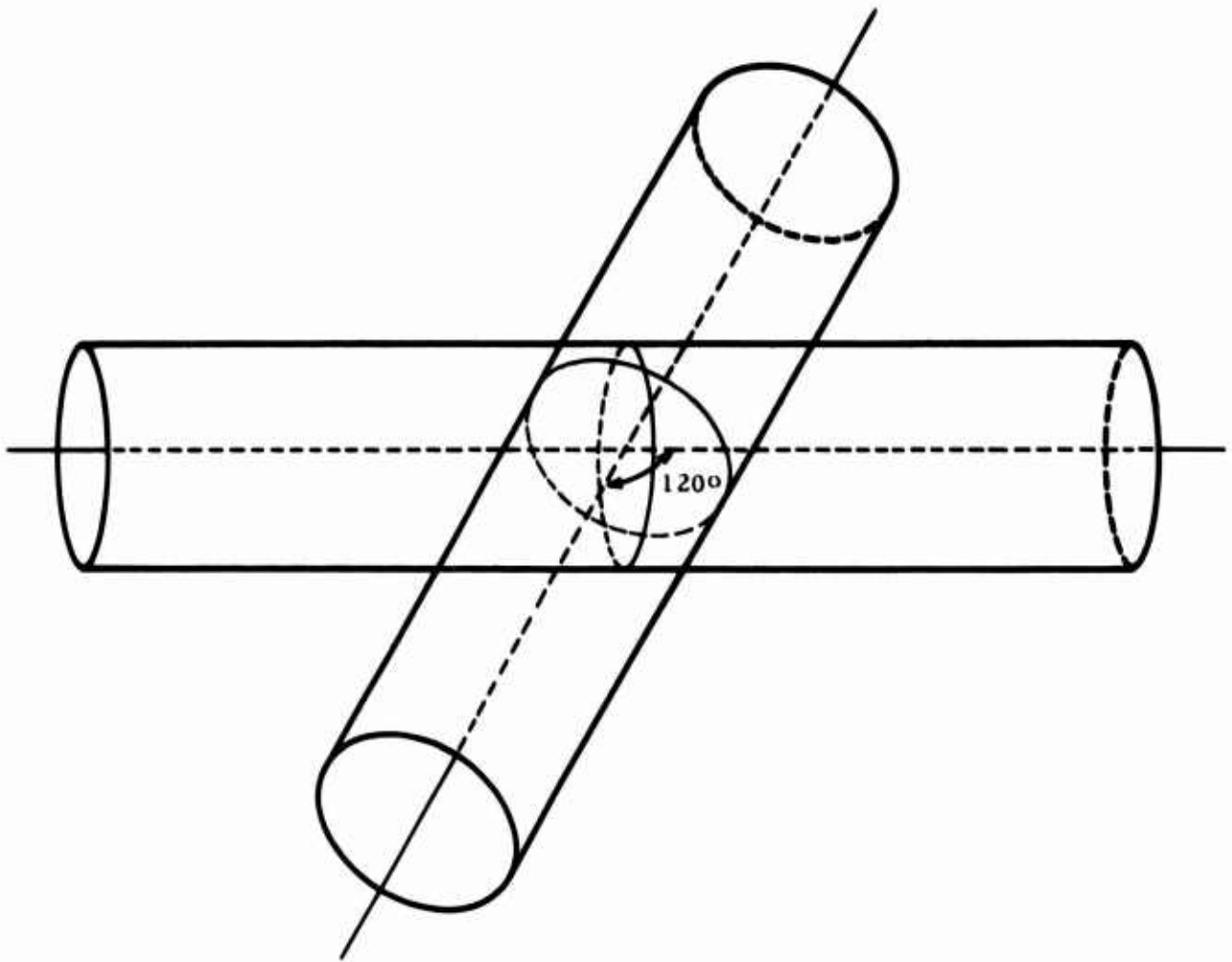


Figure B5. Scattering Volume Assumptions

and K depends on the dielectric constant of the particles as described in IVB2 above. For the dust we can assume the conductivity $\sigma_c = .0006$ mho/m. Then

$$m^2 = 2.55 - j \frac{.0006(36\pi \times 10^9)}{(2\pi)(10.525 \times 10^9)} = 2.55 - j 103 \times 10^{-5}$$

$$K = \frac{m^2 - 1}{m^2 + 1} = \frac{1.55 - j(103 \times 10^{-5})}{3.55 - j(103 \times 10^{-5})}$$

$$K = .676 - j(2.53 \times 10^{-4}) L_m(-K) = 2.53 \times 10^{-4}$$

For the two largest sized particles:

$$\begin{aligned} L_P(t) &= (4.34 \times 10^{-4}) \frac{2}{2.85} (2.53 \times 10^{-4}) [(5.9 \times 10^4)(8.4 \times 10^{-8}) \\ &\quad + (23.6 \times 10^4)(4.2 \times 10^{-8})] \\ &= 5.66 \times 10^{-9} \text{ dB/m} \end{aligned}$$

which can be neglected, as can $L_P(r)$. L_s , or system losses, will be estimated at 2 dB.

$\underline{P_r}$ - A signal to noise ratio of 10 dB as a minimum will be desired for the system. This means that

$$P_r = 10 K T_o B_n F_n$$

We will assume a noise figure F_n of 12 dB (15.84); $T_o = 3000^\circ\text{K} + 100^\circ\text{K} + 4303^\circ\text{K}$, and $B_n = 120$ kHz. The selection of B_n is based on

$$f_d = \frac{2V_r \sin(\theta/2)}{\lambda} = \frac{2(1828.8) \sin 60^\circ}{.0285} = 111 \text{ kHz.}$$

From this $KTB = (1.38 \times 10^{-23})(7403.6)(12 \times 10^4) = 1.22 \times 10^{-14}$ W and $P_r = 1.22 \times 10^{-13}$ W = -129 dBW with 10 dB signal to noise (S/N) ratio.

P_t - We can now find the required transmitter power, knowing the required receive power. Listing the values of the parameters as obtained previously we have:

		<u>X-Band</u>	<u>Ku-Band (Sec. C following)</u>
P_r	$1.22 \times 10^{-13} \text{ W}$	-129 dBW	-130 dBW
G_t	274	24 dB	31 dB
G_r	278	24 dB	31 dB
λ^2	$(.0285)^2 \text{ m}^2$	-30.9 dBm ²	-34.7 dBm ²
σ_v	$11.34 \times 10^{-8} \text{ m}^2/\text{m}^3$	-69.5 dBm	-61.9 dBm
V	.001 m ³	-30 dBm ³	-30 dBm ³
D_t^2	$(2.2)^2 \text{ m}^2$	6.8 dBm ²	2.1 dBm ²
D_r^2	$(1.1)^2 \text{ m}^2$.8 dBm ²	.8 dBm ²
L_s	1.58	2 dB	2 dB
$(4\pi)^3$	1984.4	33 dB	33 dB

To find the required transmitter power it only remains to set the two expressions for received power equal, and add 2 dB for system loss to the result.

$$6.08 \times 10^{-14} P_t = 1.22 \times 10^{-13}$$

$$P_t = 2 \text{ W}$$

After allowing for 2 dB of wave guide and radome loss, 3 W of average power appears to be adequate for the job.

B. Proposed X-Band Measurement System

A principal consideration of the system is its mechanical layout and installation. It must be protected from the effects of the explosion, and it must be isolated from vibration and mechanical shock effects, while still being rigidly interconnected by wave guide. One approach could be to build the system on a wooden pallet which can be installed in an accessible cavity beneath the tunnel floor. Figure B6 illustrates the location and mechanical layout. The microwave equipment could be rigidly mounted to a 3/4 in. plywood pallet, which could be installed on a vibration isolating base 14 ft X 3 ft and 12 in. thick. An excavation in the shock tunnel floor would be prepared into which the pallet could be placed with provision for 120 V 60 Hz power input and signal cable output. The system would then be covered with a reinforced and braced 1/2 in. steel plate into which might be mounted the slip-cast, fused-silica radomes.

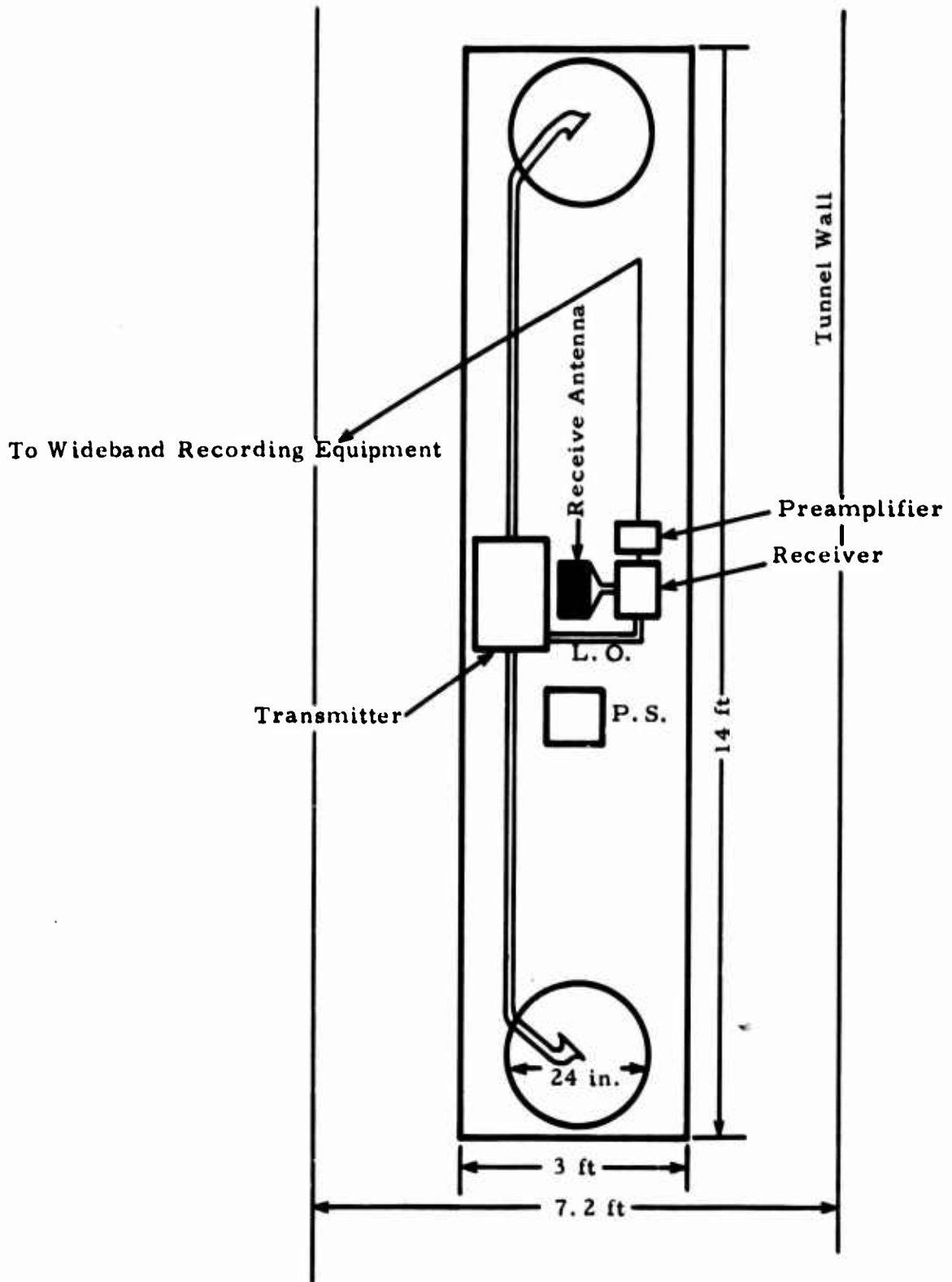


Figure B6. Microwave Velocimeter, Tunnel Floor Installation Layout, Typical for 120° Beam Intersection at 10.525 GHz

Preamplifier ARL Designed and Built \$ 500.00
 Bandwidth 0-185 kHz
 Gain 40 dB NF 10 dB

High Gain Low Noise Amplifier \$ 600.00
 80 dB Gain NF 10 dB 300 MHz B.W.

An alternative transmitter source is a Varian two-cavity klystron which produces 5 W of CW power. Price is \$2420. This would require a klystron power supply, at an estimated cost of \$4000.

Wave Guide Connectors, Wave Guide

Flanges, Miscellaneous Hardware	\$ 950.00
Radomes (3 each slipcast fused silica) Total	\$ 4,100.00
3 dB Power Divider (4 port power splitter) Ku-600	\$ 495.00
30 dB directional coupler 559-30	\$ 525.00
Components and Parts (using solid state source)	\$12,360.00

A block diagram of such a system is presented in Fig.B7. The angle between the transmitters is reduced to 60°, with the range to the scattering volume maintained at 1.1 m.

3. Design Analysis - Based on a wavelength of $\lambda = 1.85$ cm the various bistatic radar parameters for the recommended system are determined as follows:

$$\sigma_i = 4.8 \times 10^{-13} \left(\frac{2.85}{1.85} \right)^4 = 2.7 \times 10^{-12} \text{m}^2$$

$$\sigma_V = (11.34 \times 10^{-8})(5.632) = 6.39 \times 10^{-7} \text{m}^2/\text{m}^3$$

$$= -61.9 \text{ dB}$$

$$D_r \quad 1.1 \text{ m} \quad D_r^2 = .8 \text{ dBm}^2$$

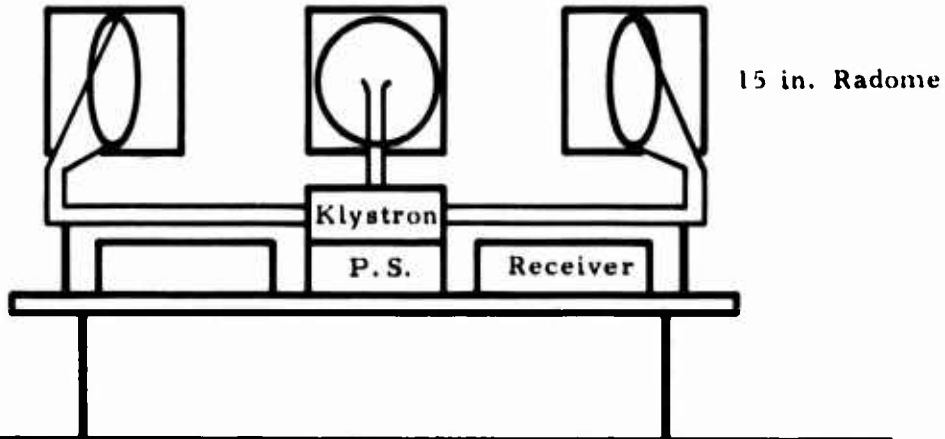
$$D_t \quad 1.27 \text{ m} \quad D_t^2 = 2.1 \text{ dBm}^2$$

At a range of 1.27 m the 4.7° HPBW of the selected antennas subtends 10 cm. This results in an effective scattering volume of approximately 10^{-3}m^3 , or -30 dB.

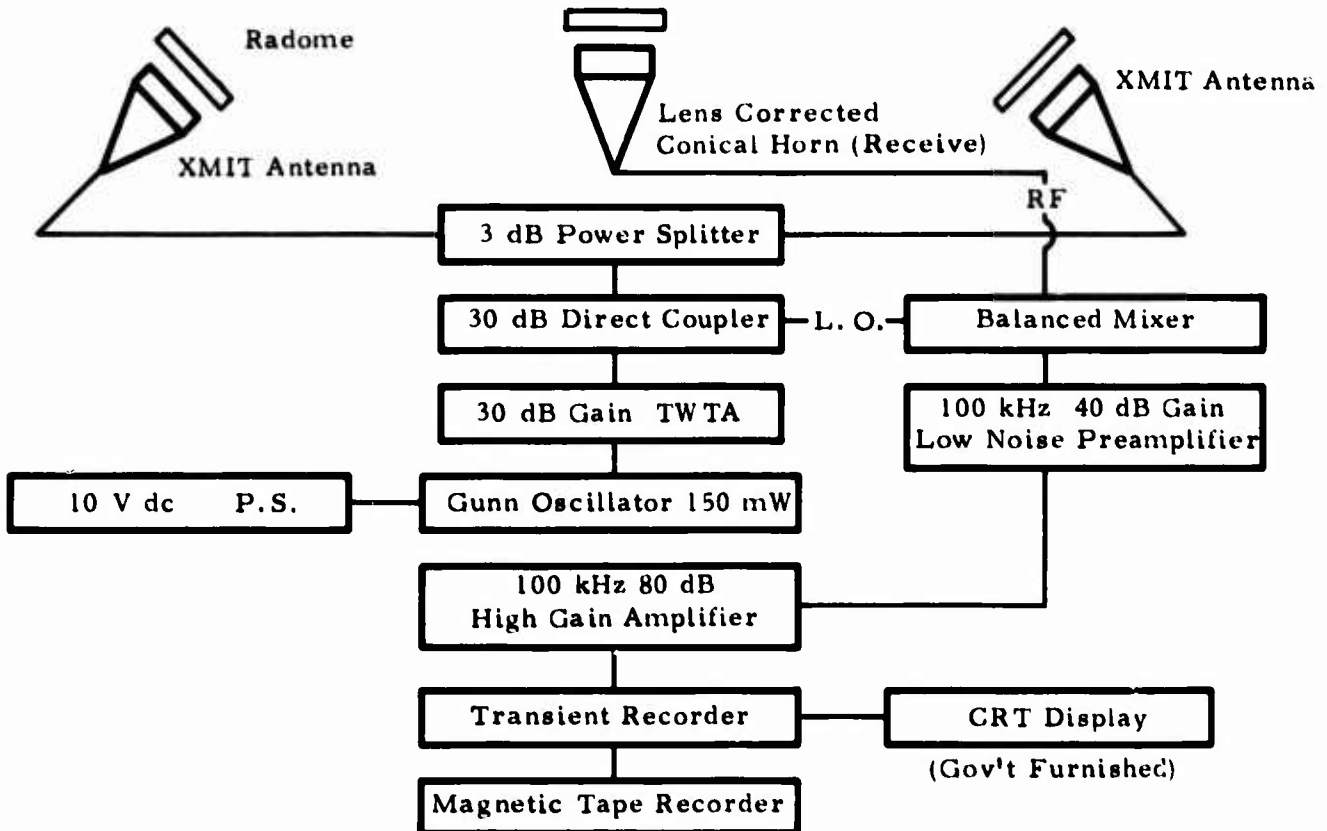
$$G_t \quad 31 \text{ dB}$$

$$G_r \quad 31 \text{ dB}$$

Roof of Tunnel



a. Mechanical Layout



b. System Block Diagram

Figure B7. Ku-Band System Design

$L_p(t)$ $L_p(r)$ These losses are negligible in the medium. The slip-cast, fused silica radomes are 15 in. square milled material (available from Brunswick Corp., Marion, VA) 7 wavelengths in thickness, or about 2.9 in. in thickness. The loss tangent for this material is given as .003 and the dielectric constant is 3.2. The thickness is given by

$$d = \frac{n\lambda}{2(\epsilon_r - \sin^2\theta)^{1/2}}$$

where θ is measured from the normal to the radome surface. If θ is 0° and $d = 7.24$ cm then

$$n = \frac{(7.24)(2)(3.2)^{1/2}}{1.85} = 14$$

The tensile strength is given as 4000 - 5000 psi with flex strength of 4500 psi and modulus of elasticity of 3.5×10^6 . The material porosity can be reduced by impregnating with silicone resin which reduces its susceptibility to moisture, grease, and other contaminants. From Ref. 10, a formula for reflection coefficient ρ is given as

$$\rho = \frac{r[1 - \exp(-2\phi L_0 - 2_j\phi)]}{1 - r^2 \exp(-2\phi L_0 - 2_j\phi)}$$

$$\phi = \frac{2\pi d}{\lambda} \left(\frac{\epsilon}{\epsilon_0} - \sin^2\theta \right)^{1/2} \text{ and } \theta = \text{incidence angle measured from normal.}$$

$$\text{If } \frac{d}{\lambda} = 7, \text{ and } \theta = 30^\circ \phi = 14\pi(3.2 - .25)^{1/2} = 75.54 \text{ radians}$$

L_0 is the attenuation due to conductive losses

$$L_0 = \frac{\epsilon_r \tan \delta}{2(\epsilon_r - \sin^2\theta)} = \frac{(3.2)(.003)}{2(3.2 - .25)} = 16.2 \times 10^{-4}$$

r is the interface reflection coefficient given by

$$r = \frac{1 - \sqrt{\epsilon_0} + j L_1}{1 + \sqrt{\epsilon_0} - j L_1}$$

and $\epsilon_e = \frac{\epsilon_r - \sin^2 \theta}{\cos^2 \theta} = 3.93$ for vertical (perpendicular) polarization.

L_1 is the reactance due to conductive loss:

$$L_1 = \frac{\epsilon_r \tan \delta}{2 \cos \theta [\epsilon_r - \sin^2 \theta]^{1/2}} = \frac{.0096}{2.974} = 3.2 \times 10^{-3}$$

$$r = \frac{1 - \sqrt{3.93 + j(3.2 \times 10^{-3})}}{1 + \sqrt{3.93 - j(3.2 \times 10^{-3})}} = \frac{-.98 + j(3.2 \times 10^{-3})}{2.98 - j(3.2 \times 10^{-3})}$$

$$r = -.33$$

Then

$$\rho = \frac{-.33[1 - e^{-2(43.17)(16.2 \times 10^{-4})}]_j}{1 - (-.33)^2 e^{-2(43.17)(16.2 \times 10^{-4})} \cdot e^{-2j(75.54)}} = -.054 - j .067$$

$$|\rho|^2 = .0069$$

The transmission at this angle is then 99% and losses can be considered negligible for both $L_p(t)$ and $L_p(r)$. The radome size selection was based on radome installation parallel to the antenna aperture. If the radomes are installed normal to the direction of propagation no losses would result. A loss of .25 dB will be estimated for $L_p(t)$ and $L_p(r)$.

L_g will be estimated at 2 dB

$$P_t = 5 \text{ W} = 7 \text{ dBW}$$

$$\lambda = 1.85 \text{ cm} \quad \lambda^2 = -34.7 \text{ dBm}^2$$

Finally we obtain in dBW:

$$P_r = 7 + 31 + 31 + (-34.7) + (-61.9) + (-30) - 33 - 2.1 - .8 - .25 - .25 - 2 = -96 \text{ dBW}$$

To calculate the S/N ratio we again need the effective bandwidth:

$$B_n = f_d = \frac{2(1828.8)\sin 30^\circ}{.0185} = 98854 \approx 100 \text{ kHz}$$

The noise power then is $kTB = N_o$

$$N_o = (1.38 \times 10^{-23})(7403.6)(10^5) = 1.02 \times 10^{-14}$$

$$N_o = -140 \text{ dBW}$$

The signal to noise ratio (S/N) is the ratio of P_r to N_o :

$S/N = -96 + 140 = 44 \text{ dB}$. In other words, there is a 34 dB advantage in S/N ratio, over the X-band design.

4. Mechanical Layout - The system will be installed on a pallet 6 ft long by 2 ft deep, so that it may be positioned adjacent to the tunnel wall with the conical horn antennas inserted into openings preformed in the cement wall at 1/2 the height of the tunnel.

5. System Engineering - In addition to the required components and parts, an estimated 12 man-months of system engineering, at a cost of \$42,000 would be required. The total estimated cost of the system is thus about \$54,360.

In the interest of cost effectiveness, it is suggested that the transmitter power may be adequate using a 150 mW solid state source. The estimated 30 dB excess S/N ratio could eliminate the requirement for the klystron source or for a TWT amplifier. The system could readily be modified to add the TWT amplifier, and in fact could be designed with the add in capability, should additional sensitivity be required. The cost of a klystron power supply, plus the klystron source, which is heavy and bulky, makes it a less attractive solution for the transmitter requirement.

6. Millimeter Wave System - At 96 GHz the wavelength is approximately one-sixth that at the selected Ku-band frequency. The scattering cross-section would be improved, therefore, by 31 dB. This could make the system design at this wavelength more attractive, since the antenna gains might be 12 to 15 dB higher also. Unfortunately, a klystron and power supply would be required, costing about \$8500, just to get 250 mW of power. In addition, millimeter components are substantially more expensive. For example, a 30 dB directional coupler costs \$675, and a power divider costs \$625, and of course wave guide and other components would be somewhat higher.

REFERENCES

1. Baker, W. E., Explosions in Air, University of Texas Press, Austin, 1973.
2. Papas, C.H., Theory of Electromagnetic Wave Propagation, McGraw-Hill Book Company, 1965.
3. Shipp, J.I., R. H. Hines, W. A. Dunnill, Development of a Laser Velocimeter System, AEDC-TR-67-175, Arnold Engineering Development Center, Tullahoma, Tennessee, October 1967.
4. Bragton, D. B., and W. H. Goethert, New Velocity Measuring Technique Using Dual Scatter Laser Doppler Shift, AEDC-TR-70-205, Arnold Engineering Development Center, Tullahoma, Tennessee, November 1970.
5. Skolnik, Merrill I., Introduction to Radar Systems, McGraw-Hill Book Company, 1962.
6. Baum, N., and K. Simmons, University of New Mexico Memorandum, Subject: Debris Collection Experiment (Ref. T.D. 10.05), 2 July 1976.
7. Robbiani, R.L., Middle North Series, Mixed Company Event, Project LN107 POR 6616, Defense Nuclear Agency, 23 July 1973.
8. Kraus, John D., Antennas, McGraw-Hill Book Company, Inc., 1950.
9. Microwave Engineer's Handbook, Volume Two, Horizon House-Microwave, Inc., 1971.
10. Jaak, Henry, (ed.), Antenna Engineering Handbook, McGraw-Hill Book Company, 1961.

APPENDIX C
IMPLEMENTATION OF A BLAST-WAVE VELOCITY GAUGE
FOR THE DYNAMIC AIRBLAST SIMULATOR

	<u>Page</u>
Introduction	128
The Blast Gauge	128
Ray Tracing	130
Simplified Technique	133

INTRODUCTION

It has been proposed that a "blast gauge" be used to measure local gas velocity and speed of sound during tests of the Dynamic Air Blast Simulator. The principle of the device is to generate at some point in the simulator a pressure pulse whose amplitude is sufficiently large as to be distinguishable in the noisy, nonsteady signal generated by the primary blast wave, and to measure the velocity of propagation of this pulse between two relatively closely spaced detectors.

The theory for the propagation of a finite-amplitude pulse through a nonuniform, nonsteady flow field is very complicated. In order to make the blast gauge a feasible instrument, significant simplifications in the theory of its operation must be made. In this report we show what assumptions have to be made and point out some of the features of the technique.

THE BLAST GAUGE

Consider the configuration shown in figure C1 (for simplicity, a two dimensional picture is shown; the formulas can easily be generalized to three dimensions). A charge of high explosive is located at the origin and is immersed in the one-dimensional flow field $u(x, t)$ generated by the primary blast in the Air Blast Simulator. Three pressure transducers are located in an array at points (1), (2) and (3), point (1) being distant r from the charge.

At some time ($t=0$) after the passage of the primary shock the charge is detonated. The blast wave from this explosion propagates relative to the nonuniform, nonsteady moving fluid with velocity c . The wave interacts with the gradients in the fluid, and its strength (e.g., its Mach number $M=c/a$, where a is the local sound speed) changes, in the same manner as when a wave interacts with an area change. We are primarily interested in the velocity of the wave, and, if the wave is weak, the variation of M due to the interaction with nonuniformities is second order, so the effect on c is negligible. However, other causes of variation of the velocity c may be first order. For example, if the variation of wave

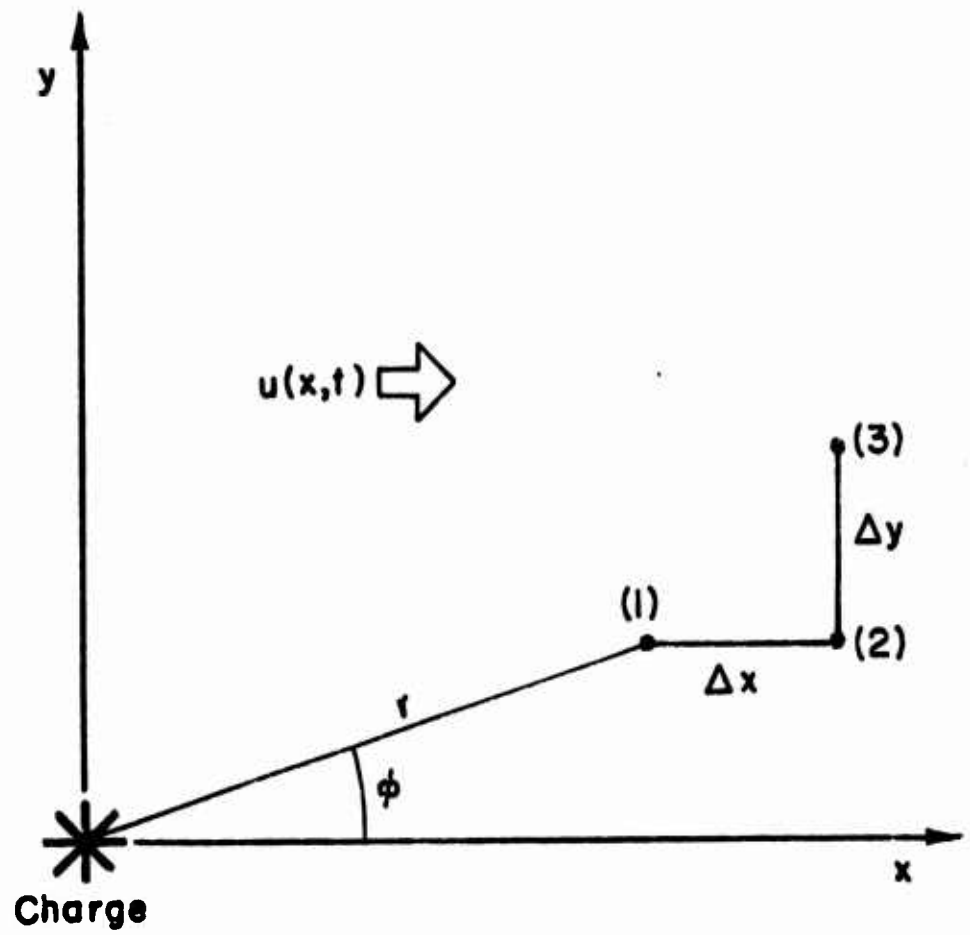


Figure C1. Geometry of Blast Gage

strength M along the path length $R(t)$ due to spherical spreading is known a priori, then $M(r)$ can be accounted for. Furthermore, in general the sound speed is variable, $a(x,t)$, and it may be necessary to account for this.

The geometry of shock wave propagation in multidimensional flows can most easily be studied according to the theory of nonlinear shock dynamics of Whitham. For weak shocks this reduces to the theory of nonlinear geometrical acoustics of J. B. Keller, which has been worked out in much greater detail. For waves of infinitesimal strength it is the familiar theory of geometrical acoustics. In all cases the wavefronts propagate along trajectories known as rays. In our problem (figure C2) the waves propagate relative to the fluid in a direction normal to the front with speed c and are convected along with the fluid velocity $u(x,t)$. The resultant wave speed \underline{v} is the vector sum of $c\underline{n}$ and \underline{u} , where \underline{n} is the unit vector normal to the wavefront. \underline{v} is tangent to the ray at the wavefront. Thus, in a moving fluid the rays are not normal to the wavefronts, and the wave speed is not c .

RAY TRACING

In nonuniform, nonsteady flow $u(x,t)$ and $a(x,t)$ are variable, and, if the wave strength is decaying, $M(r)$ is also variable, so in general the rays are curved. (Furthermore, nonlinear effects cause ray curvature, but we are neglecting them here.) Therefore, in order to determine what part of the wave front is being observed at any point in space and time it is necessary to trace rays by solving the vector equation for the ray trajectory

$$\frac{d\underline{r}}{dt} = \underline{v}, \quad (C1a)$$

or

$$\frac{dx}{dt} = v_x, \quad \frac{dy}{dt} = v_y, \quad (C1b)$$

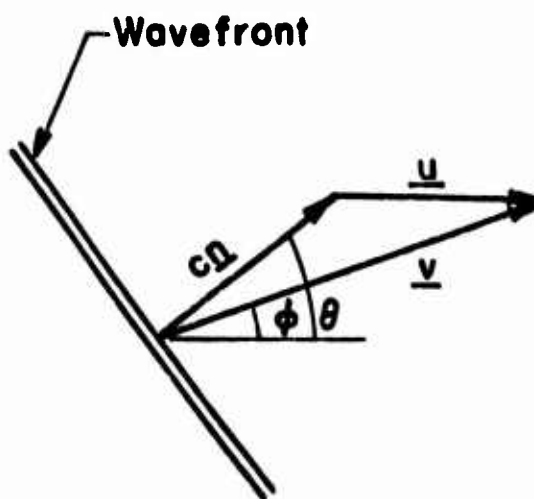


Figure C2. Propagation of Secondary Shock

where, from figure C2

$$v_x = M(R) a(x, t) \cos \theta + u(x, t), \quad (C2a)$$

$$v_y = M(R) a(x, t) \sin \theta \quad (C2b)$$

In C2 we have used $c = Ma$. θ is constant along a ray and is the label denoting the part of the wavefront that is being observed. Thus, the ray emanating from the explosion with angle θ can be constructed by integrating the equations

$$dx = [M(R(t)) a(x, t) \cos \theta + u(x, t)] dt \quad (C3a)$$

$$dy = M(R(t)) a(x, t) \sin \theta dt \quad (C3b)$$

to give the parametric representation $x(t; \theta)$, $y(t; \theta)$ for the ray. The path length $R(t)$ is evaluated from

$$R(t; \theta) = \int_0^t v(t; \theta) dt, \quad (C4)$$

where

$$v(t; \theta) = \left\{ \left[M(R(t)) a(x(t), t) \right]^2 + \left[u(x(t), t) \right]^2 + 2M(R(t)) a(x(t), t) U(x(t), t) \cos \theta \right\}^{\frac{1}{2}}, \quad (C5)$$

which is simply $v^2 = c^2 + u^2 + 2uc \cos \theta$, with the dependence on the independent variables written out explicitly. It is clear that, in the general case, C3 can be solved for the ray coordinates together with the integral equation C4 for the path length only by an approximate, iterative scheme, and this only under circumstances when good estimates of the entire flow field $u(x, t)$, $a(x, t)$ are available.

Equations C3 and C4 would in general be used with the blast gauge as follows: Using a preliminary estimate of the flow field, rays are traced from the explosion to the locations of the detectors and arrival times are thereby predicted. The predictions are compared with measurements, and any differences are used to correct the estimate of the flow field, presumably by some kind of optimal interpolation procedure. The process is repeated

until agreement is obtained. This is clearly a very complex and sophisticated process, particularly if several different detectors and several different explosions are used for the purpose of providing sufficient data to adequately define the flow field. Thus, in order that the blast gauge be an easily applied tool, it is essential that further simplifications be incorporated.

SIMPLIFIED TECHNIQUE

If the detectors are located close enough together that $\Delta x, \Delta y \ll L$, where L is some length scale of the flow field (given by the gradients behind the primary shock; e.g., of order of the driver length) and if $\Delta x, \Delta y \ll r$, then locally, in the triangle of the detectors the waves can be treated as being plane, the rays as straight and the flow as uniform and steady. In figure C3 the wave front is shown at three different times as it passes the three detectors. The time interval measured between the first pair of detectors is $t_2 - t_1 = \Delta t_1$ and between the second pair is $t_3 - t_2 = \Delta t_2$. The figure shows the distance traveled by the wave along the vector \underline{y} in these intervals. From the geometry shown in the figure (cf. dotted line), it follows that

$$\frac{(c + u \cos \theta) \Delta t_1}{\Delta x} = \cos \theta \quad (C6a)$$

$$\frac{(c + u \cos \theta) \Delta t_2}{\Delta y} = \sin \alpha \quad (C6b)$$

$$\alpha = \theta. \quad (C6c)$$

Therefore,

$$\tan \theta = \frac{\Delta x \Delta t_2}{\Delta y \Delta t_1} \quad (C7a)$$

$$c + u \cos \theta = \frac{\Delta x}{\Delta t_1} \cos \theta. \quad (C7b)$$

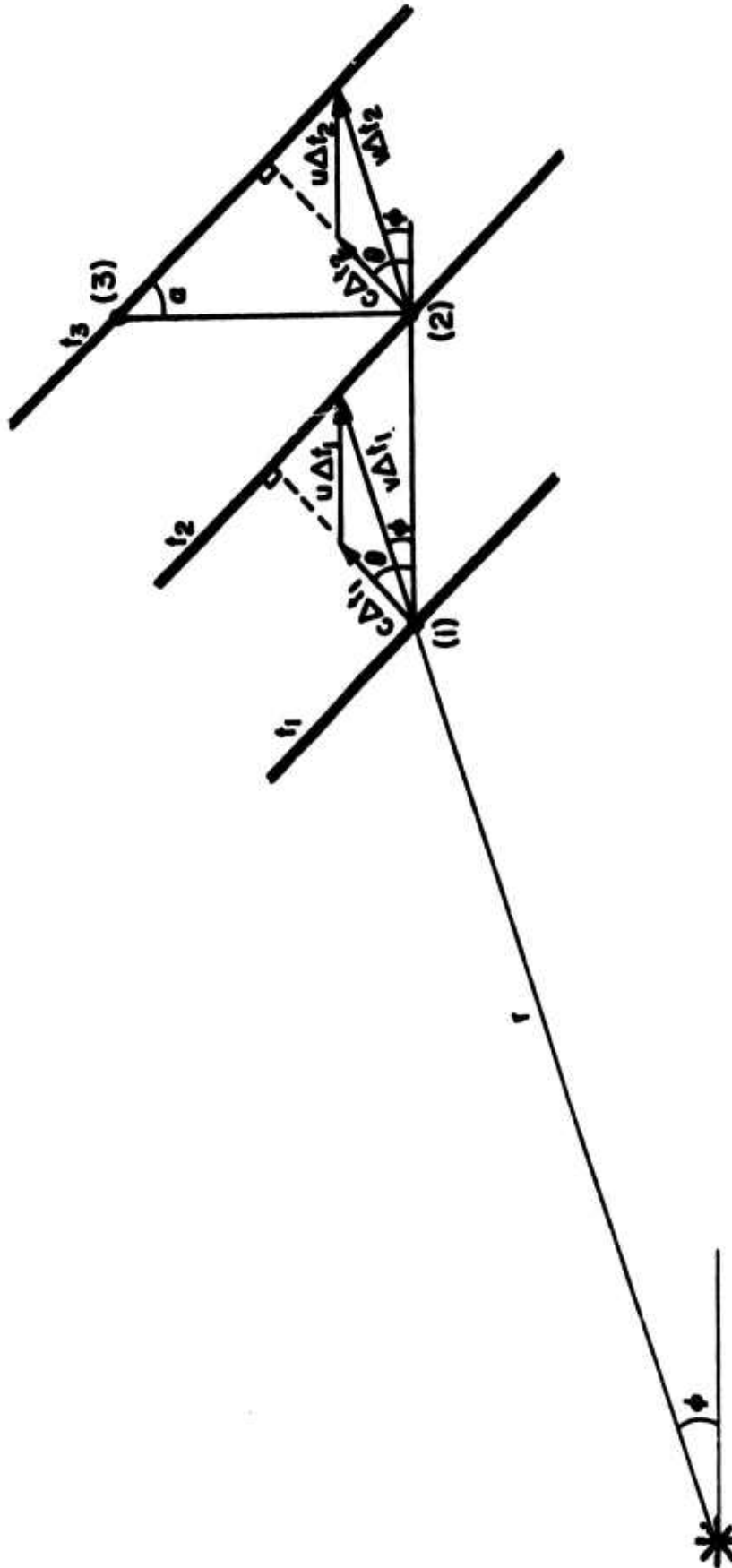


Figure C3. Propagation Direction of Secondary Shock

Equations C7 are the fundamental relations for the blast gauge. They show that:

1) It is necessary to have an array of three detectors as shown in order to determine both the angle θ and the velocities, and

2) It is necessary to observe two different waves (i.e., with 2 different angles θ_1, θ_2) in order to resolve separately the velocities u and c . That is, if two waves are observed, closely enough spaced in time that the flow field does not change significantly, then the two measurements yield, say,

$$c + u \cos \theta_1 = K_1 \quad (C8a)$$

$$c + u \cos \theta_2 = K_2, \quad (C8b)$$

so that

$$u = \frac{K_1 - K_2}{\cos \theta_1 - \cos \theta_2} \quad (C9a)$$

$$c = \frac{K_1 \cos \theta_2 - K_2 \cos \theta_1}{\cos \theta_2 - \cos \theta_1} \quad (C9b)$$

On the other hand, if it is known "where the wave came from" (i.e., the angle φ), then another relationship between c and u is available. φ is known if the ray r from the explosion to the detector array can be considered to be straight, i.e., if $r \ll L$. Therefore, providing

$$\Delta x, \Delta y \ll r \ll L \quad (C10)$$

c and u can be evaluated from one wave only. For, from figure C3

$$v \cos(\theta - \varphi) = c + u \cos \theta \quad (C11)$$

Expressing v in terms of c and u , and using C7b to evaluate the right-hand-side,

$$c^2 + u^2 + 2uc \cos \theta = \left[\frac{\Delta x}{\Delta t_1} \frac{\cos \theta}{\cos(\theta - \varphi)} \right]^2 \quad (C12)$$

C12 can be used together with equations C7 to evaluate c and u;

$$\tan \theta = \frac{\Delta x}{\Delta y} \frac{\Delta t_2}{\Delta t_1} \quad (C7a)$$

$$c = \frac{\Delta y}{\Delta t_2} \sin \theta \left[1 - \frac{\tan(\theta - \varphi)}{\tan \theta} \right] \quad (C13a)$$

$$u = \frac{\Delta y}{\Delta t_2} \tan(\theta - \varphi) \quad (C13b)$$

Note, however, that for $\theta = \varphi = 0$ the additional information is lost; that is, the array must not be directly downstream from the explosive source.

For "slight offset" ($\theta \ll 1$ or $\pi - \theta \ll 1$) simplified equations result. First consider downstream-propagating waves ($\theta \ll 1$). Then equation C11 becomes

$$\varphi \doteq \frac{c}{c+u} \theta \quad (C14)$$

and C7 become

$$\theta \doteq \frac{\Delta x}{\Delta y} \frac{\Delta t_2}{\Delta t_1} \quad (C15a)$$

$$c + u \doteq \frac{\Delta x}{\Delta t_1} \quad (C15b)$$

Thus, for a downstream wave with the gauge slightly offset, c and u can be evaluated independently;

$$c \doteq \varphi \frac{\Delta y}{\Delta t_2} \quad (C16a)$$

$$u \doteq \frac{\Delta x}{\Delta t_1} - \varphi \frac{\Delta y}{\Delta t_2} \quad (C16b)$$

On the other hand, for upstream propagating waves with slight offset ($\pi - \theta \ll 1$), C11 becomes

$$\varphi \doteq 2\theta - \pi \quad ; \quad c > u \quad (C17a)$$

$$\varphi \doteq 2(\theta - \pi) \quad ; \quad c < u . \quad (C17b)$$

That is, for $c > u$ φ must be almost π while for $c < u$ φ is almost zero, and to first order an additional relation between u and c is not obtained! In this case C7 become,

$$\theta = \pi + \frac{\Delta x}{\Delta y} \frac{\Delta t_2}{\Delta t_1} \quad (C18a)$$

$$c - u = -\frac{\Delta x}{\Delta t_1} \quad (C18b)$$

In summary, with a blast gauge satisfying the conditions C10 and with the array set downstream from the explosive source with slight offset, if the flow is locally supersonic ($c < u$), first the downstream propagating wave passes the array, yielding c and u according to C15, and then the upstream propagating wave passes, yielding θ by C17b or C18a, and $c-u$ by C18b. In subsonic flow ($c > u$) the same redundant information may be obtained with a blast gauge if an additional array of detectors is set upstream of the source.

It should be noted that if the time of ignition of the blast ($t=0$) relative to the time of arrival at point (1) (i.e., if the time t_1) is accurately known, if r is taken as Δx and if $M(R)$ is known all the way from the source, then the occurrence of the blast can be taken as one of the times of arrival, and the number of transducers required can be reduced by one.

**APPENDIX D
FEASIBILITY OF MAGNETIC VELOCITY
GAGE FOR DABS TESTS**

	<u>Page</u>
Background	140
Introduction To MHD Velocity Measurement	143
Experimental Results	152
Conclusions and Recommendations	169
References	175

1. BACKGROUND

Measurement of airblast flow velocity in a DABS test is essential for adequate definition of the flow environment, but there are difficult technical problems to overcome. The flow velocity is too high and the blast environment is too severe for conventional anemometers to work. Optical methods for measuring flow velocity are difficult to begin with, and are impractical or impossible when account is taken of smoky impurities in the explosive gases together with problems of optical alignment in an explosive field test. Doppler shift radar is a possibility, but depends on adequately launching lightweight reflecting materials in the airblast flow or utilizing interface conductance phenomena. Even if successful, the radar method only determines the velocity of a particular element of fluid, and does not yield directly the desired result of gas velocity history at a given test station.

On the other hand measurement of flow velocity in explosively driven plasma for MHD electric power applications is outstandingly simple, accurate, reliable, and compatible with field test conditions. Standard practice at Artec in these tests is to provide a magnetic field, either with a permanent magnet or an electromagnet, across the flowing gas, and pick up the Faraday generator voltage with simple electrodes fabricated from brass screws. The electrode

voltage, as measured directly across the electrodes through a long (100 ft) terminated cable, is directly proportional to the gas flow velocity. Knowing magnetic field strength the relationship between velocity and voltage is known absolutely, and there is no need for gage calibration.

The magnetic velocity gage is an outstanding candidate for DABS tests in terms of simplicity and practicability, but there are serious problems associated with low gas conductivity which must first be overcome. In explosive MHD experiments the gas conductivity is high, and the internal resistance of the Faraday generator is only a few milliohms. By contrast the theoretical equilibrium conductivity of seeded detonation products is so low that internal resistance is many megohms. Nonequilibrium effects in the expanding gas undoubtedly increase the conductivity, but the generator resistance is still so high that amplifiers with high input impedance are required. Measurement of generator voltage at high impedance levels introduces concerns with noise and static electricity that do not affect explosive MHD measurements.

The present program was initiated to evaluate the utility of the magnetic field gage in measuring dynamic flow environment in DABS tests. The program is divided into two phases: Phase I consists of gage design and preliminary evaluation tests conducted by Artec at a local test site,

and Phase II consists of evaluation of the gage in scheduled large scale DABS tests.

This report describes the results of Phase I tests to date. It is concluded that problems associated with high impedance measurements, stray capacitance, and charge accumulation effects preclude advancing to Phase II at this time. The data are not conclusive with respect to the feasibility of the concept, and there is a reasonable possibility that the measurement problems can be resolved with further Phase I effort.

2. INTRODUCTION TO MHD VELOCITY MEASUREMENT

2.1 Faraday Generator

Michael Faraday originally observed that a voltage is generated when a conductor moves through a magnetic field. Maximum voltage is obtained when the conductor motion, the magnetic field, and the pickup electrodes are perpendicular. When used as a velocity gage the Faraday generator consists of an electromagnet field coil (or permanent magnet) and a pair of electrodes as shown in Figure D1.

Open circuit voltage across the electrodes is

$$V = BuA, \quad (D1)$$

where B is the magnetic field in tesla (1 tesla = 10^4 gauss), u is the gas velocity in meters/sec, A is the interelectrode spacing in meters, and V is the open circuit voltage in volts. This equation relates the open circuit output voltage to the gas velocity in terms of two readily determined parameters B and A .

When the generator is attached to a load there is a voltage drop due to resistive losses in the gas. In that case the generator voltage is given by

$$V = BuA - RI \quad (D2)$$

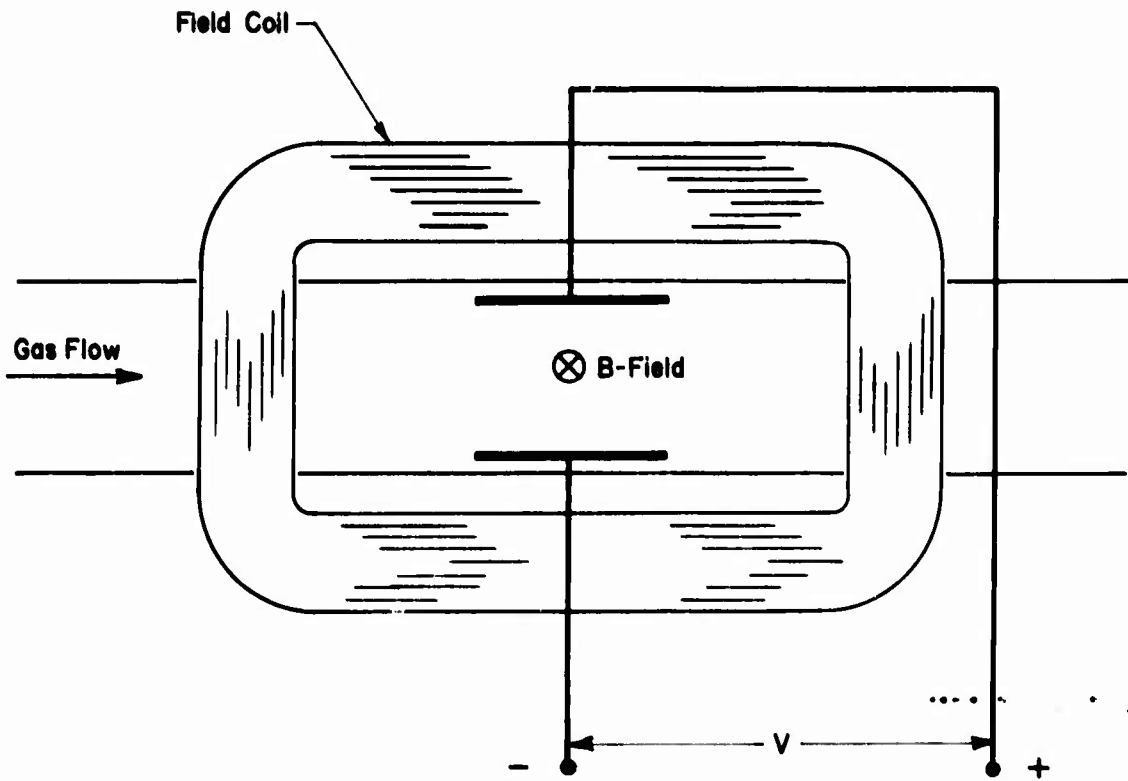


Figure D1. Schematic of Faraday Velocity Gage

The equivalent circuit of the Faraday generator consists of a voltage source in series with the internal gas resistance R .

Gas resistance is related to gas conductivity by the equation

$$R = k \frac{A}{\sigma A} \quad (D3)$$

where A is the interelectrode spacing in meters, σ is the gas conductivity in mho/m, A is the electrode area in square meters, and k is a geometric correction factor which is approximately unity for large electrodes. The correction factor is usually determined by direct experiment using a convenient conductor (e.g. copper sulfate solution).

If the input impedance of the oscilloscope or instrumentation amplifier is much larger than the internal resistance of the gage the resistive voltage drop in the generator is negligible and open circuit voltage is measured. In that case the measured voltage is proportional to velocity, and it does not depend on the value of the gas conductivity.

A necessary condition for the velocity gage to work is therefore that the gas resistance be much smaller than the input impedance of the instrumentation amplifier. In explosive MHD studies the internal gas resistance is about a milliohm, and in combustion MHD for large power installations

the internal resistance is a fraction of an ohm. In these cases there is no problem whatsoever in measuring open circuit voltages. In the magnetic velocity gage for DABS, on the other hand, gas resistance is very high, and there is considerable difficulty assuring that the condition is met. Furthermore, as will be discussed later, when all the signal processing occurs at very high impedance levels, static charge and capacitative coupling become circuit design concerns not present in the MHD work.

2.2 Gas Conductivity

A DABS blast pulse is produced by detonating an explosive in a confined earthen tube. At the test station the first portion of the pulse is shocked air, followed by expanding detonation products. Because of the large compression of air, together with interface mixing, the bulk of the blast pulse is composed of detonation products.

Conductivity of the gas is principally determined by temperature and the ionization potentials of the gas constituents. At the low temperatures of expanded explosive gases (less than 1500 K) it is necessary to "seed" the gas with metals such as potassium or cesium. As long as the seed material is only a few percent the temperature of the gas is essentially unchanged by seeding. Temperature is therefore determined by the properties of the expanding

explosive gases, and conductivity will be determined by the seed material present.

We are not aware of any temperature measurements in expanded explosive products, but there have been computer calculations based on equilibrium thermochemistry assuming isentropic expansion from the detonation state. The latest and best of these explosives codes is the TIGER code (Reference 1). Published calculations were available only for TNT and RDX; the results are shown in Figure D2.

Temperature ranges from about 1100°K to about 800°K. Higher temperatures are obtained from a relatively low density explosive, presumably because of the increased entropy caused by compression at the detonation front. Temperatures are lowest at low pressures, as is expected.

Actual temperatures in an experiment may differ substantially from these curves for several reasons. The explosive in a DABS test is an array of PETN detonating cords. The gases expand radially out from the cords at first, then stagnate and expand as a whole at a lower pressure to drive the blast wave. The process of stagnation and reexpansion increases the entropy of the gas, which increases its temperature at a given pressure. Furthermore there is burning of the gases with air in the blast tube, which will increase the temperature.

Conductivity of a gas depends on the number of electrons

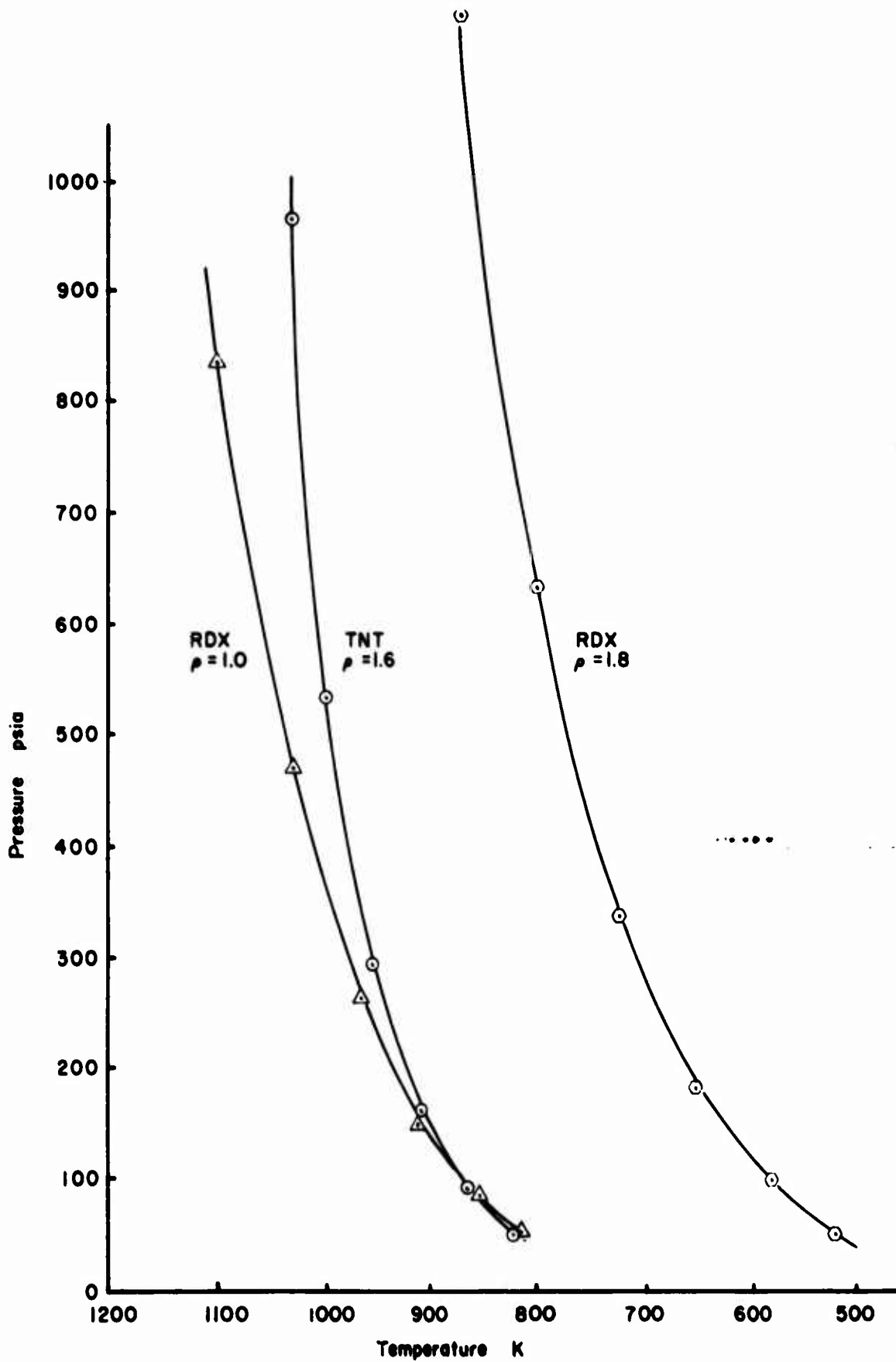


Figure D2. Tiger Calculations of Expanded Explosive Gases

present and the average collision cross-section of the gas molecules. Electron number density may be estimated from equilibrium chemical thermodynamics using data on expanded explosive products together with a selected seed material. These calculations are quite lengthy and tedious; it turns out that certain electronegative compounds (e.g. CN^- and CO_2^-) play an important role in suppressing electrons and must be included in the calculations.

The results of these equilibrium conductivity calculations are shown in Figure D3. The conductivity is strongly temperature dependent, varying many orders of magnitude in the temperature range of expanding explosives. The actual quantity of ionized seed material in the gas is minute; at these temperatures the material is barely melted, much less vaporized, and the partial pressure of the vapor state is very small. Consequently it takes very little seed material to achieve saturation. However, considerations of mixing and evaporation rates suggest putting several percent of seed material into the explosive. The difference in conductivity between cesium and potassium is about a factor of 50, but the cost difference is many orders of magnitude.

Nonequilibrium effects may be dominant in establishing the electrical conductivity, because the electron concentration is very small and the expansion time is very short (a few milliseconds). For example nonequilibrium chemistry is

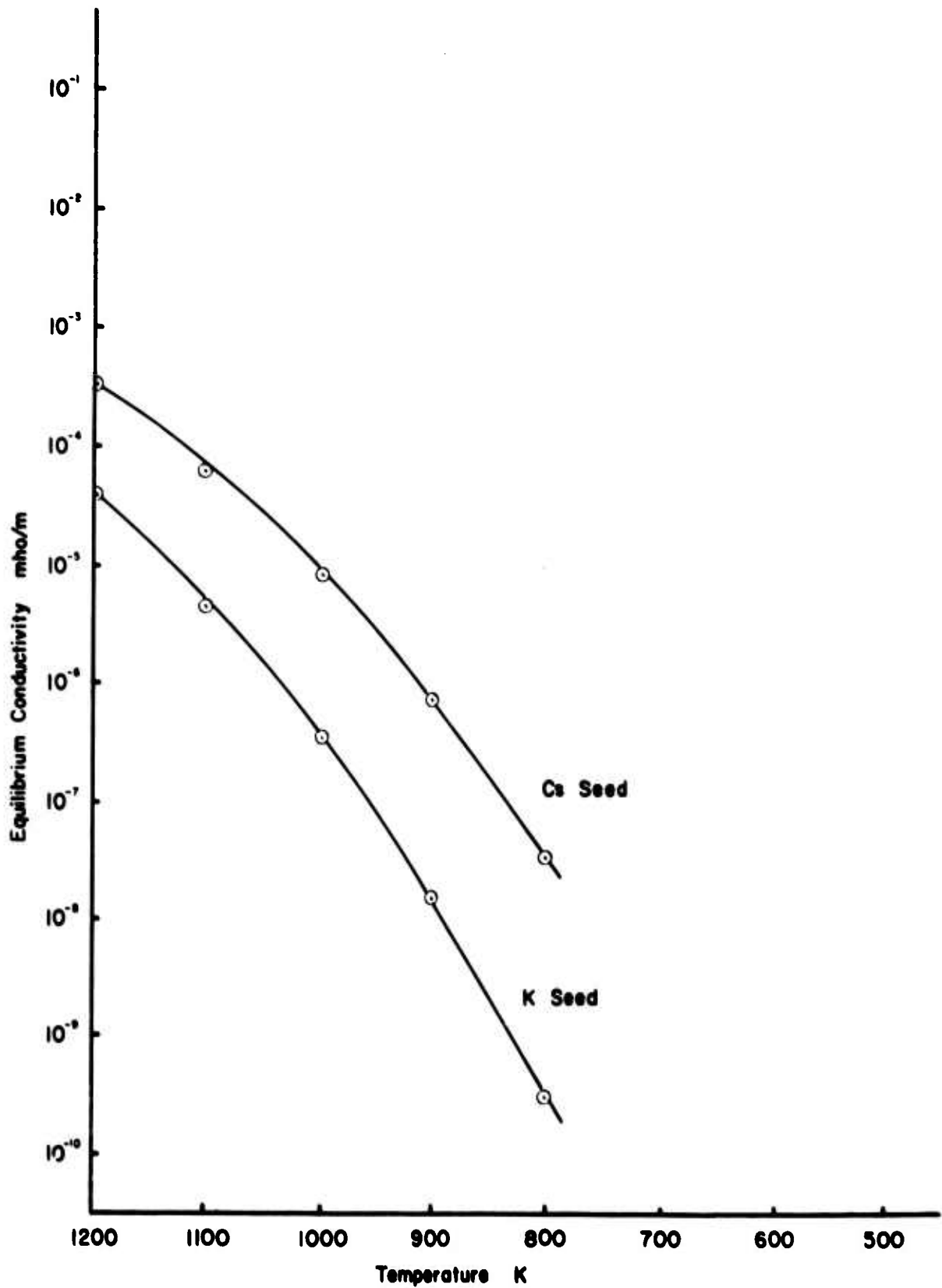


Figure D3. Equilibrium Conductivity Calculations

largely responsible for automobile smog production; equilibrium concentration calculations show vanishingly small concentrations of many noxious species.

If seed material is imbedded in the DABS explosive to assure exposure to the extreme detonation conditions, the likely result of nonequilibrium effects is to increase conductivity by delaying electron recombination. If the seed material is outside the explosive, relying on late-time mixing effects, non-equilibrium effects would result in lower conductivity due to delayed evaporation of the seed material.

3. EXPERIMENTAL RESULTS

The objective of this program (Artec Project 122) was to determine the feasibility of the magnetic velocity gage principle for AFWL DABS tests. Preliminary calculations indicated that the critical parameter is internal resistance, determined by gaseous conductivity. If internal resistance is less than the input resistance of practical instrumentation amplifiers, gage output will accurately measure velocity; if internal resistance is greater, gage output will be reduced by a factor depending on gas conductivity.

Phase I consisted of five explosive experiments conducted at the FMC test site in Hollister, California. All shots used essentially the same configuration, shown in Figures D4 and D5. The explosive was contained in a 10-foot long 12-inch diameter cardboard tube tamped by several feet of sand. Four 5-foot long bundles of 400-grain detonating cord were suspended approximately 6 inches apart in the first half of the tube. The explosive driver tube was connected to a 20-foot long steel pipe to achieve proper pulse amplitude and duration. The transition pipe was flanged to a 3.5-foot long stainless steel test section, which contained magnetic field coil and electrodes. An additional 10-foot length of cardboard tube connected to the test section helped to maintain pulse duration.

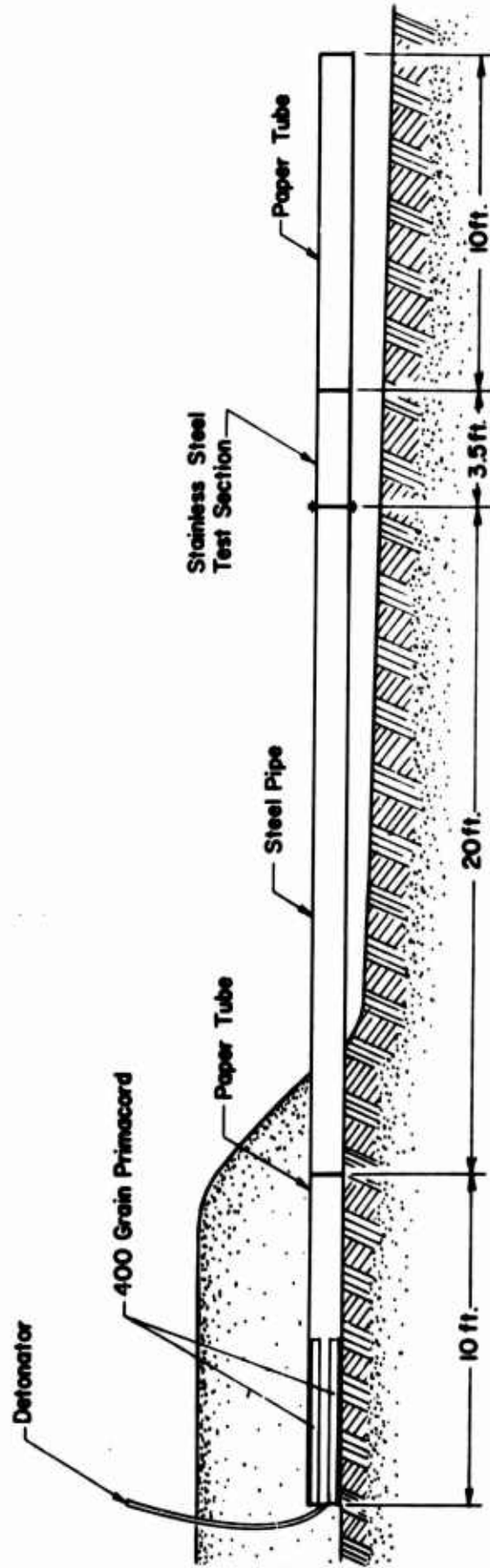
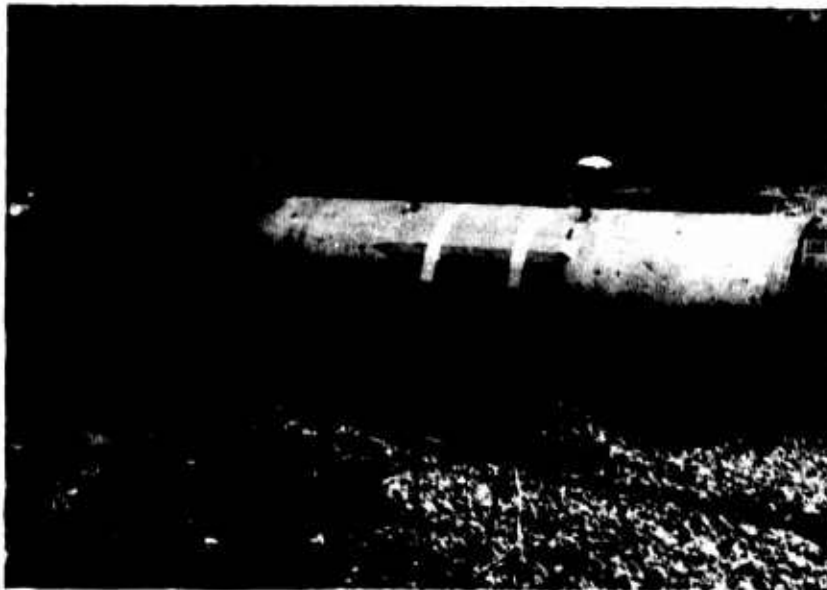


Figure D4. Experimental Setup of Shot 122-2



Experimental Setup, Shot 122-2



Test Section

Figure D5. Pre-Shot Photographs of Shot 122-2

Shot 122-1 successfully verified the mechanical performance and post-shot integrity of the test components. Shot 122-2 was the first electrical test.

Seeding of the explosive in 122-2 was accomplished by mixing cesium chloride with an approximately equal volume of PETN explosive powder in paper tubes taped to the explosive charges. An amount of seed material equal to 1% by weight of the total explosive charge was used.

Electrodes were fabricated as an 8 x 20 array of separate elements connected electrically in parallel, which was shown by auxiliary laboratory tests to work as well as solid electrodes (as shown in Figure D6). Each element consisted of a U-shaped piece of stainless steel wire passed through holes in the test section sidewall. Plastic sleeves provided electrical insulation, and epoxy provided mechanical rigidity. The inside of the stainless steel test section was coated with Cotronics ceramic insulating material. The electrode elements protruded approximately 3/8-inch and were canted at an angle of 30 degrees from the flow to improve electrical contact with the gas, as it was felt that a cold boundary layer would add a high resistance to the electrical circuit in the gas. The electrode constant relating resistance to conductivity is $.4 \text{ m}^{-1}$.

The objective of 122-2 was to measure the average conductivity of the gas by means of the circuit shown in Figure

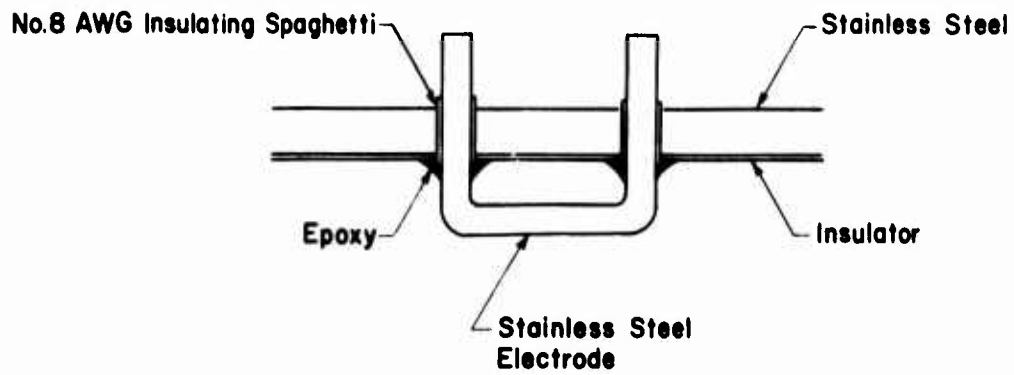
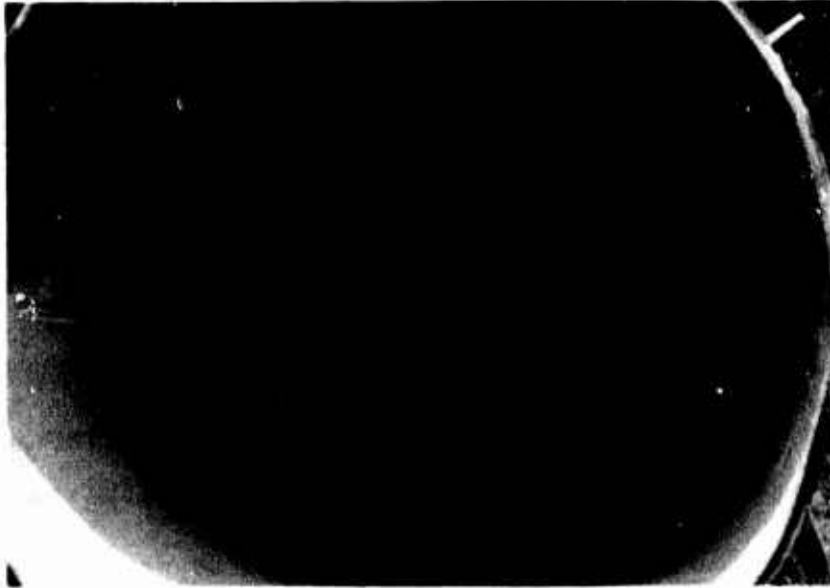
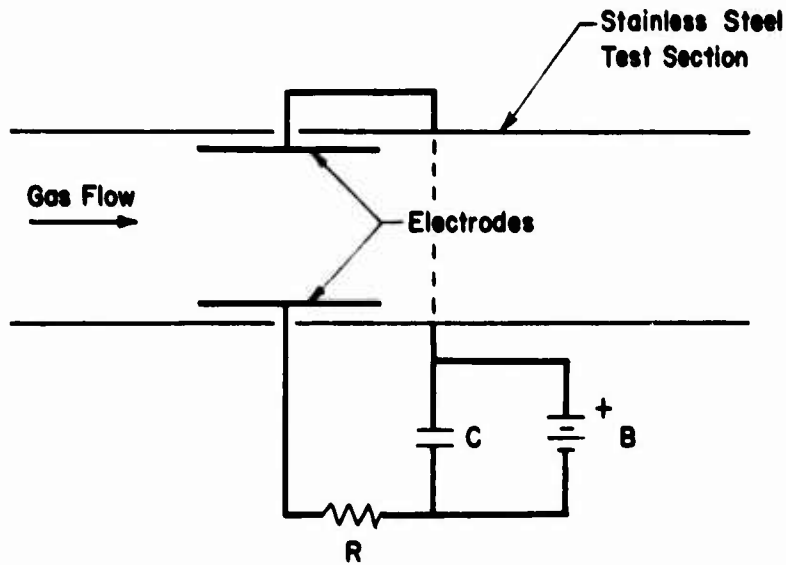


Figure D6. Test Section and Electrode Detail

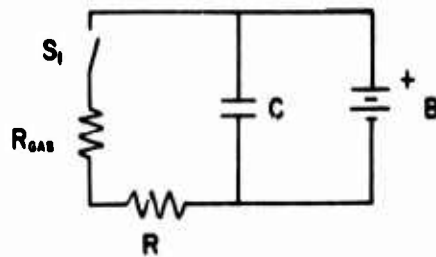
D7. The capacitor discharge time is long (minutes) compared to gas flow duration (milliseconds), and so acts as a constant voltage source. The gas resistance is determined by measuring the source voltage and the voltage drop across a known resistance. Average conductivity is obtained from measured resistance using the known electrode constant.

The explosive driver produced 250-400 psig gas pressures in the test section, representing acceptable DABS test conditions. Conductivity measurement was unsuccessful because of a short-circuit which occurred between an electrode element and the test section tube wall during the test. It was also noted that epoxy seal material was broken from several other electrode elements, and some gas escaped through the mounting holes possibly providing additional electrical shunt paths.

Shot 122-3 was essentially a repeat of 122-2 with improvements in electrode mounting. All the electrode elements were removed and critical mounting holes were beveled to reduce the chances of a short circuit. New sleeves were installed with generous amounts of epoxy. The Cotronics insulator coating, which had evidenced some cracking and chipping, was removed and replaced with a high temperature insulating paint on both the inner and outer diameters of the stainless steel test section, along with additional layers of high temperature duct tape. The test section was isolated electrically from the steel transition pipe.



Physical Schematic



Electrical Schematic

The Gas Completes The Circuit (Closes S_1) When It Arrives At The Electrodes. With The Capacitor Discharge Time Chosen Correctly, The Gas Resistance

$$R_{gas} = \frac{C}{\sigma} = R \left(\frac{V_b}{V_n} - 1 \right)$$

C = Constant

V_b = Battery Voltage

V_n = Voltage Drop Across R

σ = Conductivity

Figure D7. Gas Conductivity Measurement

By direction from CERF the seed material was changed from cesium chloride to potassium chloride on the basis of economy for large scale DABS tests. Because of its low cost, 5% by weight of potassium chloride seed was used instead of 1%. No other aspects of the shot were changed from 122-2.

The driver operated about the same as the previous shot, but again conductivity data was lost by an electrode short circuit. Post-shot inspection revealed that gas again had escaped through a few of the electrode element mounting holes causing a low impedance shunt to the stainless steel test section.

Because of time and budget constraints the next shot was configured to provide both velocity gage data and conductivity data. Magnetic field was provided by an 80-turn saddle coil with an average B/I of 3.6 gauss/amp over the electrode volume. Four automobile batteries in series provided enough current to generate a field of 180 gauss. The electrode elements were reworked, and a solid mechanical backing to prevent gas leakage was provided by high density Hydrostone casting plaster. The Hydrostone was thoroughly dried to maintain high impedance levels (in excess of 20 megohms). Separate 1-inch diameter electrodes near the upstream end of the test section were included to obtain conductivity data. The stainless steel test section, the pressure gage, and the conductivity gage electrodes were all

carefully isolated electrically to minimize spurious ground paths.

The conductivity gage apparently worked well in 122-4. Raw data from the tapedeck is shown in Figure D8, and reduced data is shown in Figure D9. Conductivity ranged from 10 to over 100 micromhos/m, with peaks at the shock front and what appears to be the burning interface between air and explosive products. This conductivity corresponds to a velocity gage resistance from .4 to 4 megohm, which is high but may be acceptable with high input impedance amplifiers.

Velocity gage data in this shot showed large oscillations. A major factor contributing to this effect was determined after the shot to be electrical crosstalk occurring in the gas between the conductivity gage electrodes and the velocity gage electrodes. The conductivity gage had nearly 300 volts across it, while the velocity gage had about 5 volts. Trickle currents through the gas produced several volts at the velocity gage electrodes from the conductivity gage electrodes; this effect was confirmed by lab tests using copper sulphate solution.

Considerable effort was put into the electrical design of shot 122-5 to isolate the high impedance velocity gage electrodes from other circuitry, as shown in Figure D10. A PCB Model 402M41 voltage follower amplifier was used,

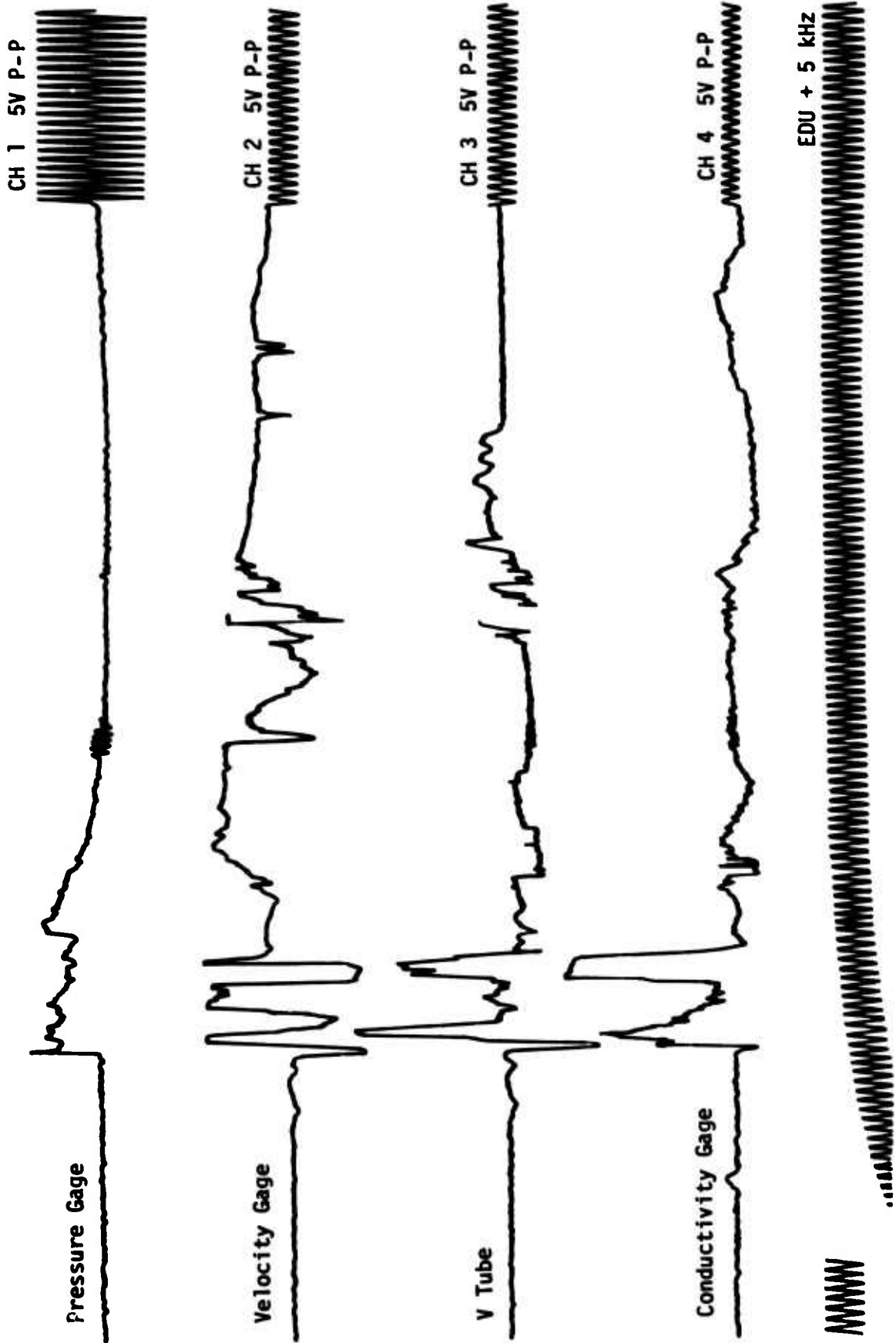


Figure D8. 122-4 Raw Data

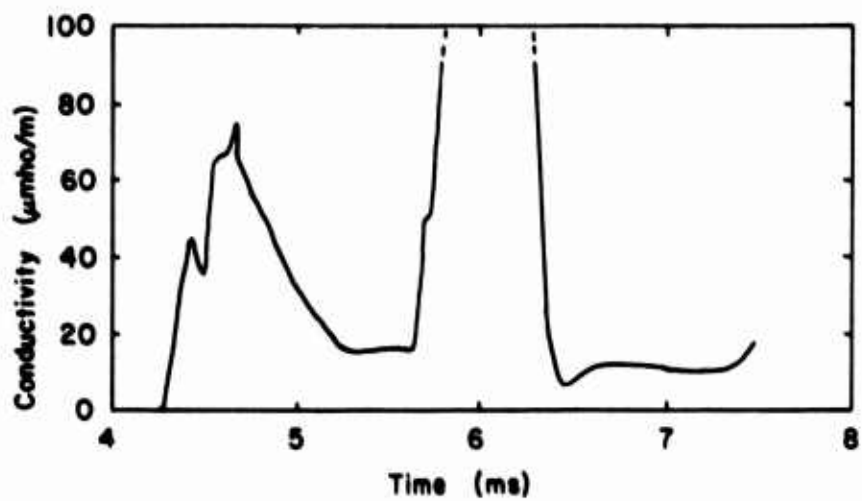
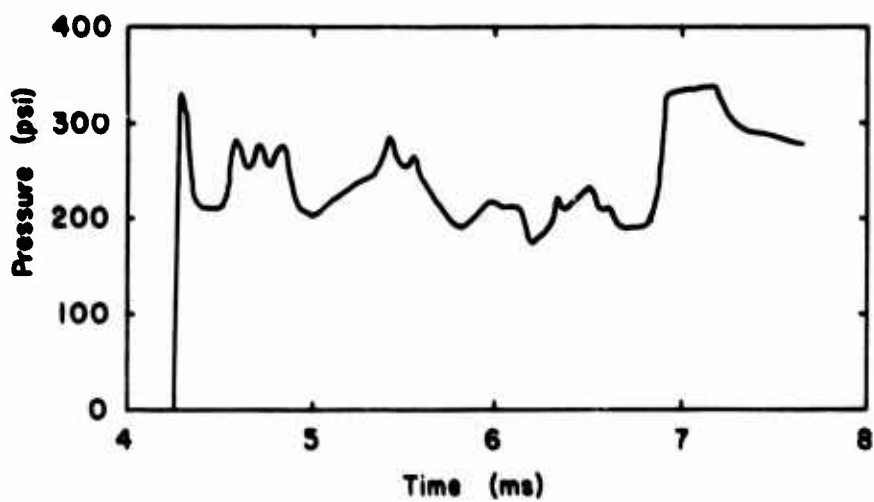
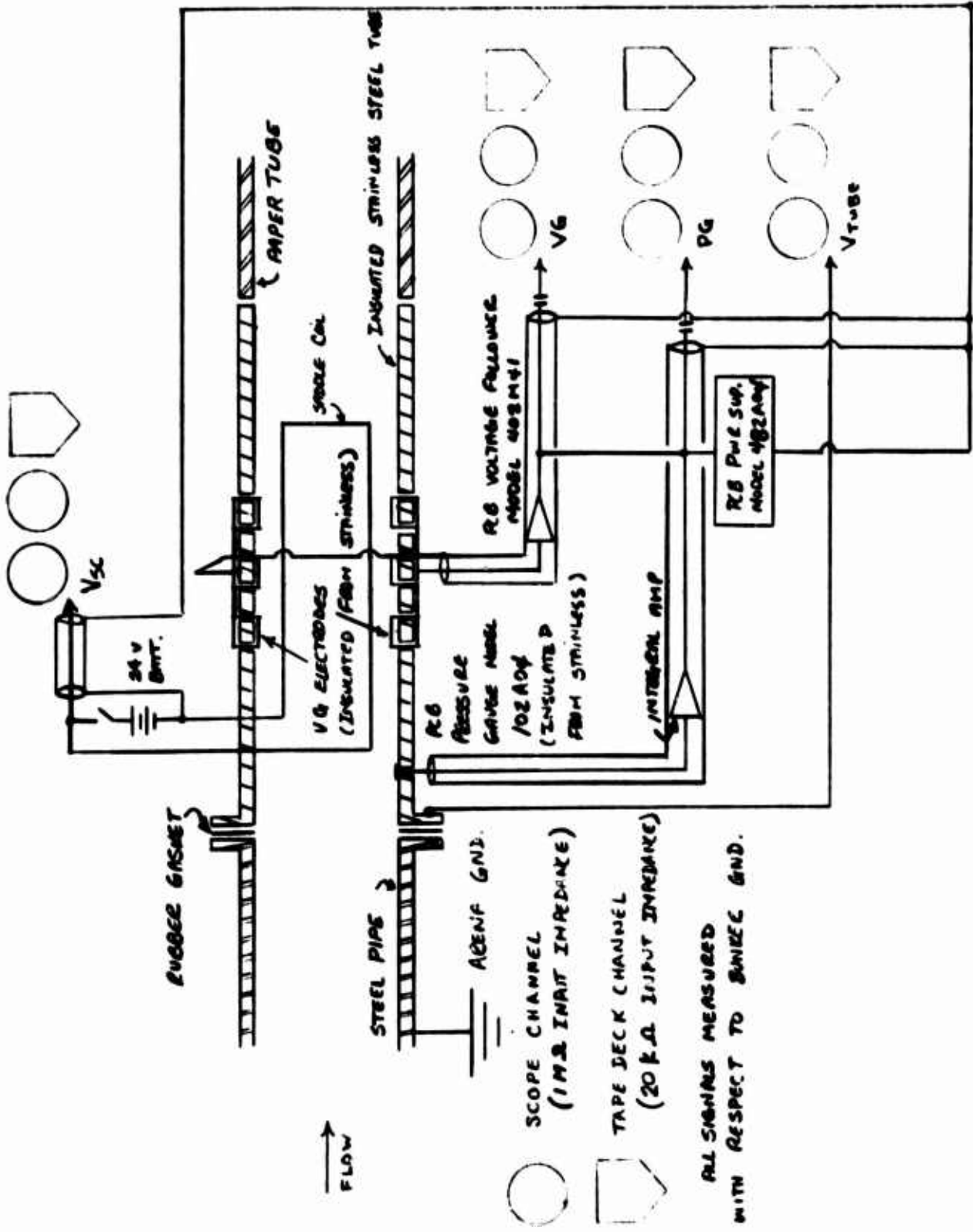


Figure D9. 122-4 Reduced Data

which has an input impedance of 10^{11} ohms. The conductivity measurement was eliminated, and in addition the voltage level of the velocity gage was halved to eliminate clipping by using only two batteries to power the field coil instead of four. All other aspects of the shot were identical to 122-4.

Raw data from 122-5 is shown in Figures D11 and D12, and reduced data is shown in Figure D13. In general the shot performed very well except for anomalous pulses in the velocity gage data at shock arrival and at pulse termination. Measured velocities appear reasonable, although they have not been compared to a detailed theoretical calculation of the experimental setup. The velocity data appears smoother than the pressure data, as though it were filtered by RC effects in the generator.

Post shot analysis has indicated that the likely source of the anomalous voltage pulse is a static electricity effect associated with the shock tube boundary layer. Grosse (Reference 2) has investigated static charge phenomena in shock tubes, and found coupling effects similar to what was observed in 122-5. Grosse concluded that the mechanism was a charged boundary layer produced by shearing and compression effects inducing a voltage on pickup electrodes by capacitive coupling. This interpretation is supported by observations of voltage on the stainless steel tube, which is also coupled



BURKEE GND.

Figure D10. 122-5 Diagnostic Setup



Top: Stainless Steel Voltage
10 V/cm 5 ms/cm

Bottom: Velocity Gage
3.18 km/sec/cm
5ms/cm



Top: Stainless Steel Voltage
5 V/cm 2ms/cm

Bottom: Pressure Gage
106 psi/cm 2ms/cm

Figure D11. 122-5 Raw Data From Scope Traces

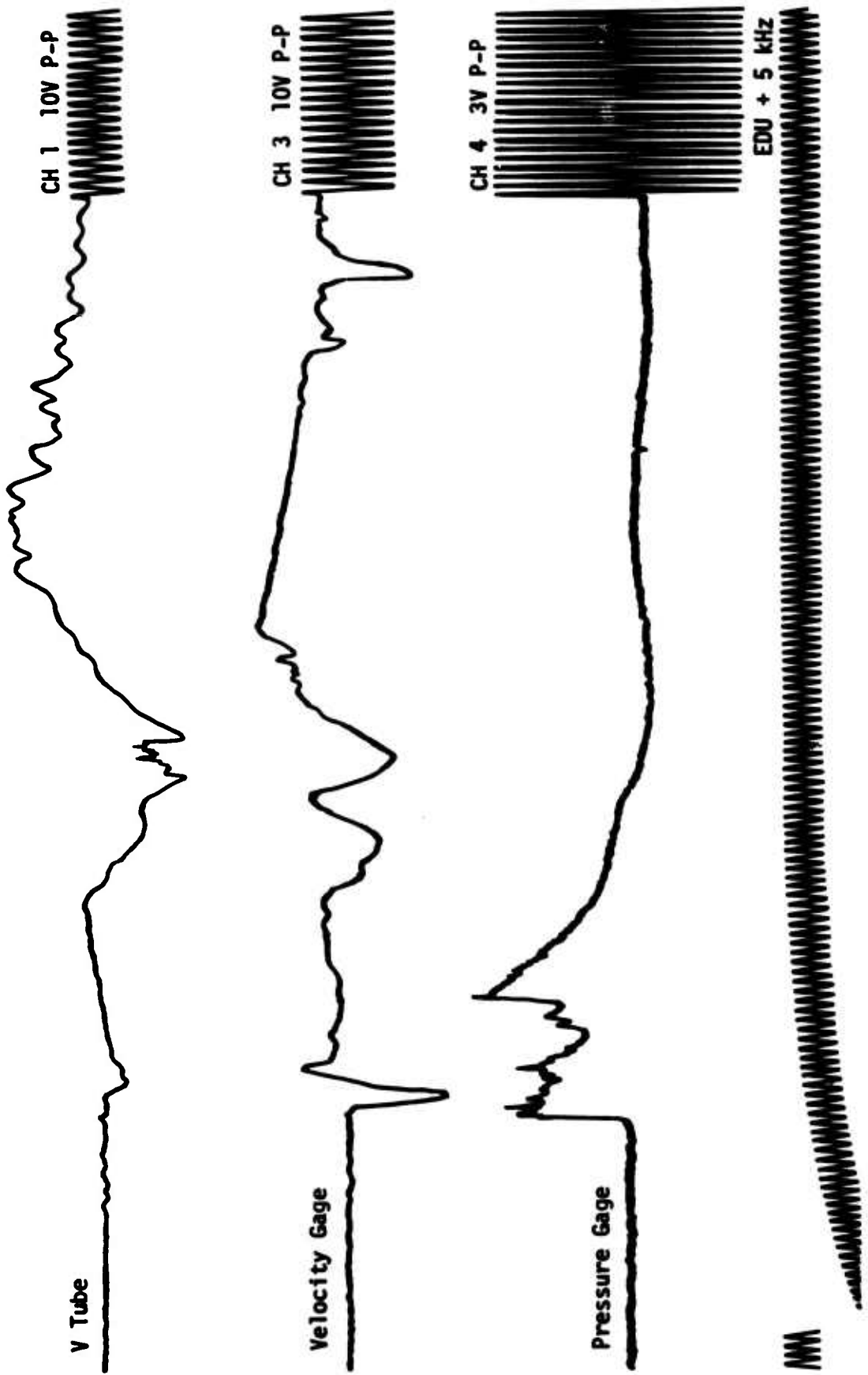


Figure D12. 122-5 Raw Data from Tape Deck

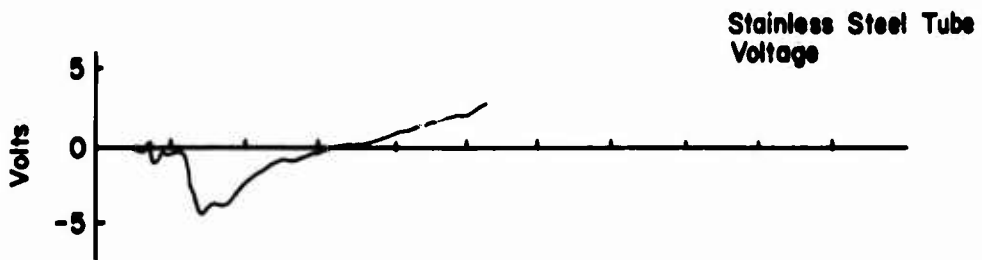
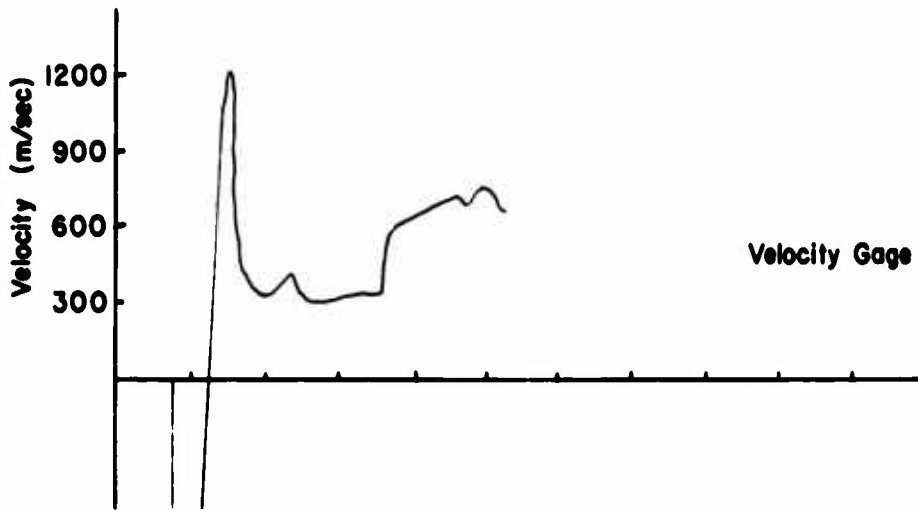
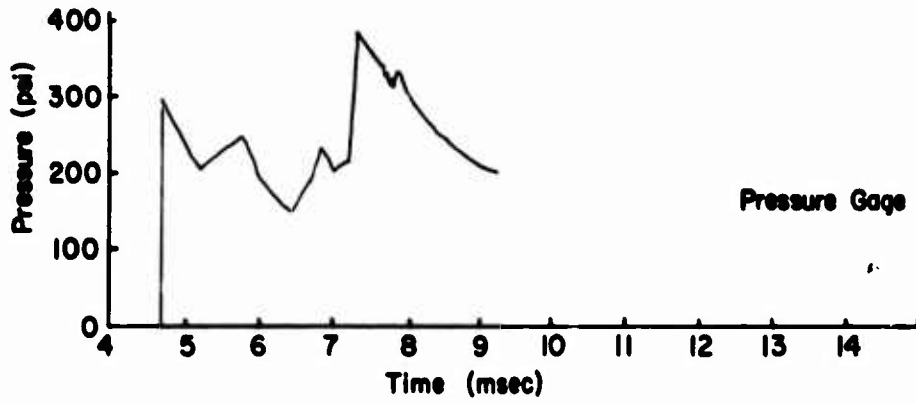


Figure D13. Reduced Data, Shot 122-5

capacitively to the surface charge but with capacitance history different from the electrodes.

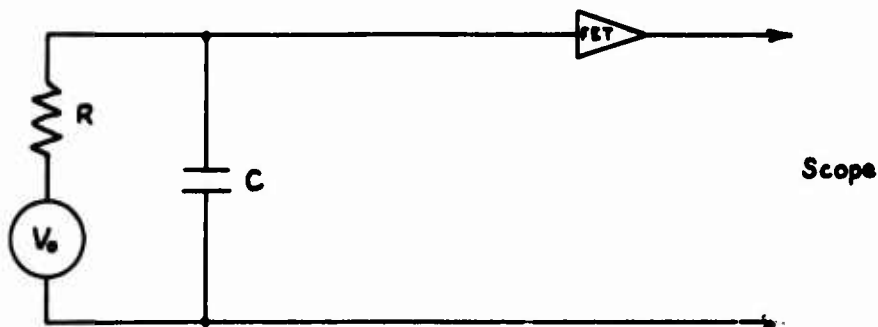
4. CONCLUSIONS AND RECOMMENDATIONS

4.1 Conductivity Data

Shot 122-4 successfully obtained conductivity data on the test gas. It ranged from 10 to 100 micromhos/m, which is several orders of magnitude better than preliminary equilibrium calculations, but consistent with expectations based on nonequilibrium phenomena. The measured conductivities correspond to gas resistances in the velocity gage ranging from .4 to 4 megohm. Use of cesium instead of potassium would theoretically lower this resistance by a factor of about 50, but it is a costly material for large tests.

With gas resistance in the megohm range it is necessary to use a high input impedance amplifier, and a commercial FET amplifier with input impedance of 10^{11} ohms was used in 122-5.

At these high impedance levels shunt capacitance becomes a problem. For example consider the circuit:



This circuit acts as an RC filter on the velocity gage voltage. To achieve reasonable fidelity in a typical DABS blast pulse, $RC < 1$ msec. For a gas resistance of one megohm, this condition limits allowable shunt capacitance to 1 nanofarad. A higher gas resistance would require a lower shunt capacitance.

Sources of shunt capacitance are connecting cable, capacitance of electrodes to electromagnet coil, and capacitance of electrodes to metal structures. In the particular case of the Artec tests at FMC test site the shunt capacitance was 3.0 nf. This was unusually high because of a stainless steel channel. In a DABS test where the entire gage is immersed in the blast it can be made of fibreglass, resulting in lower shunt capacitance.

Velocity gage data was successfully obtained in Shot 122-5. It was smoother than the corresponding pressure gage record, so some degree of RC filtering was probably present. Velocity magnitudes appear reasonable, but neither computer calculations of the experimental setup nor alternate velocity measurements were available as a check.

A static electricity noise problem was identified in 122-5. A sharp negative-going pulse occurred at shock arrival, and a slower oscillation occurred toward the end of the blast wave.

Static electricity noise was considered as a potential

problem for high impedance velocity gage measurements early in the program, and this effect seemed to be borne out by an experiment at AFWL (Figure D14). In that experiment 30 volts of electrostatic noise was measured between two metal plates resting on a DABS shock tube floor. The explosive was not seeded.

Further consideration of this effect indicated that seeding, if at all effective, should eliminate the problem. Charge concentrations cannot persist in a conducting gas; they equilibrate on a time scale of the order

$$\tau = \frac{\epsilon_0}{\sigma} \quad (D4)$$

Even low conductivities, on the order of 10^{-8} mho/m, lead to an equilibration time of less than a millisecond. If the gas is sufficiently conductive for the magnetic velocity gage to work, static charges cannot be carried along by the flowing gas, and this type of noise should not be a problem.

The electrostatic noise measured in 122-5 is apparently of a different nature from the noise measured by AFWL. Noise in the AFWL test (Figure D14) was rapidly oscillating, with oscillations persisting throughout the pulse duration. Noise in Artec Shot 122-5 consisted primarily of a single oscillation at the start of the pulse, and a longer single oscillation toward the end of the pulse.

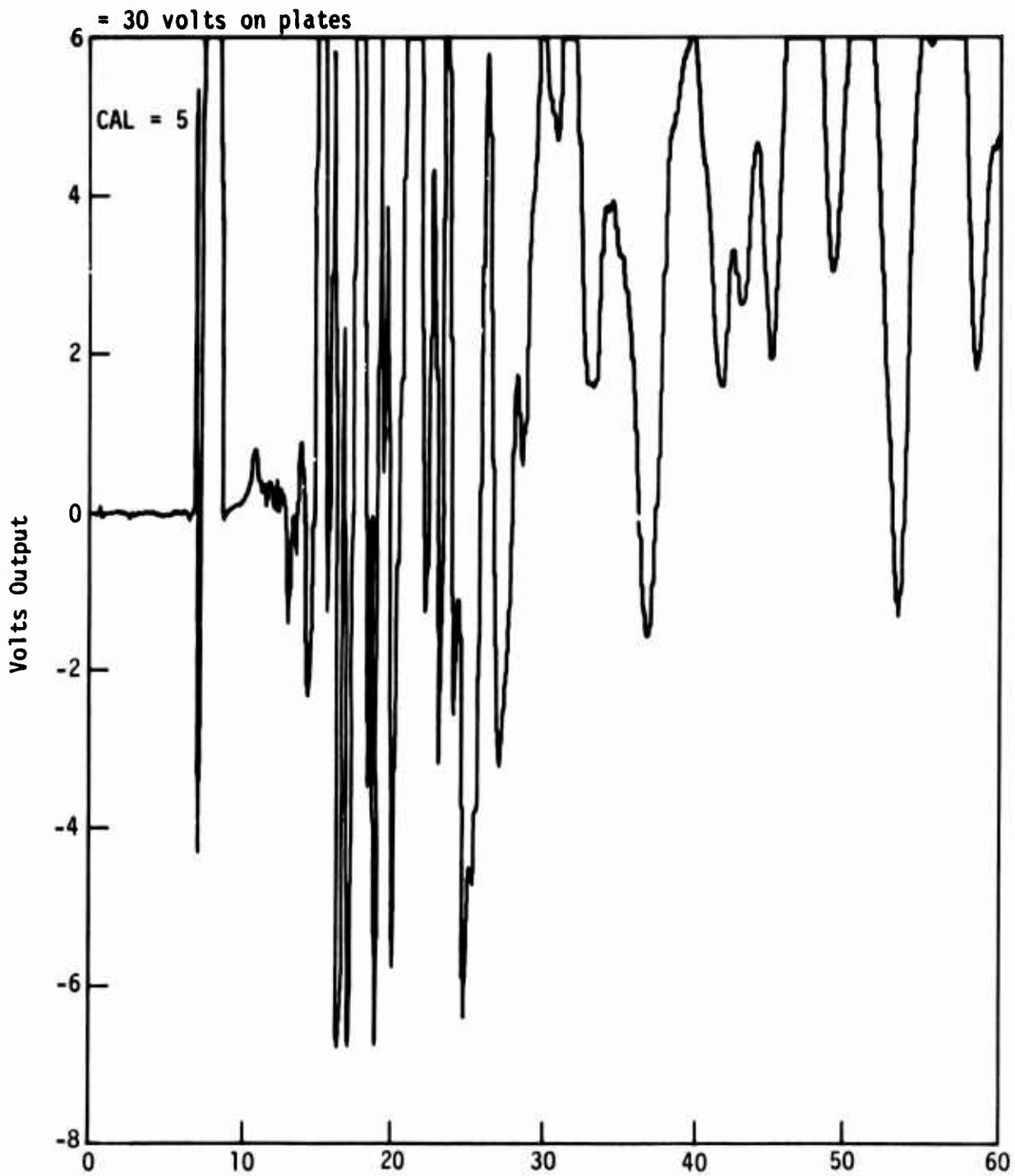


Figure D14. AFWL Noise Test Raw Data

This type of noise appears to be related to surface electrostatic phenomena previously observed in shock tubes. Grosse (Reference 2) has made extensive observations of these electrostatic effects, and concludes that they can be explained by a static charge in the boundary layer. The magnitude of this charge layer, about 10^{-9} coulomb/m², is sufficient to induce voltages in sensing electrodes by capacitative coupling. The charge is produced by compression or shearing effects at the boundary. Since the boundary layer is cold, the conductivity is low and the charge persists a long time.

Assuming a surface area of 1 sq. meter, which is about right for the Artec experiments, the 10^{-9} coulomb charge would produce a 1 volt signal across a 1 nanofarad capacitor. Thus the observed voltage is of correct order of magnitude to be explained by the boundary layer charge effect.

Electrostatic boundary layer effects and their effects on high impedance measuring circuits are poorly understood at present, but there is no reason to believe that they cannot be circumvented by an appropriate circuit design.

In an actual DABS test the magnetic velocity gage would be located in the core flow, well away from the shock tube boundary layer. In that case the only boundary layer is the one formed over the electrodes themselves, and any resulting effects are likely to be small. Even in the Artec test

setup the electrodes could be moved further away from the wall to minimize capacitive coupling to the boundary layer charge.

4.2 Recommendations

For the immediate DABS test program our recommendation is that the MHD velocity gage not be fielded in a Phase II test effort. It is possible to field a high impedance gage, but the associated practical problems of static noise, stray capacitance, and spurious pickup are not likely to be solved in time for the test program. It is felt that with further effort the high impedance difficulties could be overcome.

For tests conducted with a higher temperature gas (e.g. a tunnel test using a high energy source or a high pressure DABS) the magnetic velocity gage is likely to prove more effective. Conductivity is highly sensitive to temperature, and any seeded flow over about 1200 K would have internal resistance well below a megohm, thereby eliminating high impedance problems.

REFERENCES

1. M. Cowperthwaite and W. H. Zwisler, "Improvement and Modification to TIGER Code", Stanford Research Institute Project Report PYU-1397, Contract N60921-72-C-0013 (January 1973).
2. F. A. Grosse, "Electrostatic Effects In the Shock Tube", PhD. Thesis Lehigh University, 1966.

APPENDIX E
RECOMMENDATIONS FOR INSTRUMENTATION
FOR DYNAMIC AIRBLAST SIMULATOR

	<u>Page</u>
Introduction	178
Radiative Diagnostics	178
Conclusions	189
References	194

INTRODUCTION

The Dynamic Air Blast Simulator (DABS) is an explosively-driven shock tube being developed to simulate nuclear blast wave phenomena on a variety of structures. As a simulation facility it should reasonably reproduce the pressure history of a nuclear blast wave. Several small scale, exploratory DABS have been built and fired. These tests have generally demonstrated reasonable pressure levels and pressure time histories. However, several questions remain: (i) at least two of the three tests to date have shown "spurious" double spiked pressure traces; the origin of this phenomenon is unclear. (ii) Since the utility of this facility is structure loading, a direct measure of the dynamic forces is important. (iii) Scaling laws need to be verified.

To provide further diagnostic concepts as an aid in understanding the operating performance and scalability of the DABS facility, a meeting was held at CERF, May 18 and 19, 1976. At this working group, the DABS test data, diagnostics, and technical issues were discussed. Recommendations were made for additional diagnostics for the next test scheduled for June 17th.

This letter report documents this consultant's ideas concerning radiation measurements that might be attempted on the next and future DABS tests.

RADIATIVE DIAGNOSTICS

A. Objectives

Measurement of the emitted or absorbed radiation is an important and highly developed diagnostic for high temperature gases. The intensity, temporal history, and spectral content of radiation can, in principle, yield information about gas density, temperature, state of excitation, and species identification to mention a few important variables. With the recent availability of lasers covering a wide range of wavelengths, many sophisticated optical measuring techniques have been developed.

However, the emphasis on this study has been to consider simple optical systems which have the capability of providing overall, gross measurements. The rationale for the above emphasis is several fold: (i) The very hostile environment of DABS precludes sophisticated experiments and expensive equipment. (ii) The time scale for the next test (June 17th) precluded any instrumentation development. (iii) At present it is more cost effective to proceed with simple experiments which are easy to interpret. More costly diagnostics might be developed later if required.

The recommendations of the working group in the optical area were to attempt to measure infrared emission at several selected wavelengths using simple IR radiometers and transmission in the visible using both a pulsed ruby laser ($\lambda = 6943 \text{ \AA}$) and a broadband source. The following sections briefly describe some of the technical issues involved in attempting to field and interpret such measurements.

B. Environment

The unique environmental conditions of DABS make it difficult to design optical diagnostics which have unequivocal interpretation. For example, the construction of the shock tube consists of a trench in the desert with concrete walls, dirt floor, and a wood roof. This construction creates unusual problems with radiation diagnostics. It does not appear possible to completely characterize the driven gas conditions as to temperature, density, and species concentrations. There is evidence for a substantial carbon (soot) content in the driver gas. This may result from the fact that the PETN explosive contains up to 20% of "inert" plastic binder material. There is data which indicate that the driver interface is a highly turbulent, combusting, and radiating gas. Finally, the high densities of operation (\geq atmospheric) and long path lengths (6 - 8 ft) suggest that optical opacity may be serious. There is photographic evidence of an opaque region that accompanies the blast wave.

From previous DABS test data¹, it can be seen that the average velocity of the shock is $\sim 6500 \text{ ft/sec}$ ($2 \text{ mm}/\mu\text{sec}$). Based on this shock velocity, the

post shock conditions for equilibrium air are:

$$T_2 \sim 2000^\circ\text{K}$$

$$\rho_2/\rho_1 \sim 6$$

$$P_2/P_1 \sim 40$$

where T = temperature, ρ = density, and P = pressure. Subscripts refer to (1) initial unshocked, and (2) post-shock conditions. A graph of the equilibrium composition of air for 2000°K is shown in Fig. E1.² For the shocked gas density of DABS ($\log \rho/\rho_0 \sim 0.7$), it can be seen that the gas would contain $\sim 1\%$ NO , 0.04% CO_2 (ambient) and a small amount of NO_2 ($\sim 10^{-2}\%$). These are the only infrared active species. In addition, the electron concentration is obviously very low and probably dominated by easily ionized impurities such as Na. The assumption of equilibrium conditions is justified because of the high gas densities involved. For example, an estimate of the time to form NO under these conditions is $\sim 1 \mu\text{sec}$.³

Unfortunately, the explosive driver conditions are far less easy to characterize. Martens⁴ has used a hydrocode to calculate blast wave strength for explosive loadings and geometries comparable to DABS tests. However, this code does not determine explosive product species concentrations or temperature. Cook⁵ gives "typical" detonation concentrations for PETN, but the details and validity of these results is questionable. Nevertheless, Cook's results would imply that N_2 , CO_2 , H_2O and CO are all probably present in roughly equal concentrations. The temperature of the detonation products initially is about $2000 - 3000^\circ\text{K}$ and decreases as the gas expands. There is evidence of a highly luminous contact surface which propagates down the tube just behind the shock front. This luminous front is caused by further combustion of the detonation products as they mix with the hot air. A specification of the conditions within this burning interface is not practical.

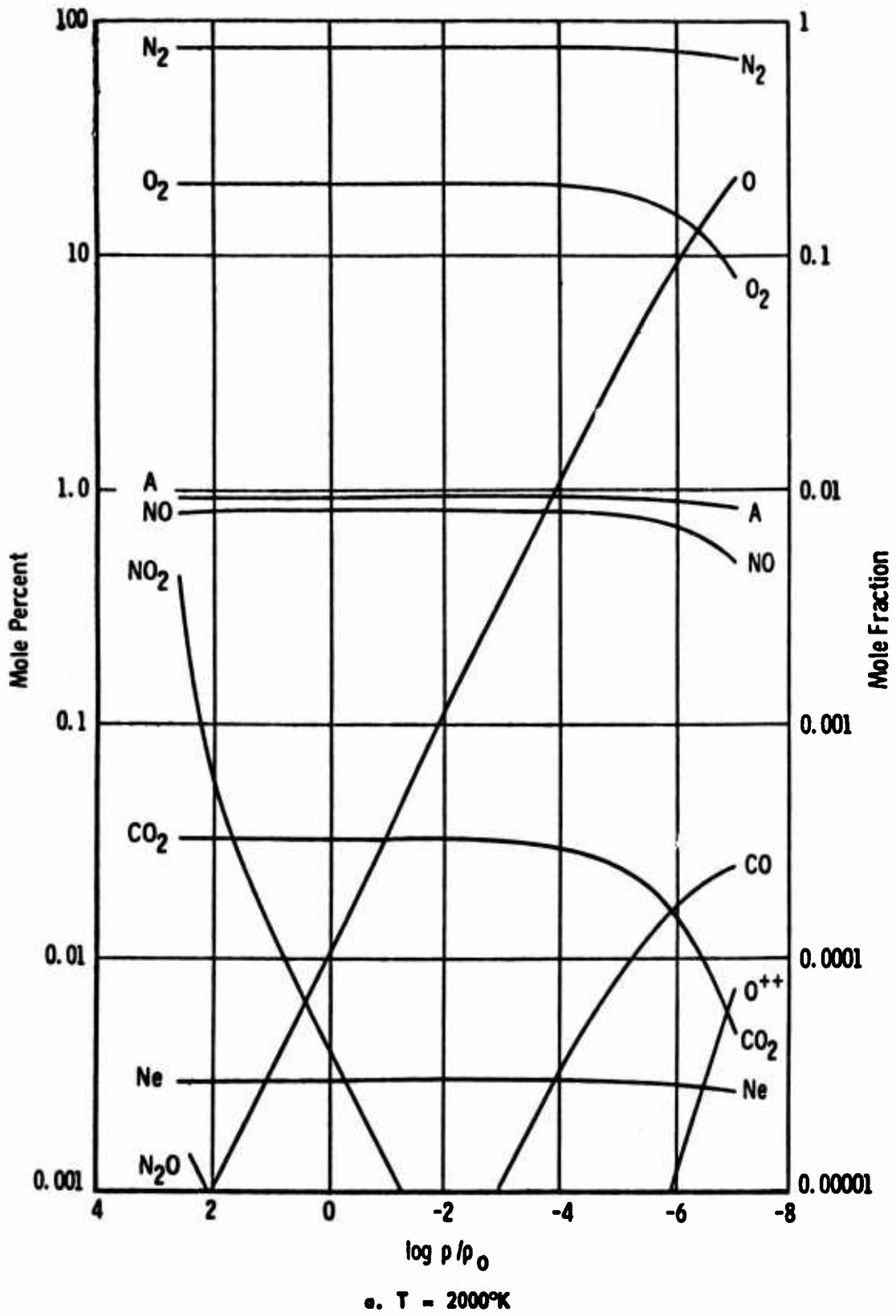


Figure E1. Equilibrium Composition of Air

Another feature of this facility is the production of the substantial amounts of carbon (soot) by the detonation/combustion process. The origin of this free carbon is not clear, but one reasonable source is the plastic binder of the PETN primer cord which burns and vaporizes in the detonation. For example, for 600 lbs of PETN there will be about 85 lbs of plastic. If 10% of this plastic material is converted into carbon, $\sim 4 \times 10^3$ gms of C are produced. If this carbon is uniformly distributed throughout the entire tube, the mass loading of carbon is about 3×10^{-5} gms/cm³. The particle size distribution is not known. However, soot formed by hydrocarbon combustion typically shows sub-micron particle size. With this assumption and the large mass loading of C we can calculate an absorption length, L, in the particle laden gas in the volume absorption limit.

$$L = \left(\frac{M}{\rho} \alpha \right)^{-1}$$

where M is the mass loading of particles of density, ρ and α is the volume absorption coefficient for C which is shown in Fig.E2. For the mass loading considered $L \sim 10$ cm and the gas is generally optically thick in the infrared. The situation would even be worse (smaller optical depth) in the visible.⁶ This calculation is very approximate, but it would appear that the particle laden detonation products would make it difficult if not impossible to perform absorption or molecular scattering (i. e. Raman) measurements. However, if the gas is optically black, then it can be treated as a blackbody (see below).

C. Radiation Techniques

A number of infrared optical techniques were considered to determine the temperature of the shock heated gas or detonation products as they flow down the tube: emission from neutral Bremsstrahlung, emission from CO₂, NO, etc., absorption of CO₂ laser lines, and two color measurement of blackbody radiation.

NORMALIZED RAYLEIGH ABSORPTION CROSS SECTION

T = 300° K

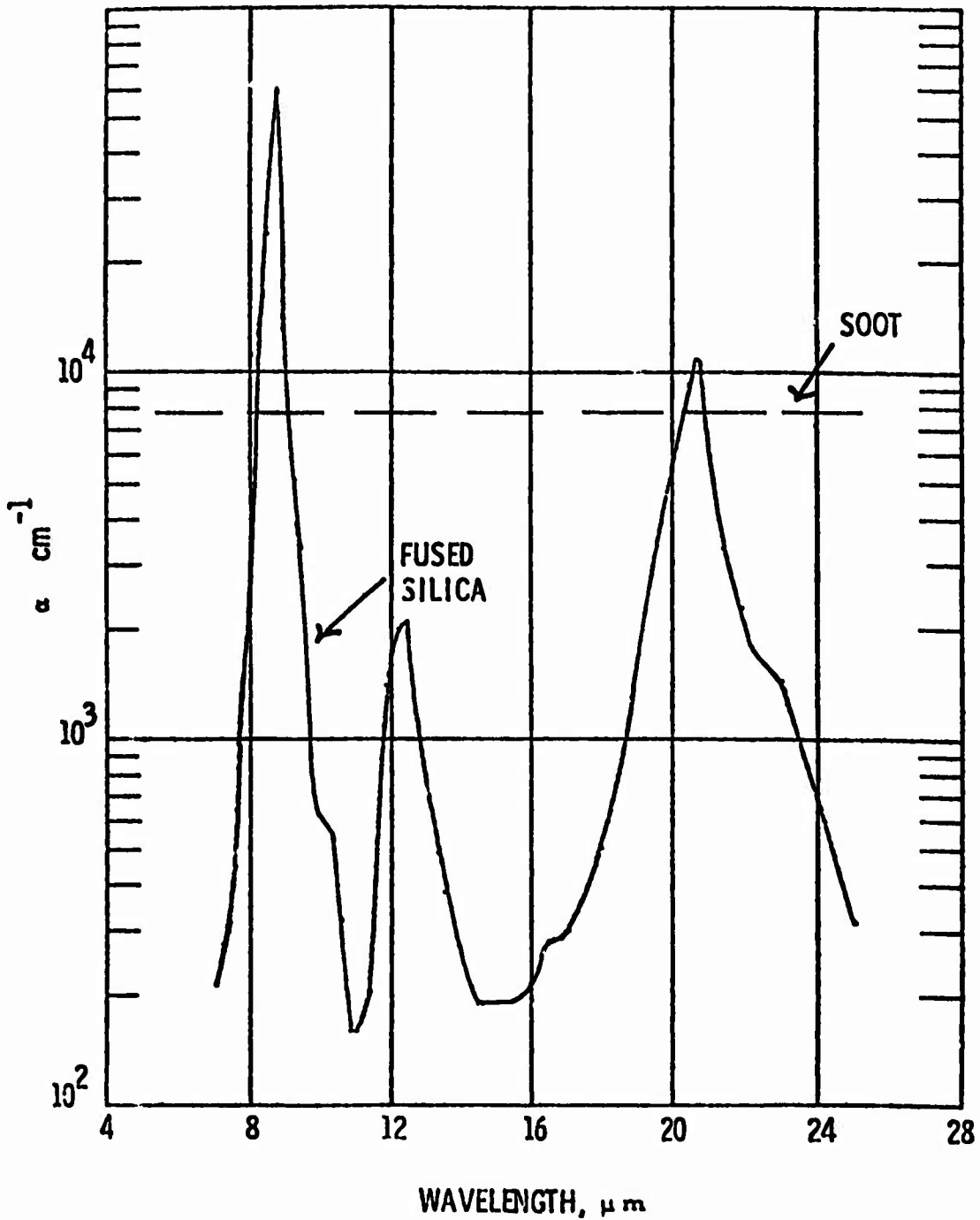


Figure E2. Volume absorption coefficient vs. wavelength for soot and fused silica. T = 300°K.

1. Neutral Bremsstrahlung is continuum radiation produced by inelastic scattering of electrons from neutral atoms or molecules. The appropriate cross sections have been experimentally determined for the major constituents of air N_2 and O_2 ,⁷ and the technique has been used for temperature measurements. However, this method is clearly inappropriate for this application due to the very low and undefined electron concentration.

2. In principle the measurement of the absolute emission from CO_2 (or other infrared active molecules) behind the incident shock could be used to determine gas temperature. The shock heated air is at equilibrium with the CO_2 at its ambient concentration. A simple IR radiometer could be constructed with appropriate filter and calibrated in a small, pressure driven shock tube. An example of this type of measurement is shown in Fig.E3 taken from one of the author's own papers. This figure shows the emission from the first overtone band of CO at 2.3μ . The expected temperature sensitivity for the 4.3 band of CO_2 would be similar to the dashed curve on Fig.E3.

The difficulty of this technique is that the interpretation is simple only if the gas is optically thin. The optical opacity, μ , for infrared molecular radiation may be defined in terms of the product of path length, l , and density of species, P , in atmospheres

$$\mu = Pl \sim 0.5 \text{ atm-cm for } CO_2 \text{ in DABS}$$

This is a value of μ for which the fundamental infrared bands of species such as CO_2 , CO, NO and H_2O are generally black. For example, Fig.E4 shows the emissivity (proportional to intensity) of the 4.3μ fundamental band of CO_2 for various values of Pl for $1500^\circ K$. In the region of the band head ($\sim 2300 \text{ cm}^{-1}$), it can be seen that the emissivity curves do not scale with Pl for $Pl > 0.1$. The curves do scale in the wing of the band, $\lambda < 2200 \text{ cm}^{-1}$. However, the intensity is much weaker in the wings and obviously more difficult to detect and measure quantitatively. In principle, optical calibration of this technique

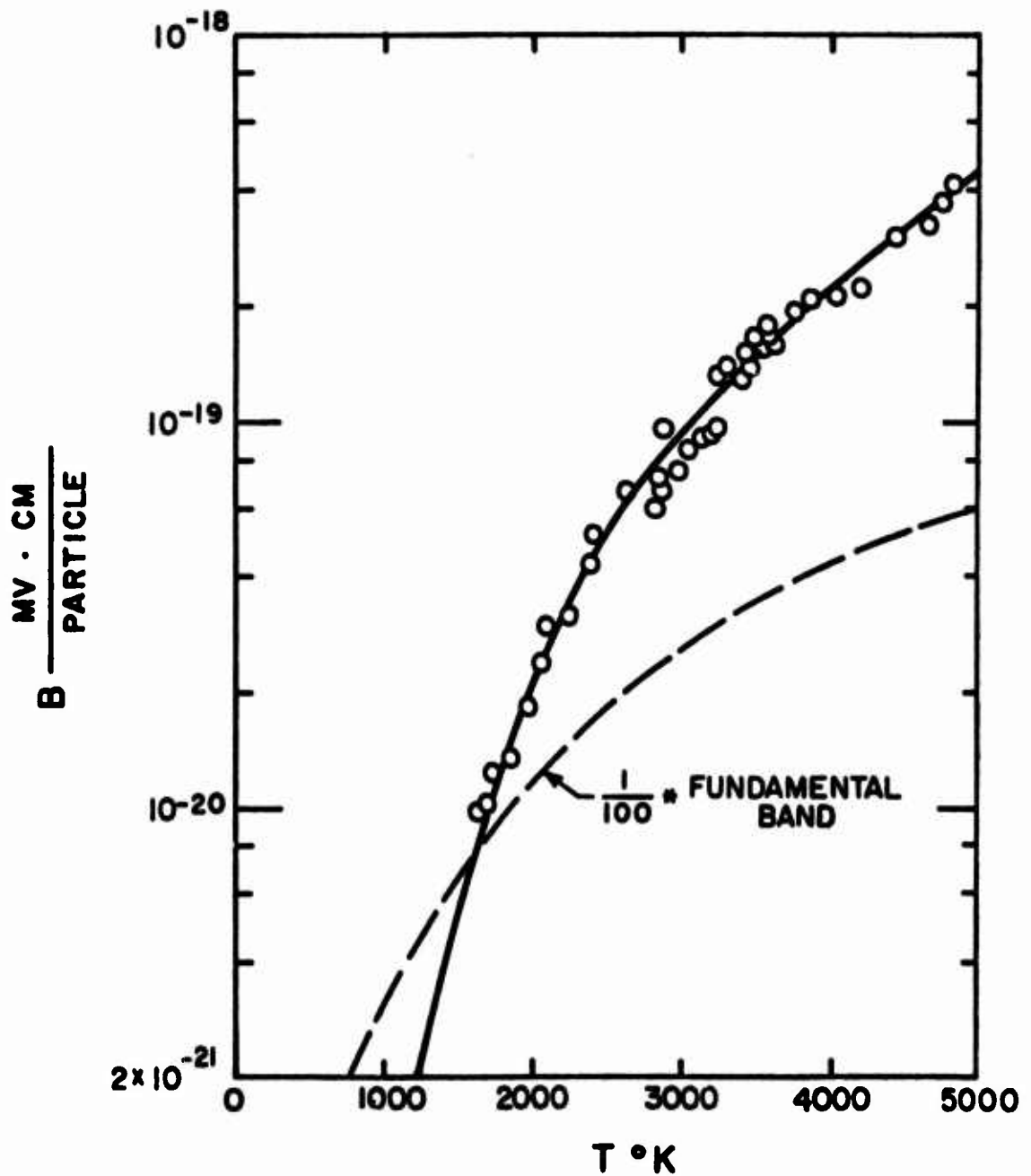


Figure E3. Data from incident shock calibration on the CO first overtone emission. The parameter $B = S/A_{M^{n_{\text{CO}}}}$, defined in the text, is proportional to radiated power per particle per steradian. The dashed curve shows the temperature dependence of the fundamental band emission.

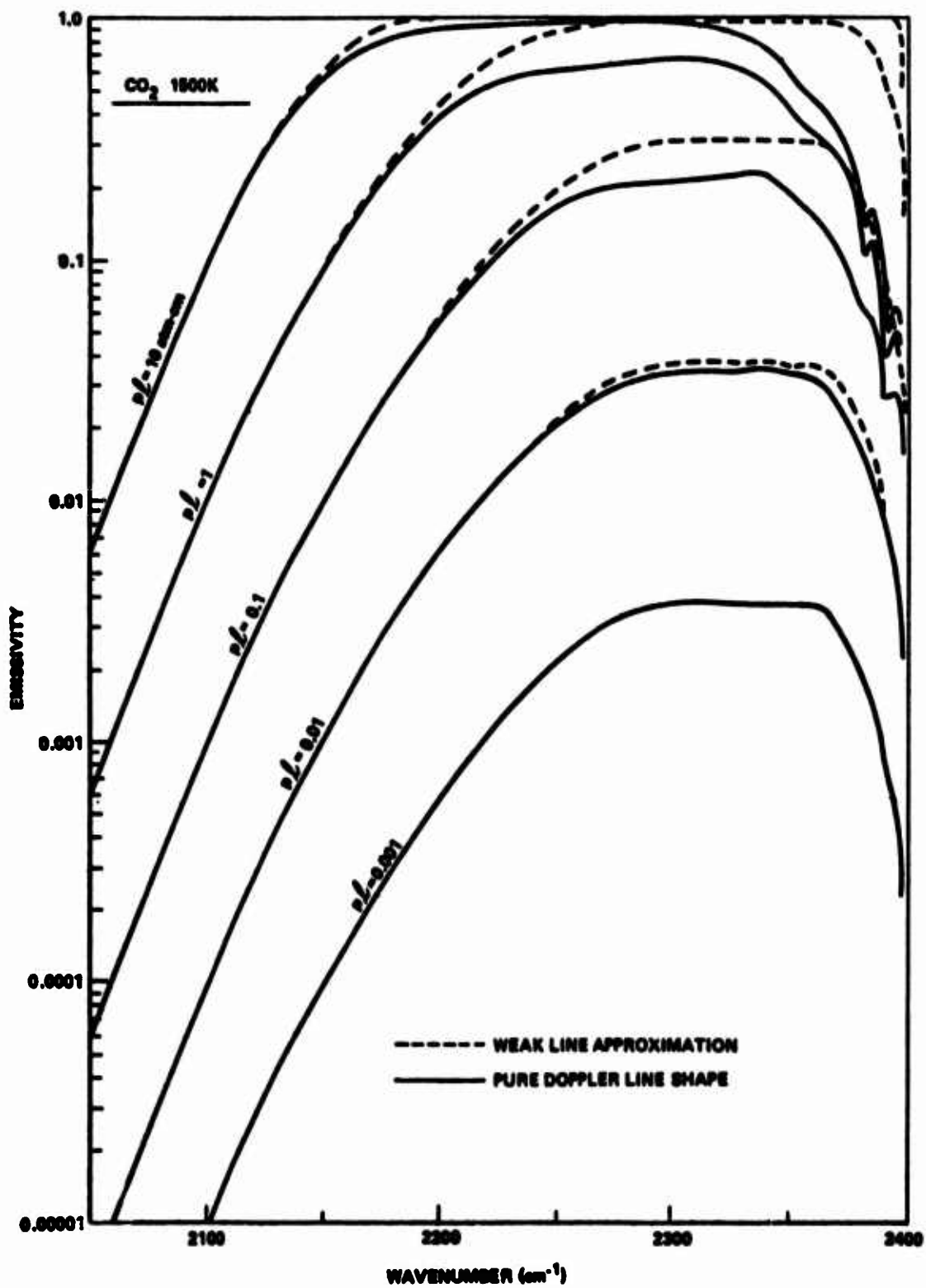


Figure E4. CO₂ 4.3- μ band emissivity versus wavenumber for pure Doppler line shape and weak line approximation for T = 1500K.

could be carried out under conditions of identical $P l$ even for $P l \geq 0.1$. In the small shock tube the pressure of CO_2 would have to be increased to account for the smaller l . However, interpretation becomes less certain, and, as the gas becomes more optically thick, the technique samples boundary layer gas which is not of interest.

3. It is well known that the relative population of rotational states of a specific vibrational level of a molecule can be used to determine the rotational temperature of a gas. Since, under DABS conditions, the various internal modes of the gas are in equilibrium, a measurement of rotational temperature would yield gas temperature. The population of the rotational levels of CO_2 can be measured in absorption by using a probe CO_2 laser. This measurement has several inherent advantages. First, the CO_2 laser radiation is not absorbed to any appreciable extent by the room temperature CO_2 in the atmosphere ($< 1\%/km$ for most CO_2 laser lines). Hence, the probe laser could be placed a reasonable distance from the facility. Second, behind the incident shock the CO_2 is heated to 2000°K and this temperature rise provides enough increase in CO_2 (100) population to create significant and measurable absorption over the 200 cm DABS path length. Finally, determination of only two rotational state populations is necessary. It is possible to operate a CO_2 laser on two individual transitions simultaneously, hence the same source and collection optics could be used for this measurement.

However, the technique is not recommended at this time because the absorption and scattering of the laser radiation by the soot particle is a possible serious degradation. Furthermore, in the driver gases, large turbulent density gradients may exist and prevent propagation of a well collimated beam across the tube. This technique could be implemented at a later date after some of the questions concerning particles and turbulence have been resolved.

4. Since the gas is probably optically black because of a high mass loading of carbon particles, one very simple optical technique to measure temperature is to use a two color radiometer. Figure E5 shows the spectral

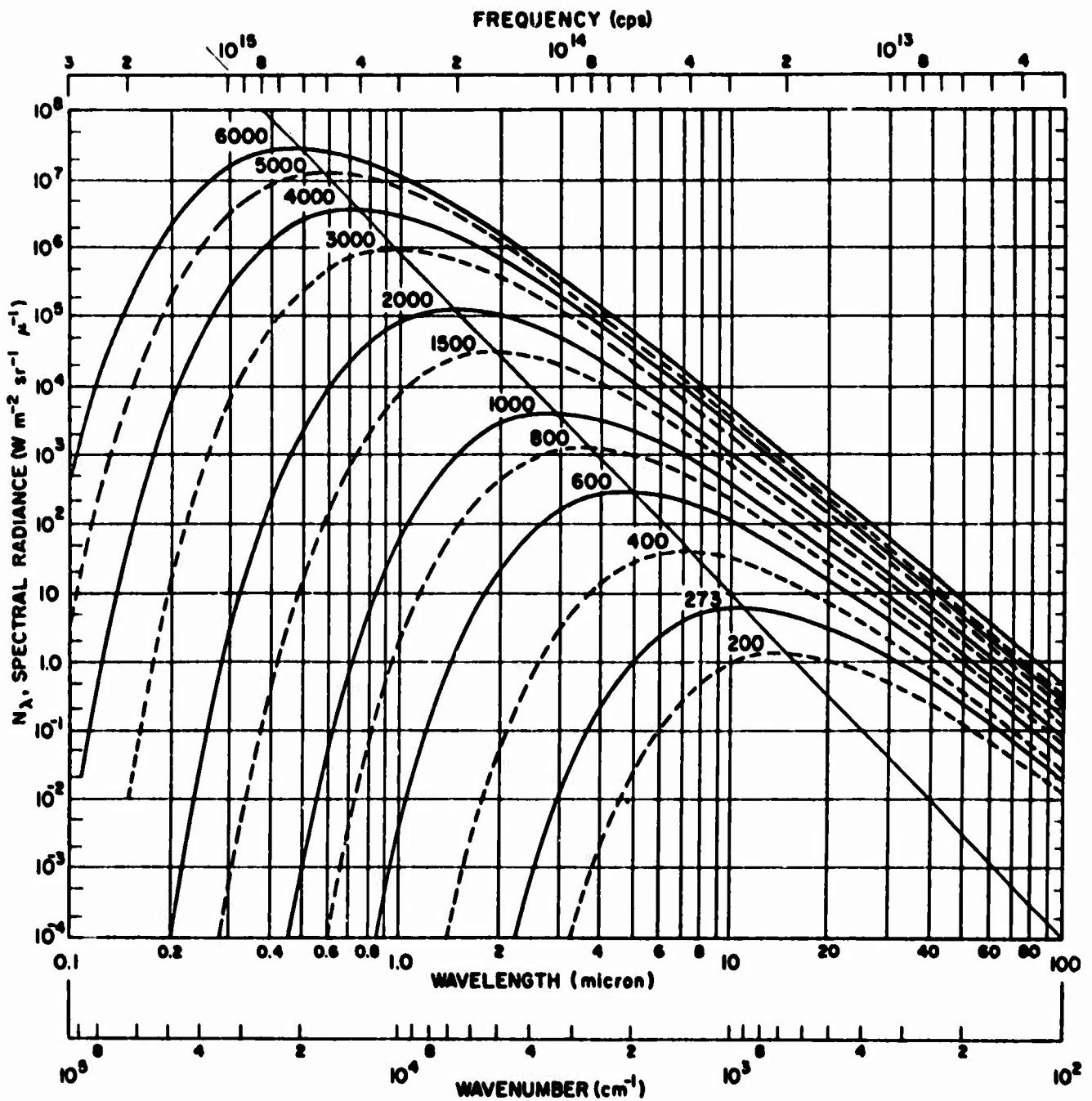


Figure E5. Spectral radiance of a blackbody, N_λ , at the temperature in °K shown on each curve; beyond 100μ the curves continue to be linear (plotted on logarithmic scales). The diagonal line, intersecting the curves at their maxima, shows Wien's displacement law. (Subdivisions of the ordinate scale are at 2 and 5.) Figure by P. R. Gant.

radiance of a blackbody, N_λ , as a function of wavelength for various temperatures. It can be seen that for the conditions existing in DABS, i. e., $T \sim 2000^\circ\text{K}$, the peak of the blackbody function is 1-2 μ .

Many techniques have been developed to determine temperature from measurements of blackbody radiance. For the present application, two points must be considered: (i) the radiance from the detonation products will be composed of contributions from both molecular bands and continuum from the particles. (ii) The emissivity of carbon particles is both a function of size and wavelength.

The first point is the more important. Ferriso et al⁸ have developed an infrared band-ratio technique for temperature determination under the condition of radiation from both molecular bands and particle continua. This technique was developed for measurements in rocket exhausts for which the gas conditions are similar to those being considered in DABS. Ferriso et al suggest that the most appropriate wavelengths for observation of the continuum radiation are at 2.3 and 4.0 μ . Figure E6 is an example of the expected emission from the high temperature molecular radiators that can be expected in the DAB environment. Note that this figure is for 3000^oK. As is evident, the wavelength region of 2.3 and 4.0 μ are natural valleys between the emissivity peaks of bands from CO_2 , CO , and H_2O .

The emissivity of carbon particles is a somewhat controversial issue. Existing measurements⁹ do not all agree, but clearly indicate particle size and composition dependence. However, it appears that the emissivity of small (sub-micron) carbon particles is probably ~ 0.9 and reasonably constant in the infrared spectral region. Therefore, in the present application, the existing uncertainty in carbon particle emissivity does not introduce a serious error.

CONCLUSIONS

The following recommendations have been developed in this consulting study:

(i) The environmental conditions existing in the DABS facility preclude developing any sophisticated radiation diagnostics at this time. In

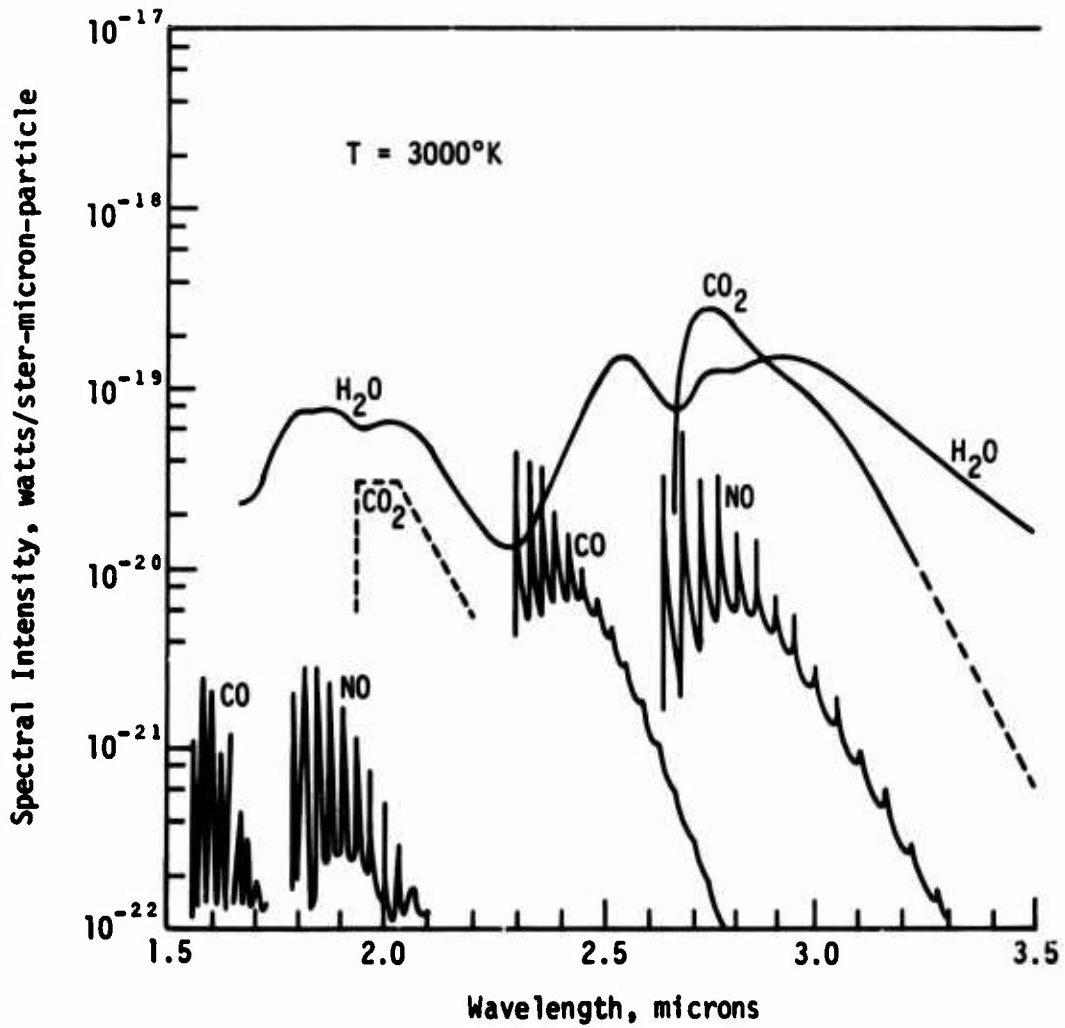


Figure E6. Example of Expected Emission from High Temperature Molecular Radiators in DAB Environment (1 of 2)

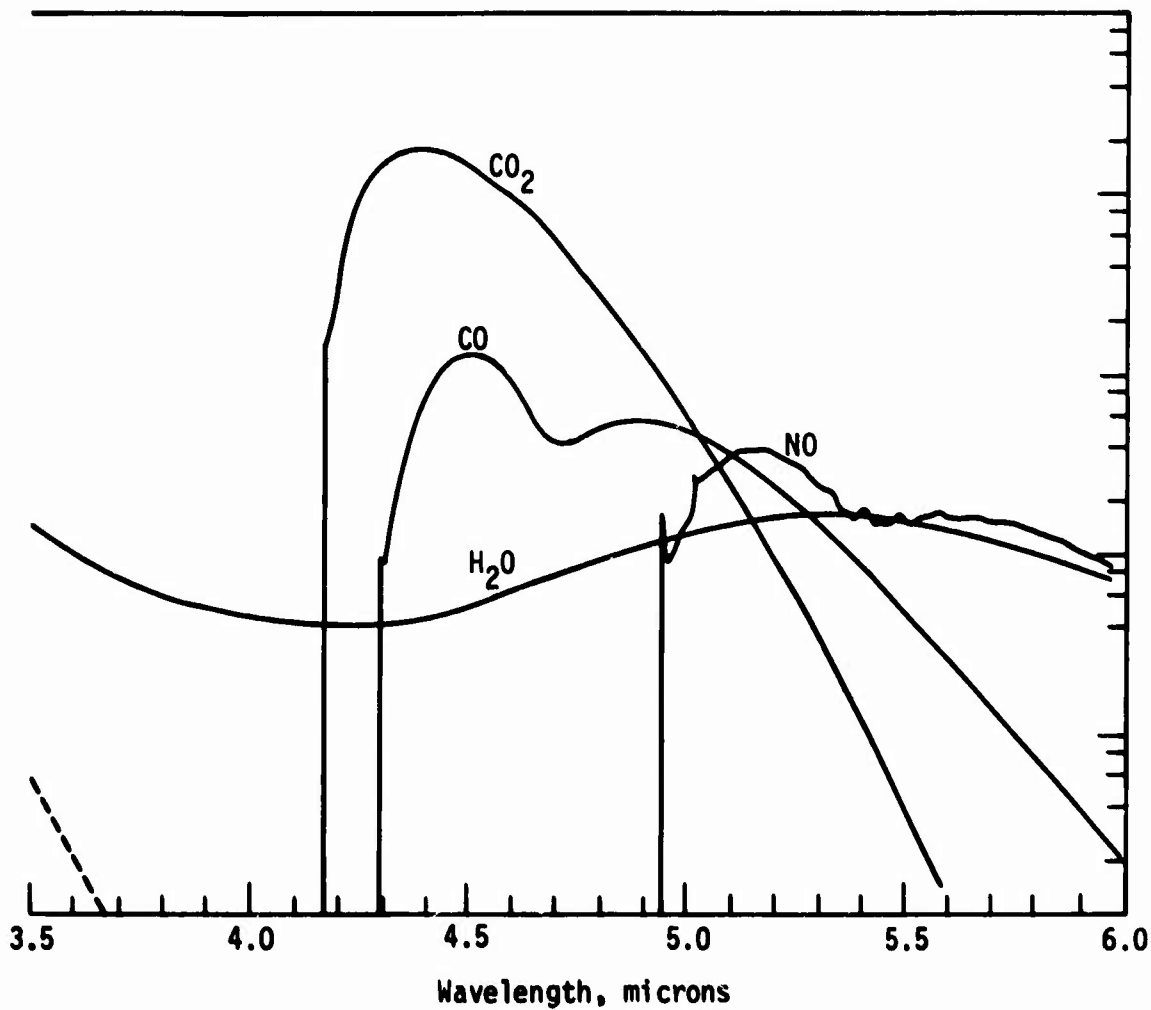


Figure E6. Example of Expected Emission from High Temperature Molecular Radiators in DAB Environment (2 of 2)

particular, the possible high mass loading of particles and the large optical depth of molecular radiators indicate that the gas (at least the detonation products) are probably opaque and volume sampling may be impossible. In addition, high turbulence levels and interface combustion indicate that the gas is inhomogeneous, and it may be difficult to probe the medium with any external source (laser absorption, Raman scattering, etc.).

(ii) The environmental conditions described above suggest that simple radiation diagnostics should be developed to (a) determine qualitative understanding of the DABS gas conditions and (b) used in conjunction with existing pressure probes to provide some further information about shock tube flow parameters. In particular, it is important to ascertain whether the gas is optically black and/or whether a probe beam can be propagated across the tube. Simple transmission measurements using a probe laser (Ruby at 6943 \AA) as well as a quartz lamp would provide some initial information in this regard. These measurements should have sufficient spatial and time resolutions that the signals could be correlated with existing pressure probes. This correlation might yield information about the separation of the shock and driver gases and help understand the "two spike" pressure records.

(iii) In addition, it is recommended that simple infrared radiometers be developed and used on future DABS tests. If the gas is optically black, it should be possible to determine gas temperature by IR emission measurements. Either simple overall band measurements ($\propto \epsilon \sigma T^4$) can be used or the more sophisticated band ratio method⁸ can be employed. In any event, it should be possible to provide an estimate of gas temperature which can be correlated with other variables of shock performance.

References

1. D. P. Martens, "Dynamic Airblast Simulator Feasibility Test (DABS 1-A) Quick Look Report", Technical Note No. DE-TN-75-027, AFWL, January 1976.
2. J. Hilsenrath and M. Klein, "Tables of Thermodynamic Properties of Air in Chemical Equilibrium including Second Virial Corrections from 1500^oK to 15,000^oK", AEDC-TR-65-58, Arnold Air Force Station, Tennessee, March 1965.
3. M. Camac, R. M. Feinberg, and J. D. Teare, "The Production of NO in Shock Heated Air," Avco Everett Research Laboratory, Inc. Research Report 245, December 1966.
4. Capt. D. P. Martens, DABS Diagnostics Working Group, AFWL, May 18-19, 1976.
5. Cook, The Science of High Explosives, ACS Monograph No. 139.
6. C. D. Lanzo and R. G. Ragsdale, "Experimental Determination of Spectral and Total Transmissivities of Clouds of Small Particles", NASA TND-1405, NASA, Washington, D. C., September 1962.
7. R. L. Taylor and G. E. Caledonia, J.Q.S.R.T. 9, 681 (1969).
8. C. C. Ferriso, C. B. Ludwig and F. P. Boynton, "A Band-Ratio Technique for Determining Temperature and Concentration of Hot Combustion Gases from Infrared-Emission Spectra", Proceedings of the Tenth Symposium (International) on Combustion, The Combustion Institute, Pittsburg, PA, 1965, pp. 161-173.
9. M. E. Whitson, Jr., "Handbook of the Infrared Optical Properties of Al₂O₃ Carbon, MgO, and ZrO₂", SAMSO-TR-75-131, Vol. I, Air Force Rocket Propulsion Laboratory, Edwards Air Force Base, CA, 4 June 1975.

APPENDIX F
CERF INSTRUMENTATION RECOMMENDATIONS

MEMORANDUM

Due to the apparent nature of the flow field, measurements that can reliably be accomplished while still yielding significant information with regard to the nature of the flow field are as follows:

1. Shock Wave Velocity, which is currently being measured very successfully.
2. Force Measurements.
 - a. Static pressure, being measured at several locations.
 - b. Total pressure, being measured at several locations.
 - c. Drag, not being measured.
3. Radiative heat transfer, not being measured.

Local Mach number can be successfully determined by a simultaneous measurement of static pressure, total pressure and drag. The drag measurement is necessary in order to determine the effective ratio of specific heats. If this is assumed known, a drag measurement is necessary.

The following governing equations relate the measured quantities to Mach number, M , and the effective ratio of specific heats, γ .

Total pressure/static pressure ratio.

$$\frac{P_{02}}{P_1} = \left(1 + \frac{\gamma-1}{2} M^2\right)^{\frac{\gamma}{\gamma-1}} \quad \text{For } M \leq 1 \quad (\text{F1a})$$

$$\frac{P_{02}}{P_1} = \left(\frac{\gamma+1}{2} M^2\right)^{\frac{\gamma}{\gamma-1}} \left(\frac{2\gamma}{\gamma+1} M^2 - \frac{\gamma-1}{\gamma+1}\right)^{\frac{-1}{\gamma-1}} \quad M > 1 \quad (\text{F1b})$$

$$\text{Drag } \frac{D}{ps} = \frac{\gamma}{2} M^2 C_D (M) \quad (\text{F2})$$

This drag coefficient is a single-valued function of Mach number and is virtually independent of the wake and, at the expected conditions generated by the DABS, independent of Reynolds number. This drag coefficient* as a function of Mach number is shown in Figure F1 by the open symbols. The closed symbols represent the product of $M^2 C_D (M)$. These data are then least squared to the following function:

$$AM^b$$

A and b were found to be:

$$\begin{aligned} A &= 1.048 \\ b &= 2.487 \end{aligned}$$

with a goodness of fit 0.99

D , P_{02} , and P are measured and S is the cross-sectional area of the cylinder. Once the left-hand side of equations F1 and F2 are known, a solution for γ and M can be found by any one of a number of numerical techniques. The bisection method or a similar technique is recommended rather than Newton-Raphson due to the problems encountered near Mach one in the sensitivity of the result. If γ is assumed to be known then the drag measurement is unnecessary. It should be noted, however, the relative sensitivity of the technique for an error in γ . At $M=1$.

$$\frac{1}{P_0/p} \Delta \left(\frac{P_0}{p}\right) = \frac{2\gamma^2}{\gamma^2-1} - \frac{\gamma}{(\gamma-1)^2} \ln \left(\frac{\gamma+1}{2}\right) \frac{\Delta\gamma}{\gamma} \quad (F3)$$

For a 5% error in γ the following errors result in P_0/p .

γ	P_0/p
1.1	31%
1.2	18.5%
1.3	14.5%
1.4	12.5%

It is therefore recommended that a measurement of drag be made in conjunction with pressure to determine the effective γ . In addition, at high mach numbers, $M > 0.8$. $C_D (M)$ is approximately constant and the dynamic pressure can easily be determined since:

$$\frac{D}{C_D S} = q$$

*Ref: Hoernen, Fluid Dynamic Study Drag, Figure A, Transonic Flow Chapter.

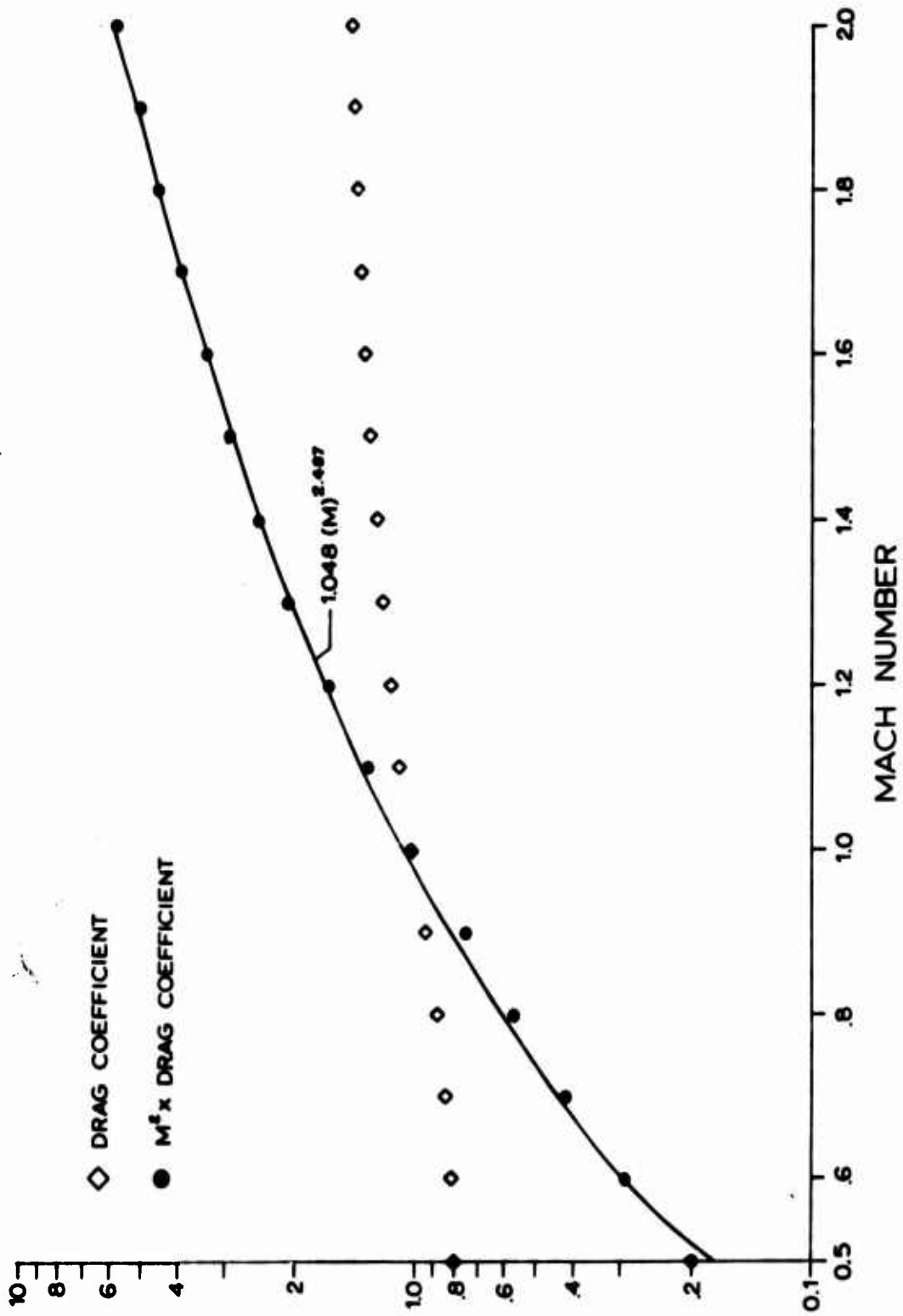


Figure F1. Blunt Cylinder Drag as a Function of Mach Number

Also, I may be approximated between M equalling 0.8 to 2.0., since C_D is a regular function and relatively slowly varying.

Another interesting observation is the effect of compressibility on the Bernoulli result.

$$\frac{P_o}{P} = (1 + \frac{\gamma-1}{2} M^2)^{\frac{\gamma}{\gamma-1}} = 1 + \frac{\gamma}{2} M^2 + \frac{\gamma}{8} M^4 + \frac{(2-\gamma)\gamma}{48} M^6 + O(M^8) \quad (F4)$$

$$\frac{P_o}{P} = 1 + \frac{q}{P} = 1 + \frac{M^2}{4} + \frac{2-\gamma}{24} M^4 + O(M^6) \quad (F5)$$

The bracketed term to order M^4 and has the following values:

M^{γ}	1.2	1.4
0.8	1.17	1.17
1	1.28	1.28
1.2	1.43	1.41

If the $M = 1$ value is used:

$$\frac{P_o}{P} = 1 + \frac{q}{P} = 1.28 \quad (F6)$$

$$\text{then } q = \frac{P_o - P}{1.28} \quad (F7)$$

Which gives no more than a 15% error in q for this Mach number range. Thus, a quick approximation for q can be made by using a reasonable value of the bracketed coefficient at a given point time in time.

Radiative Heat Transfer

Much information can be gathered through a wide-wall radiative heat-transfer measurement. H_2O and CO_2 are expected combustion products, and therefore, monitoring their vibration-rotation spectra in the near-infrared should yield information with regard to the nature of the shock-heated region and the relative location of the deflagration and/or indicate that the gas is optically thick at this wavelength, the resulting radiation can be directly related to the gas temperature through the black body function.

for $K_{\nu} \ell \gg 1$

$$g_{\nu} = (VF) \frac{2\ell_{\nu}^3}{\exp(\frac{h\nu}{c/kt}) - 1} \quad (F8)$$

VF is a view factor and $\Delta\nu$ is the bandwidth of the filter. Note that this approach makes the measurement independent of the gas properties and relative concentrations.

Even if this is not the case, this experimental measurement will yield information with regard to the relative locations of the shock front and flame and/or combustion products front.

It is suggested that two measurements be made: One over a narrow region in the infrared and one broad band over the wavelength region.

Narrow Region 2.5 - 2.8 μ

Broad Band .2 ----- μ

These can be accomplished by using a synthetic sapphire window (Al_2O_3) and a filter for the narrow region.

The following table gives the locations of the infrared band heads.

H_2O		CO_2	
<u>λ</u>	<u>quality</u>	<u>λ</u>	<u>quality</u>
<u>6.2 μ</u>	<u>very strong</u>	<u>15 μ</u>	<u>very strong</u>
<u>2.66 μ</u>	<u>very strong</u>	<u>4.26 μ</u>	<u>very strong</u>
<u>1.14 μ</u>	<u>strong</u>	<u>2.77 μ</u>	<u>very strong</u>
<u>.94 μ</u>	<u>strong</u>	<u>2.69 μ</u>	<u>very strong</u>

The broad band radiation will give evidence of solid particle radiation as well as any chemi-luminescence occurring from the combustion process if it is occurring.

ABBREVIATIONS, ACRONYMS, AND SYMBOLS

B	magnetic field
C	speed of light
E	electric field
E/V	specific explosive energy density
F	force
I	intensity
I_D	debris impulse
M_x	mach number
P	driver pressure
Q	dynamic pressure
T	absolute temperature
V	velocity
c	secondary shock velocity
f_d	doppler frequency
f_r	radar frequency
h	Planck's constant
k	Boltzmann's constant
m	areal density of debris mass
n_i	number of particles
p_0	stagnation pressure
p_{0y}	pitot tube pressure
p_x	static pressure in flow
p_y	static pressure in stagnated region
q_i	charge on particle
u	DABS flow velocity
v	voltage
$\Delta t_1, \Delta t_2$	time intervals
δ	distance between gages
γ	ratio of isobaric to isovolumetric specific heats
θ	angle between secondary shock propagation and DABS flow
λ	wavelength
ρ	density
ϕ	angle between line connecting explosive charge and gages and flow direction

DISTRIBUTION LIST

DEPARTMENT OF DEFENSE

Assistant Secretary of Defense
Intelligence
ATTN: ODASD

Assistant to the Secretary of Defense
Atomic Energy
ATTN: ATSD/AE

Defense Advanced Research Project Agency
ATTN: Technical Library
ATTN: PMO
ATTN: STO
ATTN: NMRO

Defense Documentation Center
Cameron Station
2 cy ATTN: TC

Defense Nuclear Agency
ATTN: STSI
2 cy ATTN: SPSS
3 cy ATTN: STTL, Technical Library

Under Secretary of Defense for Rsch. & Engrg.
ATTN: Assistant Director, Nuc. Prgms.
ATTN: Deputy Director, Strat. Sys.
ATTN: Deputy Director, Tactical Warfare
ATTN: Assitant Director, Strat. Wpns.

Field Command
Defense Nuclear Agency
ATTN: FCPR
ATTN: FCT

Livermore Division, Field Command, DNA
Lawrence Livermore Laboratory
ATTN: FCPRL

DEPARTMENT OF THE ARMY

Assistant Chief of Staff for Ops. & Plans
Department of the Army
ATTN: Technical Library

Ballistic Missile Defense Advanced Tech. Central
Department of the Army
ATTN: CRDABH-X
ATTN: CRDABH-S

Ballistic Missile Defense Prog. Office
Department of the Army
ATTN: DACS-BMT

Commander
Fort Huachuca, AZ
ATTN: Commander

Commander
Harry Diamond Laboratories
Department of the Army
ATTN: DRXDO-NP
ATTN: Technical Library

DEPARTMENT OF THE ARMY (Continued)

Picatinny Arsenal
Department of the Army
ATTN: Technical Library

U.S. Army Ballistic Research Laboratories
ATTN: Technical Library

U.S. Army Engineer Center
ATTN: ATSEN-SY-L

U.S. Army Engineer Waterways Experiment Station
ATTN: W. Flathou, L. Ingram
ATTN: Library Branch
ATTN: F. Hanes

U.S. Army Nuclear & Chemical Agency
ATTN: ATCA-NAW
ATTN: Technical Library

U.S. Army Communications Command
ATTN: Technical Library

DEPARTMENT OF THE NAVY

Civil Engineering Laboratory
Naval Construction Battalion Center
ATTN: Technical Library

Naval Facilities Engineering Command
ATTN: Code 03A
ATTN: Code 03B
ATTN: Technical Library

Naval Research Laboratory
ATTN: Technical Library

Naval Ship Engineering Center
ATTN: Technical Library
ATTN: NSEC, 6105G

Naval Surface Weapons Center
ATTN: Code 240
ATTN: Code 1244, Navy Nuclear Prgms. Off.
ATTN: 241, J. Petes
ATTN: Code 730, Technical Library

Naval Surface Weapons Center
Dahlgren Laboratory
ATTN: Technical Library

Naval Weapons Center
ATTN: Technical Library

Naval Weapons Evaluation Facility
ATTN: Technical Library

DEPARTMENT OF THE AIR FORCE

Air Force Armament Laboratory, AFSC
ATTN: Technical Library

Air Force Systems Command
ATTN: DLCAW
ATTN: Technical Library

DEPARTMENT OF THE AIR FORCE (Continued)

Air Force Weapons Laboratory, AFSC
ATTN: DED-1
ATTN: DES-G
ATTN: DE
ATTN: DES-S
ATTN: SUL, Technical Library
ATTN: HO

Armament Development & Test Center
Department of the Air Force
ATTN: ADBRI.-2
ATTN: Technical Library

Foreign Technology Division, AFSC
ATTN: TDPMG
ATTN: TDFBD
ATTN: POTN
ATTN: Technical Library

Space and Missile Systems Organization/DY
Department of the Air Force
ATTN: DYS

Space and Missile Systems Organization/RS
Department of the Air Force
ATTN: RSSE

Space and Missile Systems Organization/XR
Department of the Air Force
ATTN: XRTB

Space and Missile Systems Organization/MN
Department of the Air Force
ATTN: MNN, Engr. Division
ATTN: MNNH
ATTN: MMI

DEPARTMENT OF ENERGY

Division of Military Application
ATTN: Test Office

Los Alamos Scientific Laboratory
ATTN: Technical Library
ATTN: G. Spillman
ATTN: A. Davis

Sandia Laboratories
Livermore Laboratory
ATTN: Technical Library

Sandia Laboratories
ATTN: L. Vortman
ATTN: Technical Library

University of California
Lawrence Livermore Laboratory
ATTN: Technical Library

DEPARTMENT OF DEFENSE CONTRACTORS

Aerospace Corporation
ATTN: Technical Info. Services

Agabian Associates
ATTN: M. Agabian

The Boeing Company
ATTN: Technical Library

DEPARTMENT OF DEFENSE CONTRACTORS (Continued)

Brown Engineering Company, Inc.
ATTN: M. Patel

California Research & Technology, Inc.
ATTN: Technical Library

Civil/Nuclear Systems Corporation
ATTN: Civil/Nuclear Systems Corp.

EG&G, Incorporated
Albuquerque Division
ATTN: Technical Library

Electromechanical Systems of New Mexico
ATTN: R. Shunk

General Electric Company-TEMPO
Center for Advanced Studies
ATTN: DASIAC

IIT Research Institute
ATTN: Technical Library

H-Tech Laboratories, Inc.
ATTN: B. Hartenbaum

Kaman Sciences Corporation
ATTN: F. Shelton, D. Sachs
ATTN: Technical Library

Physics International Company
ATTN: C. Godfrey, C. Vincent
ATTN: D. Orphal
ATTN: Technical library
ATTN: F. Sauer

R&D Associates
ATTN: Technical Library

Science Applications, Inc.
ATTN: Technical Library

SRI International
ATTN: G. Abrahamson
ATTN: Technical Library

Systems, Science & Software, Inc.
ATTN: D. Grine
ATTN: Technical Library

TRW Defense and Space Systems Group
ATTN: P. Lieberman
ATTN: Technical Library

Eric H. Wang
Civil Engineering Research Facility
ATTN: N. Baum

Weidinger Associates
Consulting Engineers
ATTN: J. Isenberg

Weidinger Associates
Consulting Engineers
ATTN: M. Baron